Multiband Dielectric Resonator Antennas Based on 3D-Printed Inhomogeneous and Anisotropic Ceramics

José Bruno de Araújo

THÈSE

En vue de l'obtention du

DOCTORAT DE L'UNIVERSITÉ DE TOULOUSE

Délivré par : *l'Institut Supérieur de l'Aéronautique et de l'Espace (ISAE)*

Présentée et soutenue le *Date de défense (XX/10/2022)* **par :**

José Bruno DE ARAÚJO

Multiband Dielectric Resonator Antennas Based on 3D-Printed Inhomogeneous and Anisotropic Ceramics

---

JURY

Nathalie RAVEU	LAPLACE	Présidente
Eva RAJO-IGLESIAS	UC3M	Membre
Raphaël GILLARD	IETR	Membre
Alexandre CHABORY	ENAC	Membre
Marjorie GRZESKOWIAK	LAAS	Membre

École doctorale et spécialité :
GEET : Électromagnétisme et Systèmes Haute Fréquence
Unité de Recherche :
ENAC-LAB - Laboratoire de Recherche ENAC
Directeur(s) de Thèse :
Christophe MORLAAS et *Romain PASCAUD*
Rapporteurs :
Christophe DELAVEAUD et *Cyrille MENUDIER*

Acknowledgements

Contents

List of Figures

List of Tables

List of abbreviations

5G	*Fifth Generation of Mobile Communication*
AR	*Axial Ratio*
BZ	*Brillouin Zone*
CNSS	*Compass Navigation Satellite System*
CP	*Circular Polarization*
DC	*Direct Current*
DRA	*Dielectric Resonator Antenna*
DWM	*Dielectric Waveguide Model*
GNSS	*Global Navigation Satellite System*
GPS	*Global Positioning System*
IBZ	*Irreducible Brillouin Zone*
IoT	*Internet of Things*
IMW	*Imperfect Magnetic Walls*
ISM	*Industrial, Scientific, and Medical*
LHCP	*Left-Hand Circular Polarized*
LHI	*Linear, Homogeneous, and Isotropic*
MMIC	*Monolithic Microwave Integrated Circuit*
MTM	*Metamaterial*
MWM	*Magnetic Wall Model*
PEC	*Perfect Electrical Conductor*
PMC	*Perfect Magnetic Conductor*
RHCP	*Right-Hand Circular Polarized*
TE	*Transverse Electric*
TM	*Transverse Magnetic*
TTC	*Telemetry, Tracking and Command*
VSWR	*Voltage Standing Wave Ratio*

General Introduction

Context

Over the last couple of years, the use of three-dimensional (3D) printing, or additive manufacturing, has been increasing in several industry sectors. It consists in the additive construction of 3D objects based on computer-aided design (CAD) files on a layer-by-layer basis [1]. 3D printing is in the spotlight due to its several advantages such as flexible design, low-manufacturing cost, reduced waste, variety of printing materials, and fabrication on demand, to name a few. Due to these advantages, it is possible to find applications of 3D-printing in the aviation [2], medical [3], automotive [4], civil construction [5], and food industries [6], for instance.

When it comes to antenna applications, it is possible to find several 3D-printed structures proposed in the literature [8]. Due to the several advantages offered by this technology, the interest in 3D-printed antennas has been exponentially growing with each passing day, as can be seen in Fig. 1, where the trend of the term "3D printed antennas" in the Google Scholar database is presented over the last years. Usually, 3D-printed antennas are classified in terms of the materials used in the printing process: 1) antennas printed with dielectric materials and subsequently metalized, 2) the ones printed directly with conductive materials, and 3) full-dielectric antennas. Figure 2(a) shows an example of a Voronoi antenna, where the structure

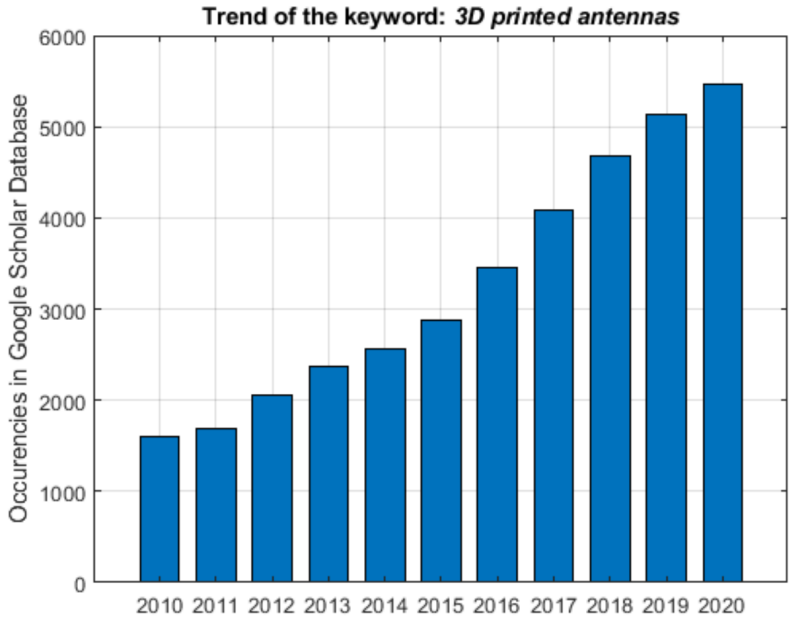

Figure 1: Trend of the term "3D printed antennas" from 2010 to 2020 in the Google Scholar database [7].

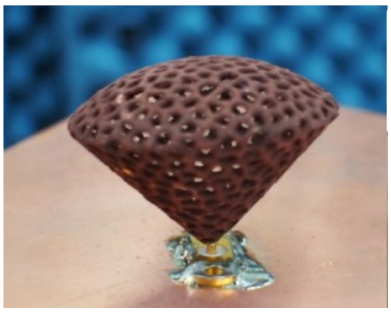

(a) Voronoi antenna 3D-printed plastic coated with metal [9]

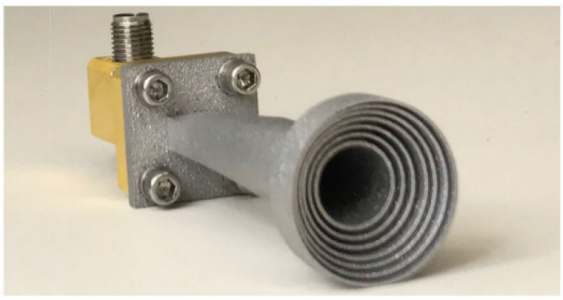

(b) 3D-printed full-metal horn antenna [10]

Figure 2: (a) Voronoi antenna 3D-printed in plastic and then coated with metal, and (b) horn antenna 3D-printed directly with metal.

is 3D-printed in plastic and, then, coated in metal [9]. The 3D-printed plastic coated with a highly conductive layer has a cheap fabrication cost but the metal coating may limit the electric performance of the antenna at high frequency due to the surface roughness and non-uniformity of the metallization process. In Fig. 2(b), a full-metal horn antenna is presented [10]. The 3D printing of metal is used to manufacture this axial corrugated horn for mm-wave frequencies. Also, the surface roughness is a challenge as well for the antennas printed directly with conductive materials. Therefore, 3D-printed antennas with conductive materials are still challenging and full-dielectric 3D-printed ones can be an interesting alternative.

3D-printing technology allows the creation of full-dielectric antennas with high precision and fine details [8], which opens up new possibilities and more design flexibility. For instance, it is possible to control the permittivity of an artificial homogeneous and isotropic lens used to enhance the gain of a broadband antenna, as can be seen in Fig. 3(a). In [11], an inhomogeneous Luneburg lens is created using the 3D printed technology, as can be observed in Fig. 3(b). Besides, 3D-printing has already been used to create an artificial anisotropic dielectric [12], as shown in Fig. 3(c), where a polarizer is proposed to convert a linearly-polarized radiator into a circularly-polarized one. Therefore, these three examples show the possibilities and degrees of freedom that the 3D-printed dielectrics can bring. Using isotropic and homogeneous printing materials with low dielectric constant, *i.e.* around 3 for these examples, it is possible to create artificial isotropic or anisotropic, homogeneous and/or inhomogeneous materials with a controlled dielectric constant to design different structures.

Most of the 3D-printed dielectric-only structures proposed in the literature for antenna applications are non-resonant, electrically large, and use printing materials with low dielectric constant as in Fig. 3. However, due to the recent developments in this technology, it is now possible to use ceramics with high permittivity for this type of application, which opens up new possibilities to design resonant and electrically-small structures. In France, the company 3DCeram develops 3D printers that use ceramics as printing materials such as zirconia, which is a material with high permittivity ($\varepsilon_r = 32.5$), low loss ($\tan\delta = 1.9 \cdot 10^{-4}$), and excellent physical and chemical properties ideal for harsh environments. From this technology, dielectric resonator antennas (DRA) using zirconia were recently designed and some examples are shown

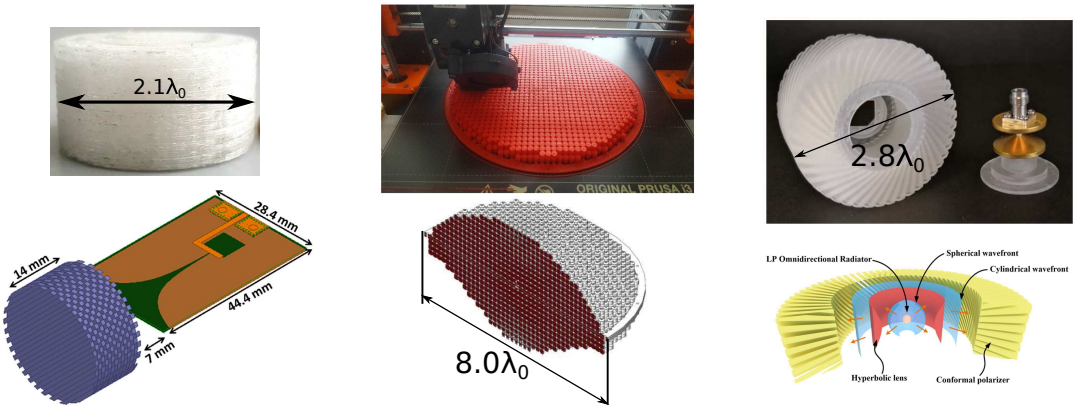

(a) Homogeneous lens (ε_r) [13] (b) Inhomogeneous lens ($\varepsilon_r(\vec{r})$) [11] (c) Anisotropic polarizer ($\overline{\overline{\varepsilon_r}}$) [12]

Figure 3: Examples of 3D-printed, non-resonant, and electrically-large dielectric structures for antenna applications.

in Fig. 4. In Toulouse, Anywaves proposed a homogeneous and isotropic DRA, where the effective permittivity is controlled by the use of 3D-printed periodic sub-wavelength unit cells [14], as shown in Fig. 4(a). On the other hand, Anywaves and XLIM designed an artificial inhomogeneous and isotropic dielectric resonator presented in Fig. 4(b) to create a dual-band circularly-polarized DRA [15]. Also, 3D-printing of anisotropic dielectric samples has been demonstrated in [16] with a circularly-polarized antenna that has been realized in Toulouse by ENAC, ISAE-SUPAERO, and Anywaves, as seen in Fig. 4(c). In these three cases, zirconia is used as the printing material, which is an isotropic and homogeneous material. Using the 3D-printing, it is therefore possible to design artificial anisotropic, isotropic, homogeneous, and/or inhomogeneous dielectrics and, then, to create new possibilities to design electrically-small dielectric resonator antennas.

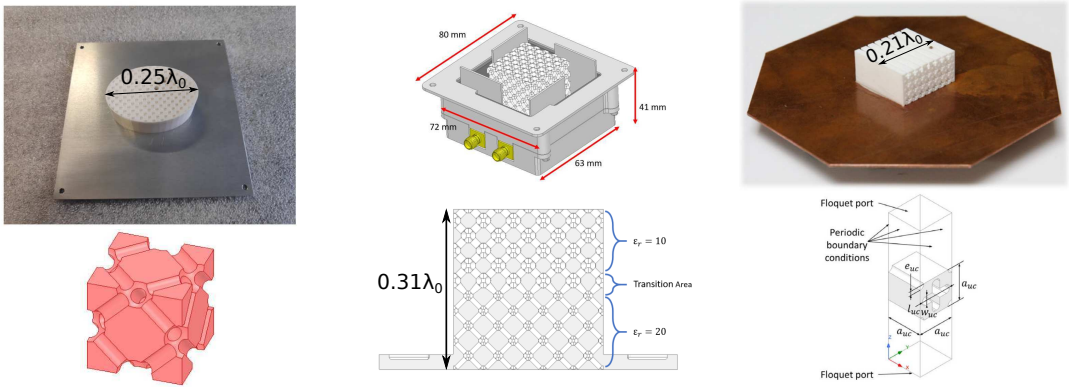

(a) Homogeneous DRA (ε_r) [14] (b) Inhomogeneous DRA ($\varepsilon_r(\vec{r})$) [15] (c) Anisotropic DRA ($\overline{\overline{\varepsilon_r}}$) [16]

Figure 4: Examples of 3D-printed, resonant, and electrically-small dielectric structures for antenna applications.

So far, dielectric resonator antennas have not been as popular as microstrip antennas, due to their high cost and difficult manufacturing process. However, a DRA, by itself, has advantages such as lack of ohmic losses, small size, several radiating modes, design flexibility, and large impedance bandwidth. The 3D printing of ceramics has the potential to change this scenario and give prominence to DRA once and for all with the possibility to fabricate it with different shapes and a wide variety of artificial effective dielectric properties.

The new degrees of freedom to design DRA offered by 3D printing can help to develop multiband antennas, which is very demanded in different applications. For instance, unmanned aerial vehicles (UAVs) and nanosatellites are experiencing high demand and a lot of effort has been made to reduce their size, which decreases the space available for their components such as antennas. At the same time, these platforms require different communication links at different frequencies for telemetry, control, data, and/or geolocalization, for instance. Each of these applications may also demand different radiating properties and frequencies. As aforementioned, in [15], a dual-band circularly-polarized 3D-printed inhomogeneous DRA has already been proposed. However, the circular polarization (CP) is achieved mainly by means of a complex feeding method and not directly due to the dielectric properties of the antenna. On the other hand, the CP obtained in [16] is due to the anisotropic DR but the antenna presents a single-band operation. Nevertheless, the possibility of using the concept of inhomogeneity and anisotropy together in a resonator sounds promising and increases the design flexibility to develop multiband DRAs with different polarizations and radiation patterns according to a given application. This is very important for different communication systems since it allows the use of a single antenna for different frequencies instead of multiple ones, which helps to save precious space in miniaturized platforms.

Objectives and Contribution

The main goal of this Ph.D. thesis is to study the capacity of 3D-printed ceramics for the design of new multiband and compact dielectric resonator antennas with good electromagnetic performances and respecting the constraints of small platforms. The possibility of having an inhomogeneous and anisotropic dielectric resonator with controlled permittivity is investigated for the first time with the use of 3D-printing technology.

Objectives

In this thesis, two main research axes are investigated:

I) Proposal of sub-wavelength periodic structures to design artificial inhomogeneous dielectric mixing isotropic and anisotropic media.

II) Design and fabrication of multiband antennas with different radiation patterns and polarizations by 3D printing.

Contribution

The contribution of this thesis consists of two distinct levels:

I) Some works in the literature already explored the use of DRA with anisotropic dielectrics, however, in most of these works, they were homogeneous. In this work, the electric properties of the dielectric are locally controlled to have circular polarization and/or control the radiation patterns at different frequency bands. In other words, inhomogeneous isotropic and/or anisotropic dielectrics are introduced within a rectangular DRA and, then, the expected electromagnetic behavior is achieved while keeping the same overall shape of the antenna.

II) To realize these antennas, the concept of periodic structures is used, where sub-wavelength unit cells are proposed to create artificial isotropic and anisotropic media inside the DRA. Thus, the dielectric properties of the antenna can be locally manipulated. To fabricate these antennas, 3D printing is employed, which allows the manufacturing of such small cells using zirconia, which is a physically robust material with excellent dielectric properties at microwave frequencies. A prototype is 3D-printed and measurements are carried out to validate the proposed antenna.

Outline

This Ph.D. thesis is structured as follows.

Chapter 1 aims to detail the necessary background for the comprehension of this work. An introduction about dielectric resonator antennas is presented, where their main characteristics are discussed and their equations for the electric field, resonance frequency, and Q-factor are developed. Moreover, a state-of-the-art to discuss different techniques to obtain multiband DRAs is presented, which helps to explain the motivation of this work.

Chapter 2 presents a single-fed dual-band linearly-polarized rectangular DRA with broadside radiation patterns. The first part shows an attempt to do so, however, the presence of an undesirable radiating mode is observed around the upper band. To overcome this issue, the electric field distributions of the modes of the DRA are analyzed and, thus, the permittivity of the dielectric is locally controlled to increase the resonance frequency of this undesirable mode, while keeping the expected radiation patterns at the lower and upper bands.

Chapter 3 aims to design a dual-band rectangular DRA with circular polarization. To do so, in the first part, the electric fields of the modes at issue are investigated and the possibility of using an anisotropic dielectric in some specific parts of the dielectric resonator is discussed. This is theoretically confirmed since the conditions to have CP are respected at both bands. The second part of this chapter provides the detailed results of the antenna with a finite ground plane and fed by a single slot. Thirdly, a parametric analysis is performed to provide a better understanding of the effect of each parameter of the anisotropic region on the

performance of the antenna and a design guideline is presented. Lastly, a study is presented to show the trade-off between DRA volume and theoretical 3-dB axial-ratio bandwidth of the proposed design.

Chapter 4 introduces the concept of periodic structures made out of sub-wavelength unit cells by 3D-printing. Indeed, in the previous chapters, the dielectric properties of the antennas are directly assigned on Ansys HFSS. However, to manufacture these antennas, it is necessary to come up with ideas on how to achieve the necessary dielectric properties. Here, we propose to 3D-print periodic structures of sub-wavelength unit cells to create artificial media with controlled effective permittivity. Taking this into account, we first describe the 3D-printing technologies. In the second part, a state-of-the-art about 3D-printed dielectric resonator antenna is presented. In the last part, the concept of periodic structures is introduced, and sub-wavelength unit cells that emulate artificial isotropic and anisotropic media are proposed.

Chapter 5 then presents the simulated results of the dual-band circularly-polarized DRA made out of periodic sub-wavelength unit cells. These results are compared with the antenna model used in Chapter 3, where the dielectric properties are directly assigned on Ansys HFSS. Secondly, the manufacturing process is described as well as the measurement setup. Finally, simulated and measured results are discussed.

In **Chapter 6**, a third band with a linearly-polarized omnidirectional radiation pattern is added to the previously proposed dual-band DRA. This new antenna operates at the GNSS L5 and L1 bands as well as the 2.45-GHz ISM band. An air cavity is here added to the center of the antenna in order to control the matching and resonance frequency of the resonant mode at the ISM band. To still have circular polarization at the L5 and L1 bands, the radiating modes are carefully analyzed so that the addition of the third band and its new elements do not disturb the performance of DRA at the GNSS bands.

Finally, the **Conclusions** are synthesized from the results obtained in this Ph.D. thesis. Also, perspectives for this work are discussed as well.

Chapter 1

Introduction to Dielectric Resonator Antennas

Contents

The purpose of this chapter is to present an introduction to dielectric resonator antennas (DRAs). At first, some reminders on dielectrics are briefly given in Section 1.1. In Section 1.2, a brief historical perspective about DRAs is presented. Then, the definition of DRAs, their different shapes, and feeding methods are detailed, and their main characteristics are discussed in Section 1.3. The theoretical aspects of rectangular DRAs are debated and the expressions for electric and magnetic field distribution, resonance frequency, and Q-factor are developed in Section 1.4. Finally, Section 1.5 shows the state-of-the-art about multiband DRAs.

1.1 Reminders on Dielectrics

Dielectrics are materials that become polarized when an external electrical field $\vec{E_a}$ is applied. More precisely, the centroids of the bound negative and positive charges of the atoms inside a dielectric are slightly displaced in opposite directions when $\vec{E_a}$ is applied, which is illustrated in Fig. 1.1, then creating numerous electric dipoles. The effect of these dipoles is accounted for by the electric polarization vector $\vec{P}$. In other words, $\vec{P}$ can be understood as the response of the dielectric when an external electrical field $\vec{E_a}$ is applied. To grasp these concepts, it is necessary to understand that a dielectric material is polarized when an electric field

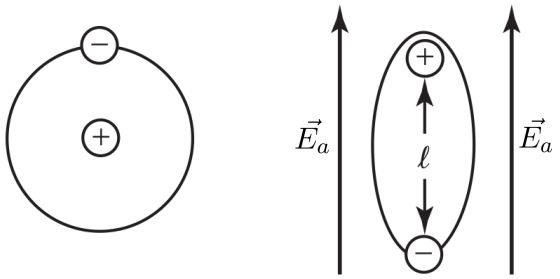

Figure 1.1: A typical schematic view of an atom in the (a) absence of applied electric field and (b) under an applied electric field [17].

$\vec{E}_a$ is applied and this material response is accounted for by $\vec{P}$ and both electric fields are related to each other through the following relation in the time-harmonic domain for a linear, homogeneous and non-dispersive medium:

$$\vec{D} = \varepsilon_0 \vec{E}_a + \vec{P}, \tag{1.1}$$

where $\vec{D}$ is the electric flux density vector and ε_0 is the free-space permittivity. The terms $\varepsilon_0 \vec{E}_a$ and electric polarization $\vec{P}$ account for the vacuum and material responses, respectively. Also, $\vec{P}$ can be expressed as

$$\vec{P} = \varepsilon_0 \left[\chi_e\right] \vec{E}_a, \tag{1.2}$$

where $[\chi_e]$ is the tensor of electric susceptibility, which is a measure of how easily bound charges are displaced due to an applied electric field. Therefore, (1.1) can be rewritten as

$$\vec{D} = \left[\varepsilon\right] \vec{E}_a, \tag{1.3}$$

where $[\varepsilon] = \varepsilon_0 \left(1 + [\chi_e]\right) = [\varepsilon_r] \varepsilon_0$ is the permittivity of the material. So, the most general relation between $\vec{D}$ and $\vec{E}$ in the time-harmonic domain, assuming a linear, homogeneous, and nondispersive medium, takes the form of a tensor of rank two, which can be expressed as follows

$$\begin{bmatrix} D_x \\ D_y \\ D_z \end{bmatrix} = \varepsilon_0 \begin{bmatrix} \varepsilon_{xx} & \varepsilon_{xy} & \varepsilon_{xz} \\ \varepsilon_{yx} & \varepsilon_{yy} & \varepsilon_{yz} \\ \varepsilon_{zx} & \varepsilon_{zy} & \varepsilon_{zz} \end{bmatrix} \begin{bmatrix} E_x \\ E_y \\ E_z \end{bmatrix}. \tag{1.4}$$

For reciprocal materials/media, their tensor of permittivity is a symmetrical matrix. Also, a symmetric matrix implies the existence of coordinate transformation that diagonalizes the tensor of permittivity [18]. Thus, $[\varepsilon]$ can be written as

$$[\varepsilon] = \varepsilon_0 \begin{bmatrix} \varepsilon_x & 0 & 0 \\ 0 & \varepsilon_y & 0 \\ 0 & 0 & \varepsilon_z \end{bmatrix}. \tag{1.5}$$

If all three components of this diagonal matrix are equal, the dielectric is said to be isotropic, which means that its electric permittivity is not a function of the direction of the applied electric field.

Electrically anisotropic, or simply anisotropic, materials are those whose electric permittivity is a function of the direction of the applied electric field, *i.e.* their charges are more easily displaced in some directions than in others. When only two out of three elements of the diagonal of the tensor are equal, the material is said to present uniaxial anisotropy. In this case, the dielectric has an ordinary permittivity ε_o and an extraordinary permittivity ε_e. If $\varepsilon_o < \varepsilon_e$, the material is said to present positive birefringence. On the contrary, if $\varepsilon_o > \varepsilon_e$, the dielectric is said to have negative birefringence. Also, the principal axis that presents the anisotropy is referred to as the optic axis. For instance, for a uniaxial dielectric with

$$[\varepsilon] = \varepsilon_0 \begin{bmatrix} \varepsilon_o & 0 & 0 \\ 0 & \varepsilon_o & 0 \\ 0 & 0 & \varepsilon_e \end{bmatrix}, \tag{1.6}$$

the z-axis is the optic axis. In addition, if $\varepsilon_x \neq \varepsilon_y \neq \varepsilon_z$, the material is said to be biaxial anisotropic.

1.2 A Brief History of the DRA

In 1939, Richtmyer theoretically demonstrated for the first time that open dielectric resonators (DRs) in form of spheres and toroids could radiate into free-space [19], but this theoretical work did not create a continuous interest in this subject at the short/medium-term. However, in the early 1960s, the interest in DRs was renewed due to the introduction of materials with high relative permittivity, such as rutile, but it was still not possible to develop practical microwave components due to their poor temperature stability leading to large resonant frequency changes [17]. In 1962, their modes were still experimentally investigated for the first time by Okaya and Barash [20].

In the 1970s, a new material evolution impulsed the usage of DRs with the introduction of low-loss ceramics, such as barium tetratitanate and (Zr-Sn)TiO_4. These ceramics were employed to fabricate DRs for monolithic microwave integrated circuits (MMICs) and semiconductor devices, due to their lightweight, temperature stability, high Q-factor, and low cost. In this scenario, DRs replaced traditional waveguide resonators in MIC applications, especially after the development of materials with dielectric constant higher than 80 with temperature stability and low-loss [17]. In addition to the evolution of the materials, this decade also witnessed some important theoretical studies. In 1975, Van Bladel investigated the general nature of internal and radiated fields of DRs by reporting a rigorous asymp-

totic method for evaluating their modes considering complex shapes with high permittivity [21]. Later, he and his research group investigated a cylindrical ring dielectric resonator and presented numerical results for the resonance frequencies, fields, and radiation Q-factor of low-order modes [22, 23].

Until the early 1980s, DRs had been mainly used as circuit elements in microwave integrated circuits [17]. However, in 1983, at the University of Houston, Long, McAllister, and Shen presented the first theoretical and experimental systematic investigation about the use of DRs as antennas, namely dielectric resonator antennas (DRAs) [24, 25, 26]. In this work, they developed cylindrical DRAs, where their analysis of radiation patterns, excitation methods, and resonant modes demonstrated their potential for millimeter-wave frequency applications. Still, in the 1980s, Birand and Gelsthorpe demonstrated the first linear array of DRAs [27], which was fed by a dielectric waveguide, and Haneishi and Takazawa proposed a linear array with broadband circular polarization [28].

In the late 1980s and early 1990s, most of the focus of the researchers around the globe interested in DRAs was on proposing different feeding methods to excite DRAs and the employment of analytical and numerical techniques to predict their Q-factor and input impedance. Some of the main studies were carried out at the University of Mississippi by Kishk and his research group [29, 30, 31], and at the City University of Hong Kong by Leung and Luk [32, 33]. In 1994, Mongia and Bhartia presented a review paper to summarize most of these works and standardize the modes nomenclature and provide simpler equations to theoretically calculate the resonance frequency and Q-factors for DRAs with different shapes. Moreover, at the Communications Research Centre (CRC) in Ottawa, a research group led by Ittpiboon, Mongia *et al.* was responsible for some other important works on DRAs in this decade as well [34, 35].

Since then, different characteristics of DRAs were examined as well as different feeding methods and complex shapes. However, DRAs with multiple bands, circular polarization, pattern diversity, and broadband, to name just a few features, are still in the spotlight due to their numerous advantages when compared to metallic antennas such as design flexibility, small size, easy excitation, and high efficiency of radiation [36]. The most important characteristics of DRAs will be presented in the following section.

1.3 Definition and Main Characteristics of the DRA

Dielectric resonator antennas are resonant antennas that consist of a block of low-loss dielectric material that is normally mounted over a metallic ground plane. The resonance frequency of a DRA is a function of its shape, size, and relative permittivity ε_r. Also, it is reported in the literature the use of dielectrics with ε_r ranging from about 6 to 100, which provides easy control over the size and bandwidth of the DRA. Indeed, small size is usually realized with high ε_r while wide bandwidth is achievable using low permittivity. Moreover, DRAs present high radiation efficiency due to the absence of conductors, which is an advantage when compared with metallic antennas, especially at millimeter-wave frequencies [36].

The DRAs can be designed considering a great variety of shapes and some of them can be seen in Fig. 1.2, which provides a high degree of freedom to the design of this kind of antenna, where each shape can present its particular radiating modes and characteristics. The most popular and traditional shapes are the hemispherical, cylindrical, and rectangular ones, which are shown in Fig. 1.2(a), (b), and (c), respectively. Their design equations for the radiating modes and Q-factor can be easily found in the literature [36]. The hemispherical DRA presents two degrees of freedom to its design, which are its radius a and relative permittivity ε_r. On the other hand, the cylindrical DRA is characterized by its radius a, relative permittivity ε_r, and height h, which leads to one degree of freedom more than the hemispherical case. Finally, the rectangular DRA is ruled by its width w, length l, height h, and relative permittivity ε_r, offering one degree of freedom more than the cylindrical DRA. Note that the rectangular shape is the one used throughout this work and more details about it are given in Section 1.4. Finally, some non-conventional shapes can be used as well, as can be observed in Fig. 1.2(d), (e), and (f), to achieve some given characteristics.

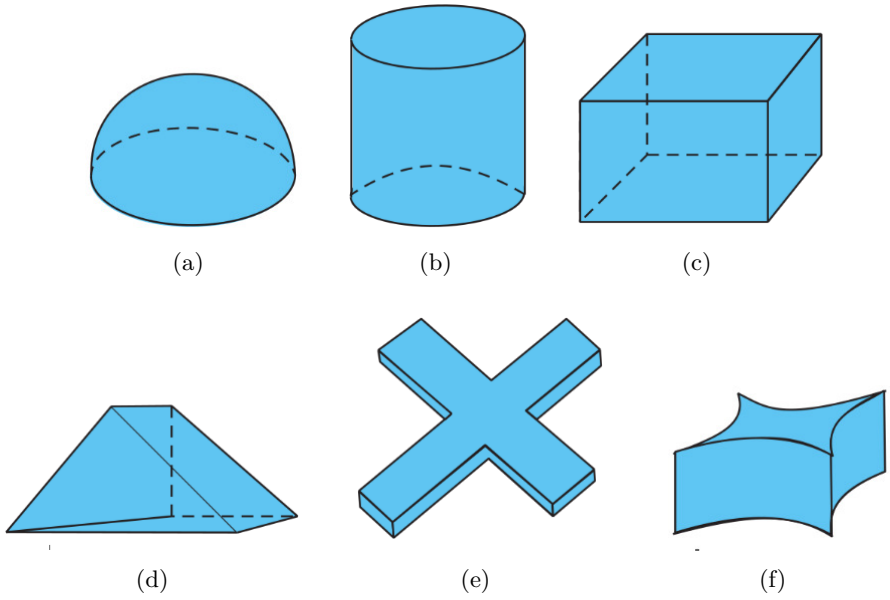

Figure 1.2: Different dielectric shapes used for DRA applications [37].

Dielectric resonator antennas can be excited by different types of feeding methods, such as slots, microstrip lines, probes, dielectric image guides, or co-planar lines. Some of them can be observed in Fig. 1.3. This feature is really important since it facilitates the integration of DRAs with various communication systems. Also, the choice of the proper feeding method depends on the radiating mode of the DRA that needs to be excited, and, then, it is important to know the electromagnetic field distribution of these modes.

Including the aforementioned features, DRAs are attractive for several applications due to their major characteristics, which can be summarized as follow:

- The size of DRAs is proportional to $\lambda_0/\sqrt{\varepsilon_r}$, where λ_0 and ε_r is the free-space wavelength

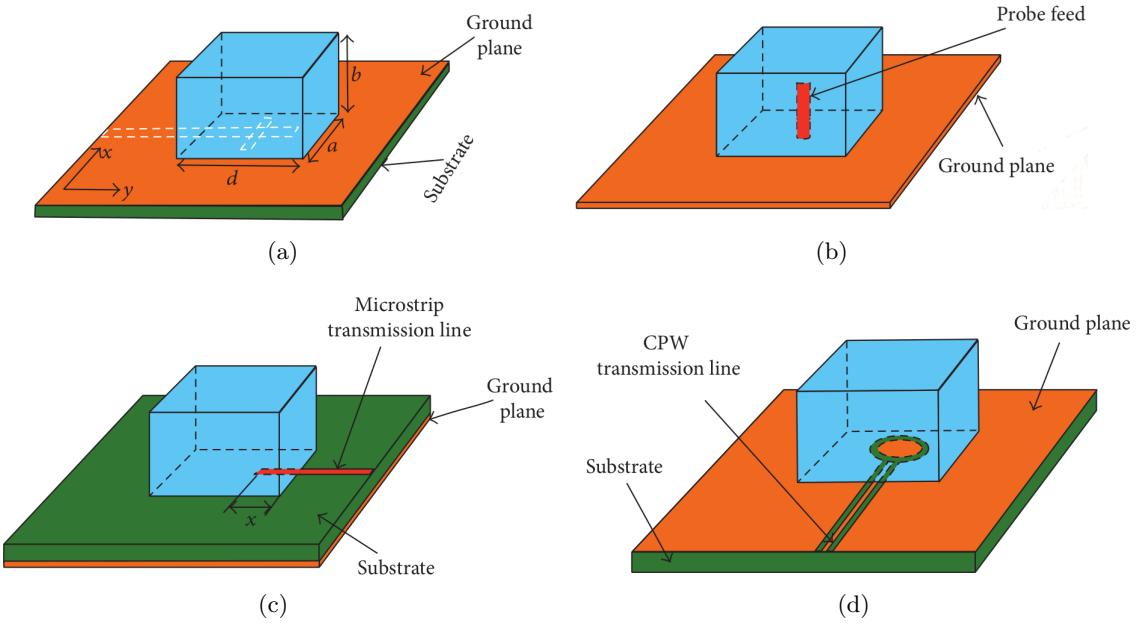

Figure 1.3: Dielectric resonator antennas fed by a (a) microstrip-coupled slot, (b) probe, (c) microstrip transmission line, and (d) coplanar waveguide (CPW) [37].

and dielectric constant of the material, respectively. This feature is important since the size of DRAs can be controlled by choosing the proper ε_r, in which DRAs with ε_r ranging from 6 to 100 were reported in the literature;

- Various radiating modes can be excited to generate different types of radiation patterns, such as broadside or omnidirectional ones, for different coverage requirements;

- The gain, bandwidth, and polarization can be controlled by adjusting the shape of the DRA, choosing the proper feeding method, and/or using multiple excitation ports, for instance.

1.4 The Rectangular DRA

In this section, the expressions for the field distribution, resonance frequencies, and quality-factor of the radiating modes of a rectangular dielectric resonator antenna are developed and discussed. The rectangular shape is considered throughout this work due to its higher degree of freedom when compared to the cylindrical and hemispherical ones.

At first, an isolated rectangular dielectric resonator (DR) is considered, as shown in Fig. 1.4, where the origin of the cartesian coordinate system is placed at the center of the DR. According to Okaya and Barash, the modes in an isolated rectangular DR can be divided into TE and TM [20]. However, the existence of TM modes in rectangular DRs has not been proven experimentally.

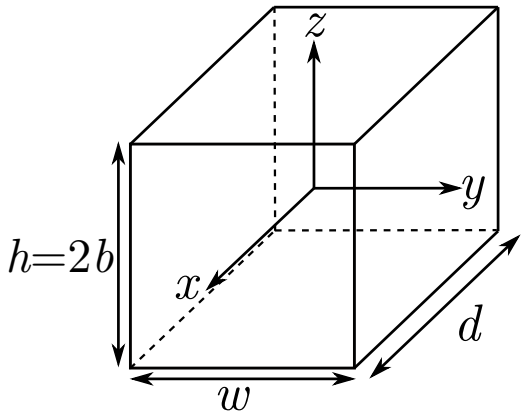

Figure 1.4: Perspective view of an isolated rectangular dielectric resonator.

In this work, the $TE^{x}_{\delta np}$ and $TE^{y}_{m\delta p}$ modes are mainly considered and they resonate like short magnetic dipoles placed along the x- and y-directions, respectively [36]. The value δ represents the fraction of a half-cycle of the field variation in the x- and y-directions for the $TE^{x}_{\delta np}$ and $TE^{y}_{m\delta p}$ modes. Also, m, n, and p are positive integers that represent the field variation along the x-, y-, and z-directions, respectively.

1.4.1 Field Distribution

In this subsection, the Dielectric Waveguide Model (DWM) [38] is used to predict the magnetic and electric field distribution of an isotropic and homogeneous isolated rectangular DR shown in Fig 1.4. For the $TE^{x}_{\delta np}$ modes, for instance, this DR is assumed to be firstly an isolated infinite dielectric waveguide along the x-direction with perfect magnetic conductor (PMC) walls [39], which is then truncated at $x = \pm\frac{d}{2}$. Finally, the field components inside the DR can be derived from the x-directed magnetic potential $\vec{F} = \hat{x}F_x(x, y, z)$ [40]. In this work, the $TE^{x}_{\delta 11}$ and $TE^{x}_{\delta 13}$ modes are mainly used and their magnetic and electric field components can be written as

$$E_x = 0, \tag{1.7}$$

$$E_y = Ak_z\cos(k_x x)\cos(k_y y)\sin(k_z z), \tag{1.8}$$

$$E_z = -Ak_y\cos(k_x x)\sin(k_y y)\cos(k_z z), \tag{1.9}$$

$$H_x = A\frac{k_y^2 + k_z^2}{j\omega\mu_0}\cos(k_x x)\sin(k_y y)\cos(k_z z), \tag{1.10}$$

$$H_y = A\frac{k_x k_y}{j\omega\mu_0}\sin(k_x x)\sin(k_y y)\cos(k_z z), \tag{1.11}$$

$$H_z = A\frac{k_x k_z}{j\omega\mu_0}\sin(k_x x)\cos(k_y y)\cos(k_z z), \tag{1.12}$$

where A is an arbitrary amplitude, $k_x = \delta\frac{\pi}{d}$, $k_y = n\frac{\pi}{w}$, and $k_z = p\frac{\pi}{h}$ denote the wavenumber along the x-, y-, and z-directions inside the resonator, respectively, n and p are odd positive integers, ω is the angular frequency, and μ_0 is the free-space permeability.

To provide a better understanding about the characteristics of the TE modes in a rectangular DR, Fig. 1.5 shows the electric field distribution, *i.e.* $\vec{E} = E_x\hat{x} + E_y\hat{y} + E_z\hat{z}$, of the $\mathrm{TE}^x_{\delta 11}$ and $\mathrm{TE}^x_{\delta 13}$ modes at $x = \frac{d}{2}$ in the yz-plane. In Fig. 1.5(a), one can note that the electric field distribution $\mathrm{TE}^x_{\delta 11}$ mode is similar to an x-directed magnetic dipole. On the other hand, from Fig. 1.5(b), the field distribution of the $\mathrm{TE}^x_{\delta 13}$ mode is similar to an array of three x-directed magnetic dipoles arranged along the z-direction.

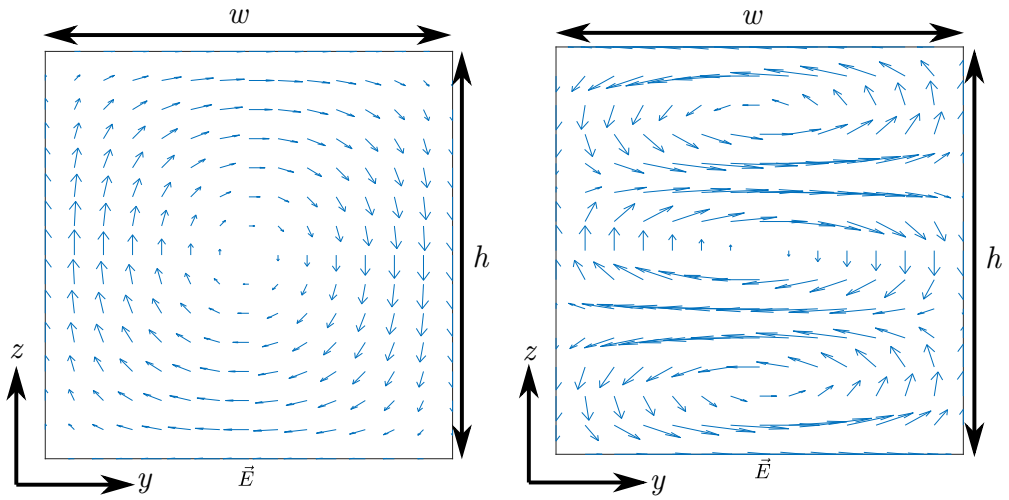

(a) $\mathrm{TE}^x_{\delta 11}$ (b) $\mathrm{TE}^x_{\delta 13}$

Figure 1.5: Electric field distribution of the (a) $\mathrm{TE}^x_{\delta 11}$ and (b) $\mathrm{TE}^x_{\delta 13}$ modes of the isolated rectangular DR at $x = \frac{d}{2}$.

1.4.2 Resonance Frequencies

To calculate the resonance frequencies of the rectangular DR, their faces at $x = \pm\frac{d}{2}$ are truncated with imperfect magnetic walls (IMW) according to Marcatili's approximation [38]. This condition allows the fields to propagate through the walls where they will decay exponentially outside of the resonator. For instance, considering that H_x and H'_x are the x-component of the magnetic field inside and outside the dielectric resonator, respectively, it is possible to state that $H_x = H'_x$ and $\frac{\partial H_x}{\partial x} = \frac{\partial H'_x}{\partial x}$ at $x = \pm d/2$, due to the continuity imposed by boundary conditions at these interfaces. Thus, H'_x can be expressed as

$$H'_x = A'\frac{k_y^2 + k_z^2}{j\omega\mu_0}e^{-jk'_x x}\sin(k_y y)\cos(k_z z), \tag{1.13}$$

where A' is an arbitrary amplitude and k'_x is the wavenumber along the x-direction outside the dielectric resonator. Also, at $x = d/2$, $H_x = H'_x$ can be written as

$$A\cos\left(k_x\frac{d}{2}\right) = A'e^{-jk'_x\frac{d}{2}}, \tag{1.14}$$

and, $\frac{\partial H_x}{\partial x} = \frac{\partial H'_x}{\partial x}$ is represented as

$$-Ak_x\sin\left(k_x\frac{d}{2}\right) = -A'jk'_xe^{-jk'_x\frac{d}{2}}. \tag{1.15}$$

Dividing the equantion (1.15) by (1.14), it is possible to find the following transcendental equation

$$k_x\tan\left(k_x\frac{d}{2}\right) = \sqrt{(\varepsilon_r-1)\,k_0^2-k_x^2}, \tag{1.16}$$

where ε_r is the relative permittivity of the DR. Therefore, using the following separation equation

$$k_x^2+k_y^2+k_z^2 = \varepsilon_r k_0^2, \tag{1.17}$$

the transcendental equation for k_x, k_y, and k_z, it is possible to calculate the resonance frequency of the DR for a given mode.

1.4.3 Quality Factor

The quality factor, or simply Q-factor, is an important figure-of-merit when it comes to DRAs. This parameter is interrelated with the impedance bandwidth of an antenna and there is no way to optimize one of them without affecting the performance of the other one [41]. Moreover, in general, antennas present conducting, radiation, dielectric, and surface-wave losses, and, then, the total quality factor Q_t can be expressed as

$$\frac{1}{Q_t} = \frac{1}{Q_{\text{rad}}}+\frac{1}{Q_c}+\frac{1}{Q_d}+\frac{1}{Q_{sw}}, \tag{1.18}$$

where Q_{rad}, Q_c, Q_d, and Q_{sw} are the quality factors due to radiation (space wave), conduction (ohmic), dielectric, and surface-wave losses, respectively. It is important to point out that for DRAs, $Q_t \approx Q_{\text{rad}}$ is usually considered, since low-loss dielectrics are normally employed and there are no conductor and surface-wave losses.

The fractional impedance bandwidth BW can be calculated from the Q-factor and is found as [36]

$$BW = \frac{\Delta f}{f_0} = \frac{\text{s}-1}{Q_{\text{rad}}\sqrt{\text{s}}}, \tag{1.19}$$

where Δf is the absolute bandwidth, f_0 is the resonance frequency, and s is the maximum

acceptable voltage standing wave ratio (VSWR).

The radiation quality factor Q_{rad} of a DR can be also written as [36]

$$Q_{\text{rad}} = 2\omega \frac{W_e}{P_{rad}}, \tag{1.20}$$

where W_e is the stored energy and P_{rad} is the radiated power. Also, W_e is defined as [17]

$$W_e = \frac{1}{4}\varepsilon \iiint_v |\vec{E}| dv, \tag{1.21}$$

where v denotes the volume of the DRA and $\vec{E} = E_x\hat{x} + E_y\hat{y} + E_z\hat{z}$. For instance, considering the $\text{TE}^x_{\delta 11}$ mode, the stored energy W_e of a rectangular DRA is given by

$$W_e = \frac{\varepsilon_0 \varepsilon_r A^2 dwb}{32} \left[1 + \frac{\sin(k_x d)}{k_x d}\right] \left(k_x^2 + k_z^2\right). \tag{1.22}$$

In [21], it is seen that the TE_{111} modes of a rectangular DR radiate like magnetic dipoles and their radiated power can be represented as

$$P_{rad} = 10 k_0^4 \|\vec{p}_m\|^2, \tag{1.23}$$

where $\vec{p}_m$ is the magnetic dipole moment [42], expressed as

$$\vec{p}_m = \frac{1}{2} \iiint_v \vec{r} \times \vec{J}_p dv, \tag{1.24}$$

and $\vec{r} = x\hat{x} + y\hat{y} + z\hat{z}$ is a vector from the origin, $\vec{J}_p = j\omega\varepsilon_0 (\varepsilon_r - 1)\vec{E}$ is the volume polarization current density, and $\vec{E}$ is the electric field intensity inside the resonator. Applying (1.7), (1.8) and (1.9) in (1.24), the magnetic dipole moment $\vec{p}_m$ can expressed as

$$\vec{p}_m = -j \frac{8A\omega\varepsilon_0 (\varepsilon_r - 1)}{k_x k_y k_z} \sin\left(k_x \frac{d}{2}\right) \hat{x}. \tag{1.25}$$

Therefore, knowing P_{rad} and W_e, the radiation quality factor can be calculated by employing (1.20). Besides, the same reasoning can be used to calculate the radiation quality factor for the $\text{TE}^y_{1\delta 1}$ and $\text{TE}^z_{11\delta}$ modes.

1.5 State-of-the-Art of Multiband DRAs

Nowadays, the exponential technology evolution demands that devices such as UAVs and nanosatellites, for instance, must be connected to each other, to base stations, and/or to

some other devices, which means that normally their antennas must cover different frequency bands for different applications. Moreover, as the size of these devices has been decreasing with each passing day, the use of a single antenna for multiple frequencies instead of multiple ones has become essential. In this context, DRAs can be very useful, since they present a wide variety of radiating modes that can be excited using different techniques. Thus, in this section, a state-of-the-art of multiband DRAs is presented.

In [43], a coplanar waveguide (CPW) is used to feed a dual-band DRA with linear polarization, which can be observed in Fig. 1.6. The antenna operates at 3456 MHz and 4797 MHz with different radiation patterns at each band. More precisely, at the upper band, the HE_{111} mode is excited and presents broadside radiation patterns. At the lower band, the inductive slot radiates by itself, which shows dipole-like patterns.

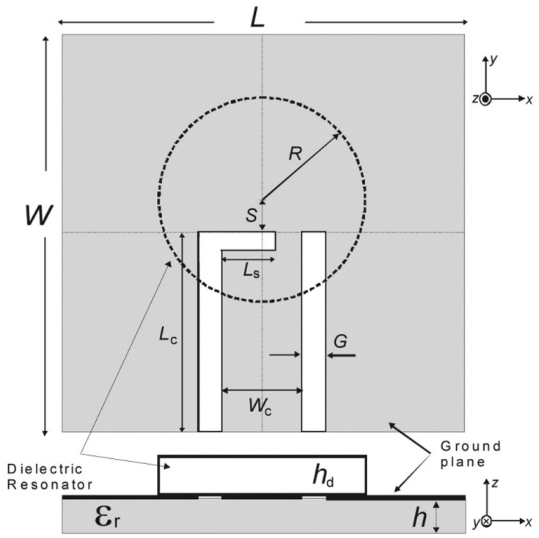

Figure 1.6: Dual-band dielectric resonator antenna fed by a coplanar waveguide [43].

A dual-band linearly-polarized cylindrical DRA with omnidirectional radiation patterns has been proposed in [44], as can be observed in Fig. 1.7. The TM_{011} and TM_{012} modes are excited at 3.5-GHz WiMAX and 5.8-GHz WLAN bands by a probe placed at the center of the DRA. Also, analytical formulas to design this type of antenna at different frequencies with different materials have been developed.

So far, only multiband DRAs with linear polarization were presented. However, the fast-growing development of wireless systems, such as satellite navigation, leads to an increasing interest in circularly-polarized (CP) antennas, since they are less affected by atmospheric conditions and insensitive to the transmitter and receiver orientations. In this context, DRA can be an interesting solution since it presents a relatively wide bandwidth, interesting radiation characteristics, small size, and low cost. Besides, the possibility of employing different feeding techniques and dielectrics with a diversity of shapes and electric properties allows the design of efficient CP DRAs at different frequency ranges with multiband.

The shape of the DRA can play an important role to design a CP antenna since it allows

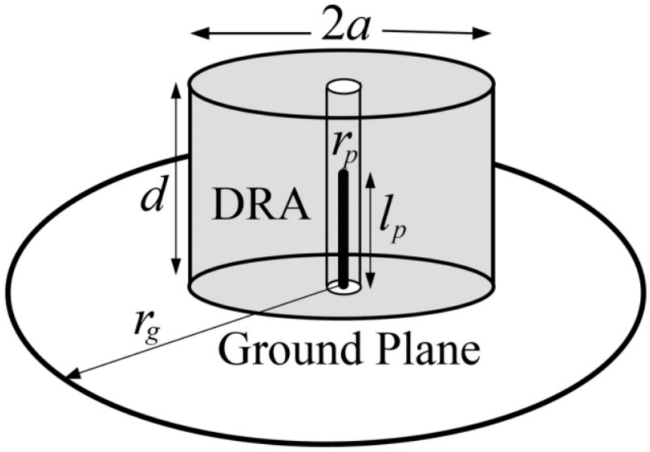

Figure 1.7: Dual-band cylindrical DRA with omnidirectional radiation patterns [44].

the possibility of exciting orthogonal modes with the same amplitude and in-phase quadrature. In the literature, it is possible to find CP DRAs with shapes such as trapezoidal [45], stair-shaped rectangular [46], elliptical [47], and cross-shaped [48]. In most of these examples, the circular polarization happens mainly due to the shape of the DRA itself.

In [49], a cylindrical DRA is used to achieve CP and dual-band, where a pair of degenerate modes are excited at each frequency band, *i.e.* the HEM^{x}_{111} and HEM^{y}_{111} modes are used at the lower band and the HEM^{x}_{113} and HEM^{y}_{113} modes at the upper band. These modes are excited by a quadrature strip-fed, as can be observed in Fig. 1.8. One can note that a complex feeding method is here necessary to have dual-band and circular polarization.

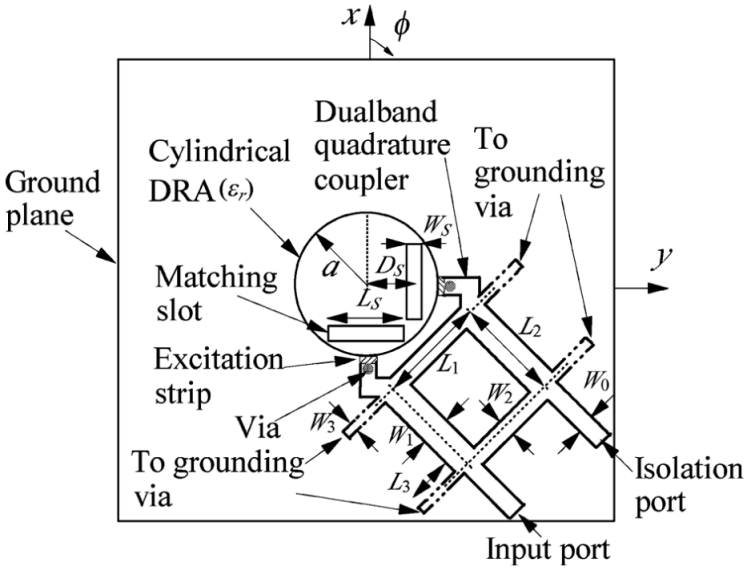

Figure 1.8: Top view of a dual-band CP cylindrical DRA [49].

In [50], both shape and feeding are combined to create a dual-band circularly-polarized

DRA, as can be seen in Fig. 1.9. The fundamental TE_{111} and higher-order TE_{121} modes are excited at the lower band, and the TE_{131} mode is employed at the upper band. Also, the DRA is fed by a cross-slot, where the length of each arm is adjusted to ensure the CP at both bands. Thus, to achieve these results, it is necessary to manipulate both the shape of the DRA and the dimensions of the cross-slot. However, as the authors are dealing with three sets of different modes, the radiation patterns are different depending on the frequency band and cut plane.

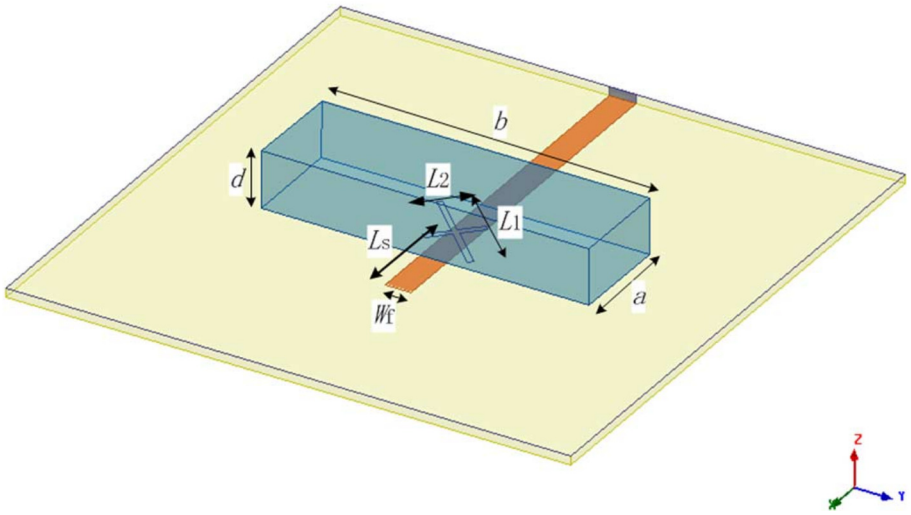

Figure 1.9: Perspective view of a dual-band CP DRA fed by a cross-slot [50].

The shape of a rectangular DRA can be manipulated for a CP and dual-band operation [51], as can be seen in Fig. 1.10. The quasi-TE_{111} and -TE_{113} modes are excited by a simple slot and, to generate CP fields, two opposite corners of the DRA are truncated. Also, a groove is introduced along one of the diagonal of the DRA to tune mainly the upper-band AR.

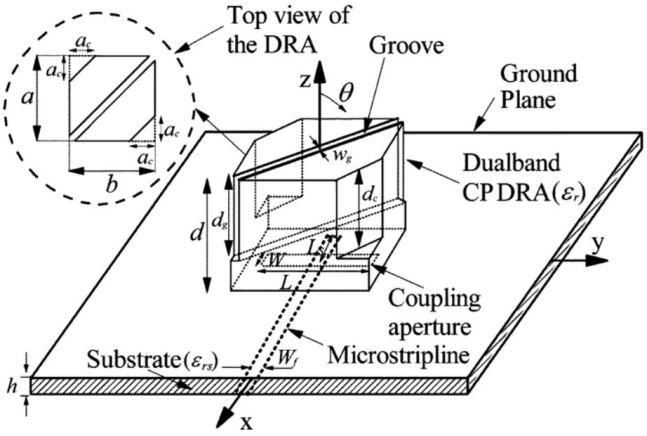

Figure 1.10: Perspective view of a singly-fed dual-band CP DRA [51].

In [52], the fundamental TE_{111} and higher-order TE_{113} modes of a rectangular DRA are excited to operate around 3.04 GHz and 3.65 GHz, respectively. This antenna is fed by two

strips, as can be seen in Fig. 1.11, so that, at the lower band, the TE^{x}_{111} and TE^{y}_{111} modes are excited and, at the upper band, the TE^{x}_{113} and TE^{y}_{113} modes are used. Thus, as this antenna is square-based, the circular polarization at two bands is only achieved due to the control of the phase of its two ports.

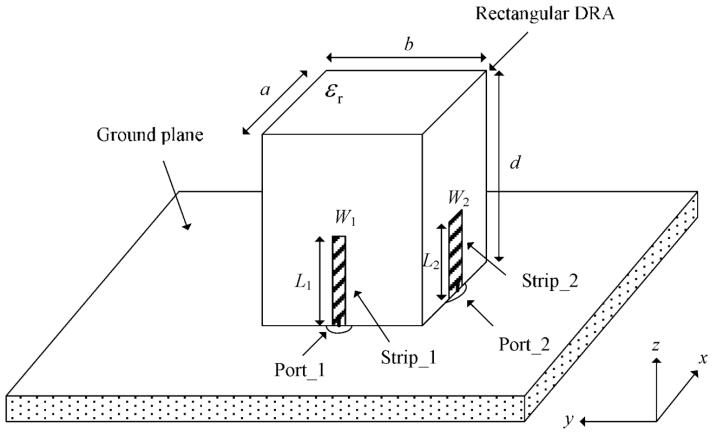

Figure 1.11: Perspective view of the dual-band circularly-polarized DRA fed by two ports [52].

In [53], a dual-band circularly-polarized DRA is proposed for the B3 and B1 bands of the Compass Navigation Satellite System (CNSS), as can be observed in Fig. 1.12. In this work, a cross-slot is used to feed a rectangular DRA with a square cross-section, and the TE_{111} and TE_{113} modes are excited. The width and length of the arms of the cross are carefully chosen to have, at each frequency band, two pairs of near-degenerate orthogonal modes with near-equal amplitudes and in-phase quadrature, thus determining a dual-band CP operation.

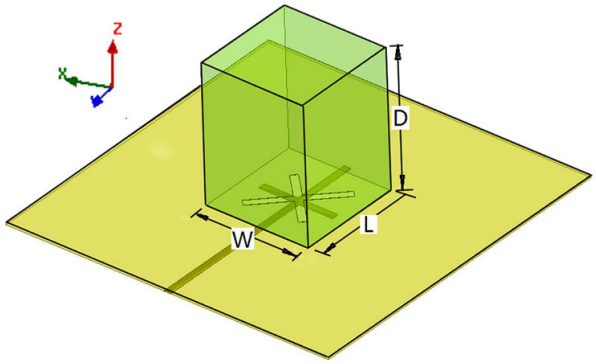

Figure 1.12: Perspective view of the dual-band circularly-polarized DRA fed by a cross-slot [53].

Figure 1.13 shows a wide dual-band circularly-polarized stacked rectangular DRA [54]. The quasi-TE_{111} and slot modes are employed at the lower band, and quasi-TE_{113} and quasi-TE_{115} modes are used at the upper band, and all of these modes are excited by an unbalanced cross-slot. Also, the DRA consists of two stacked DRAs with the same height, same permit-

tivity, and different square cross-sections.

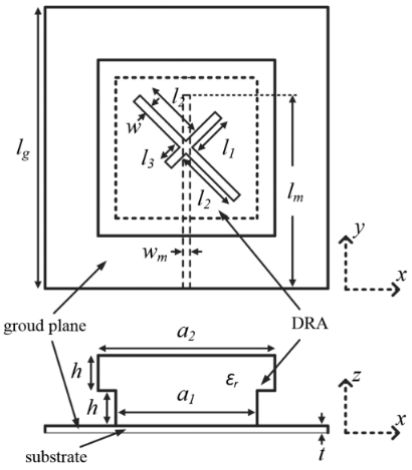

Figure 1.13: Geometry of the wide dual-band CP stacked rectangular DRA [54].

1.6 Conclusion

This chapter introduced the dielectric resonator antennas by explaining their physical shapes, different feeding methods, and characteristics, and showing the potential of this type of antenna for different applications at different frequency ranges. Also, different techniques are presented to achieve circular polarization, such as using multiple ports, manipulating the feeding network, changing the physical shape of the DRA, and so on. However, none of them employed the control of the dielectric properties of the DRA to satisfy the CP conditions at two bands. To do so, it is necessary to know the behavior of the electric field distribution, resonance frequencies, and Q-factor of the radiating modes of the DR and to be able to feed them accordingly, which is presented in Section 1.4. Of course, one has also to know to control the permittivity of a dielectric medium. Therefore, all of these points will be addressed in the following chapters.

Chapter 2

Inhomogeneous Dual-Band DRA with Linear Polarization

Contents

In this chapter, a dual-band dielectric resonator antenna is proposed to operate at the L5 (1176.45 MHz ± 10.23 MHz) and L1 (1575.42 MHz ± 10.23 MHz) bands of the Global Navigation Satellite System (GNSS). In Section 2.1, the DRA is initially designed to excite the $TE^{y}_{1\delta1}$ and $TE^{x}_{\delta11}$ orthogonal modes to cover both L5 and L1 bands, respectively. However, the presence of an undesirable higher-order mode leads to the distortion of the expected radiation pattern at the L1 band. To overcome this issue, a method to shift this mode away from the L1 band is presented and the main results are discussed in Section 2.2. It consists in drilling an air cavity inside the dielectric resonator to obtain an inhomogeneous material.

2.1 Homogeneous Linearly-Polarized Dual-Band DRA

A dual-band rectangular DRA is here considered due to its main advantages when compared to other classic shapes, as described in Section 1.3. The first step to design an antenna is to define its operating frequency and, then, the L5 (1176.45 MHz ± 10.23 MHz) and L1 (1575.42 MHz ± 10.23 MHz) bands of the GNSS are chosen in this example. For this kind of application, it is interesting to have broadside radiation patterns, which can be achieved by exciting the fundamental $TE^{x}_{\delta11}$ and $TE^{y}_{1\delta1}$ modes of a rectangular DRA since these modes have magnetic dipole-like patterns as observed from their electric field distributions in Fig. 2.1, where a homogeneous dielectric resonator (DR) over an infinite ground plane is considered.

Due to the field distribution of the $TE^{y}_{1\delta1}$ and $TE^{x}_{\delta11}$ modes, a coaxial probe is used to excite them and the configuration of the dual-band DRA can be observed in Fig. 2.2, where w, d, b, and ε_r are the width, depth, heigth, and relative permittivity of the DRA, respectively, which is mounted over a metallic ground plane. Using the Dielectric Waveguide Model (DWM) and after some optimization on Ansys HFSS so that the $TE^{x}_{\delta11}$ and $TE^{y}_{1\delta1}$

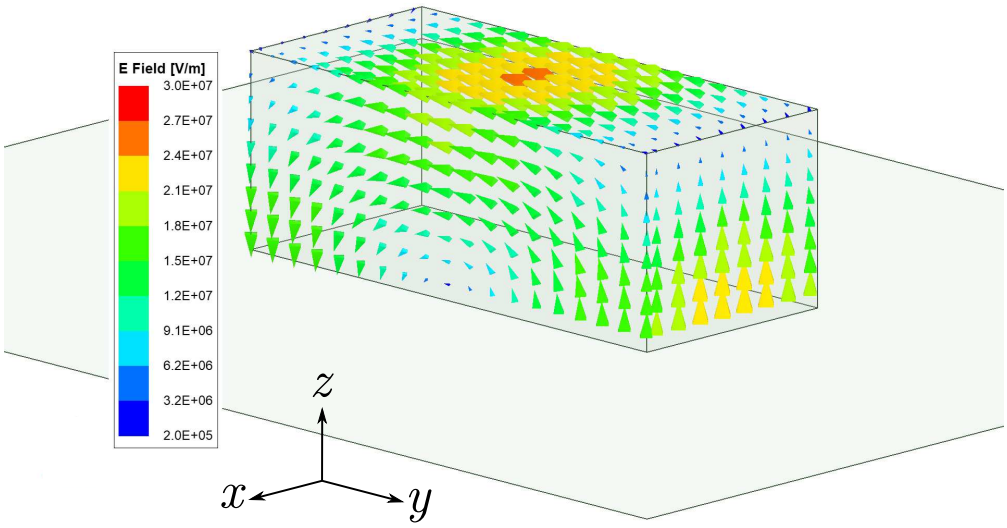

(a) $\mathrm{TE}^{x}_{\delta 11}$

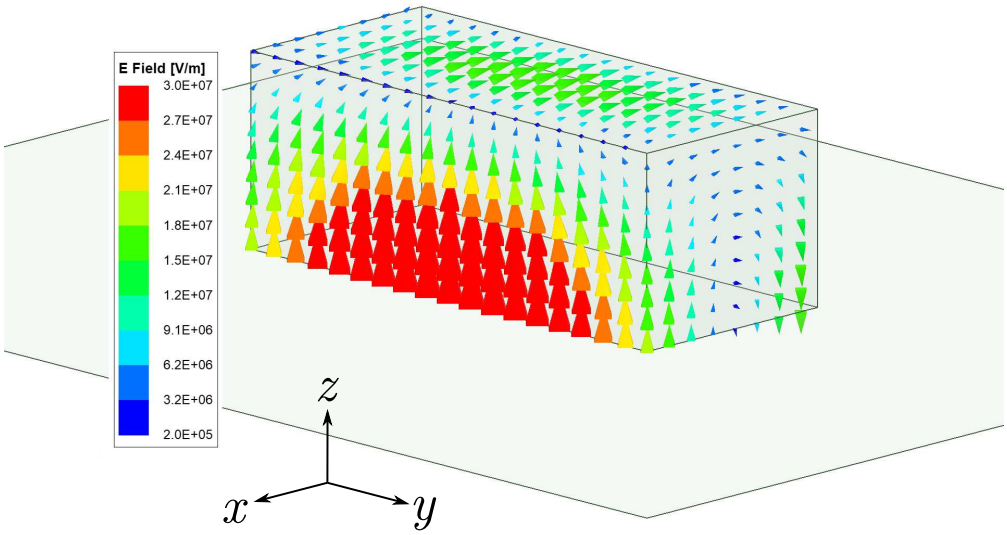

(b) $\mathrm{TE}^{y}_{1\delta 1}$

Figure 2.1: Electric field distribution of the (a) $\mathrm{TE}^{x}_{\delta 11}$ and (b) $\mathrm{TE}^{y}_{1\delta 1}$ modes considering a homogeneous DR over an infinite ground plane.

modes resonate around the L5 and L1 bands, respectively, the parameters of the DRA are defined as $d = 53.2$ mm, $w = 22.3$ mm, $b = 25.5$ mm, $p_1 = 3$ mm, $p_2 = 0$ mm, $h_p = 18$ mm, $D = 200$ mm, and $\varepsilon_r = 23$. Considering these parameters, the reflection coefficient in dB is shown in Fig. 2.3. One can note that the simulated impedance bandwidth ($|S_{11}| < 10$ dB) is 2.39% (1158 MHz - 1186 MHz) and 6.33% (1529 MHz - 1629 MHz) at the L5 and L1 bands, respectively.

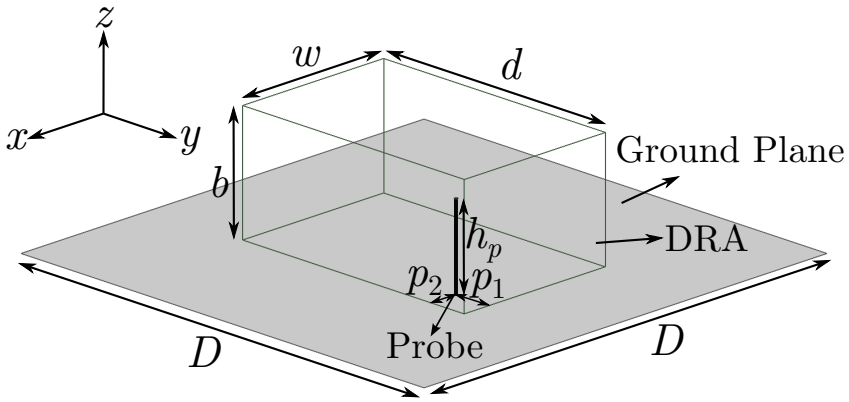

Figure 2.2: Dual-band linearly-polarized rectangular DRA.

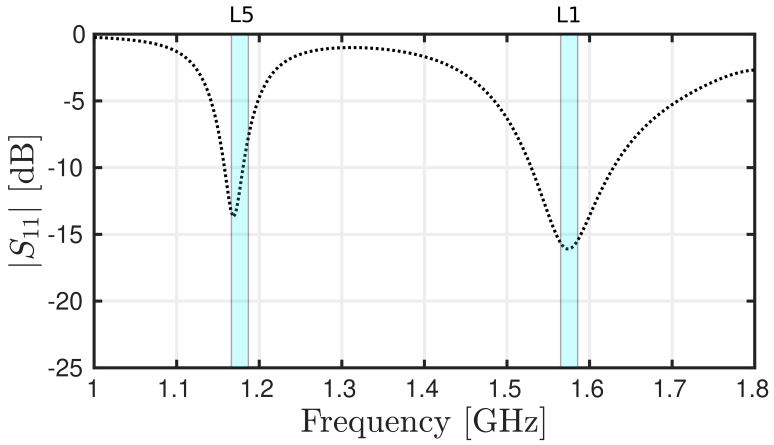

Figure 2.3: Simulated reflection coefficient of the proposed dual-band linearly-polarized DRA.

Figure 2.4 shows the θ- and ϕ-components of the simulated gain patterns, in dBi, of the dual-band DRA in the xz- and yz-planes at the center frequencies of the L5 and L1 bands. At the lower band, as expected for the $\mathrm{TE}^{x}_{\delta 11}$ mode, broadside patterns are observed for both planes. Note that this DRA is linearly polarized whereas GNSS receiving systems usually require circularly-polarized antennas. At the upper band, the radiation patterns are not as expected for the $\mathrm{TE}^{y}_{1\delta 1}$. To be more specific, in xz-plane, the θ-component of the gain for the DRA presents a null for $\theta = 285°$, which creates a blind spot, and the direction of the main lobe is shifted to around 30° as well. Therefore, it is necessary to investigate the reasons behind this unexpected result. Note also that the polarization is still linear but orthogonal to the one in the L5 band as expected.

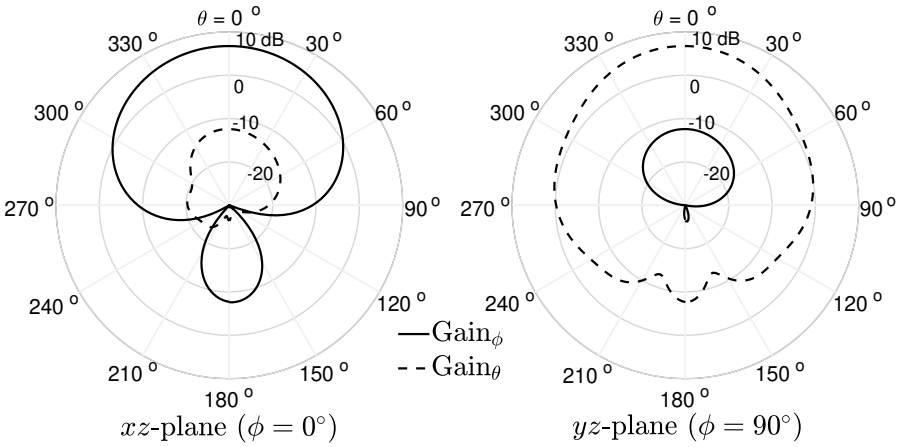

(a) $f = 1176.45$ MHz

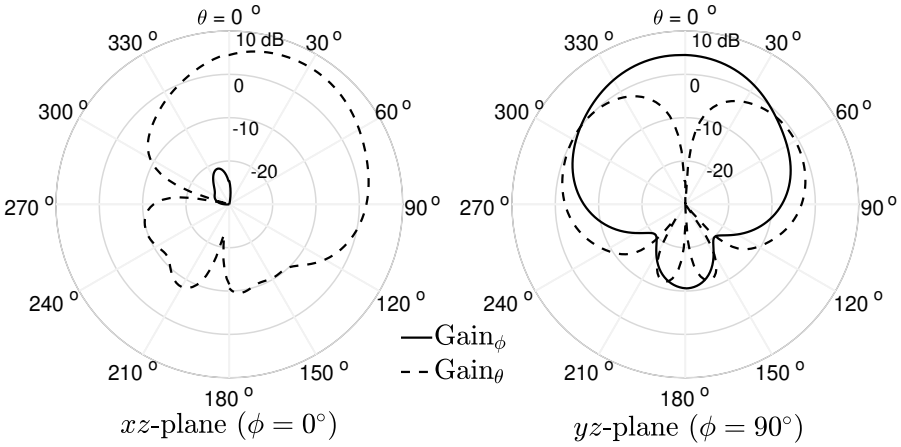

(b) $f = 1575.42$ MHz

Figure 2.4: Simulated gain patterns of the dual-band linearly-polarized DRA at the (a) L5 and (b) L1 bands.

As the radiation patterns of the fundamental modes are well-known, this unexpected result for the $\text{TE}^y_{1\delta1}$ mode may happen due to the presence of a higher-order mode that is being excited around the L1 band. To investigate this, the Eigenmode solution of Ansys HFSS. A rectangular dielectric resonator (DR) is considered without any sources and over an infinite metallic ground plane. The DR is slightly redesigned so that the $\text{TE}^x_{\delta11}$ and $\text{TE}^y_{1\delta1}$ resonate at the L5 and L1 bands, respectively, and, thus, the parameters of the DR are $d = 53$ mm, $w = 23$ mm, $b = 25.5$ mm, and $\varepsilon_r = 23$. Table 2.1 presents the results of the Eigenmode analysis. It is observed that the higher-order mode $\text{TE}^x_{\delta21}$ resonates at 1.575 GHz that is to say in the vicinity of the expected $\text{TE}^y_{1\delta1}$ mode. Due to its field distribution shown in Fig. 2.5, one can note that this mode can be excited by our coaxial probe. Besides, the $\text{TE}^x_{\delta21}$

mode can be viewed as two equivalent magnetic dipoles along the x-direction that will modify the final radiation pattern in the L1 band. Therefore, some strategy must be employed to shift this undesirable mode away from the L1 band.

Mode	**Frequency**	Q**-factor**
$\mathrm{TE}^{x}_{\delta 11}$	1.175 GHz	20.37
$\mathrm{TE}^{y}_{1\delta 1}$	1.574 GHz	14.66
$\mathrm{TE}^{x}_{\delta 21}$	1.575 GHz	12.42

Table 2.1: Resonance frequencies and Q-factor of the $\mathrm{TE}^{y}_{1\delta 1}$, $\mathrm{TE}^{x}_{\delta 11}$, and $\mathrm{TE}^{x}_{\delta 21}$ modes for the homogeneous DR.

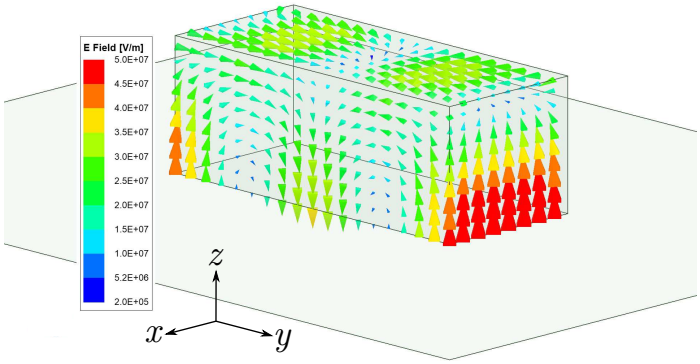

Figure 2.5: Electric field distribution of the $\mathrm{TE}^{x}_{\delta 21}$ mode considering a homogeneous DR over an infinite ground plane.

2.2 Inhomogeneous Linearly-Polarized Dual-Band DRA

Considering the field distribution of the modes at issue, one way to shift the $\mathrm{TE}^{x}_{\delta 21}$ away from the L1 band is to locally control the electric permittivity of the dielectric in a region where the electric field distributions are weak for the fundamental modes and strong for the $\mathrm{TE}^{x}_{\delta 21}$ one. Also, as this undesirable mode is resonating at the upper band, one strategy would be to consider an inhomogeneous DRA to increase its resonance frequency by decreasing the electric permittivity at the center of the DRA.

In this context, we propose to increase the resonance frequency of the $\mathrm{TE}^{x}_{\delta 21}$ mode by adding an air cavity in the center of the DRA. To understand the effect of this cavity, the Eigenmode solution of Ansys HFSS is used with the DR configuration shown in Fig. 2.6. Considering $\varepsilon_r = 23$, $d = 53$ mm, $w = 23$ mm, $b = 25.5$ mm, $d_1 = 15$ mm, and $w_1 = 15$ mm, the height of the cavity b_1 is varied and the resonance frequencies of $\mathrm{TE}^{y}_{1\delta 1}$, $\mathrm{TE}^{x}_{\delta 11}$, and $\mathrm{TE}^{x}_{\delta 21}$ modes are tracked, as can be observed in Fig. 2.7(a). One can observe that the higher-order mode $\mathrm{TE}^{x}_{\delta 21}$ is much more sensible than the fundamental ones as b_1 varies. More precisely, from $b_1 = 0$ mm to $b_1 = 18$ mm, the resonance frequencies of the $\mathrm{TE}^{x}_{\delta 11}$, $\mathrm{TE}^{y}_{1\delta 1}$, and $\mathrm{TE}^{x}_{\delta 21}$ increase by 7.24%, 6.04%, and 20.82%, respectively. Moreover, Fig. 2.7(b) shows that the

Q-factors of the fundamental modes are inversely proportional to b_1 while the Q-factor of the $\mathrm{TE}^x_{\delta 21}$ mode is directly proportional to it. Therefore, the aforementioned results demonstrate that an air cavity can be employed to avoid the presence of the $\mathrm{TE}^x_{\delta 21}$ mode around a given frequency.

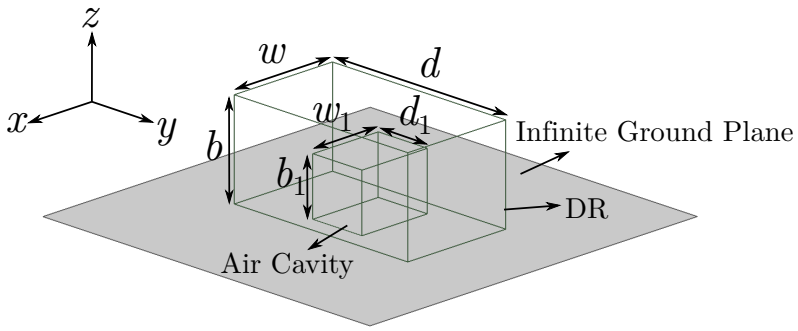

Figure 2.6: Dual-band DR with an air cavity over an infinite ground plane.

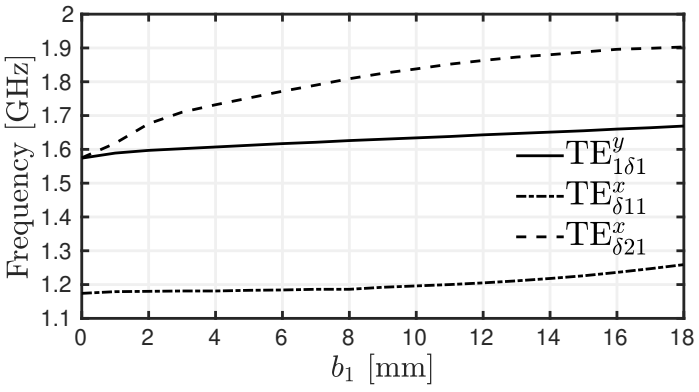

(a)

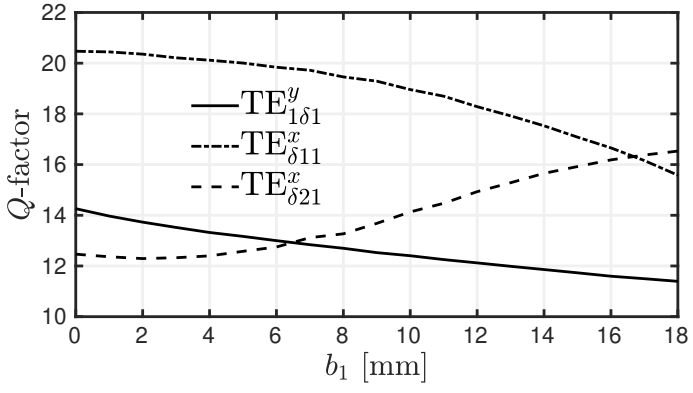

(b)

Figure 2.7: Curves of (a) resonance frequencies and (b) Q-factors of $\mathrm{TE}^y_{1\delta 1}$, $\mathrm{TE}^x_{\delta 11}$, and $\mathrm{TE}^x_{\delta 21}$ modes for different values of height b_1 of the air cavity.

As the previous analysis considered a simple DR without any sources and with an infinite ground plane, the dual-band antenna must be optimized considering a coaxial probe feeding and finite ground plane. The new parameters of the DRA are $d = 54$ mm, $w = 25$ mm, $b = 25.5$ mm, $d_1 = 9$ mm, $w_1 = 20$ mm, $b_1 = 15$ mm, $p_1 = 3$ mm, $p_2 = 2$ mm, $h_p = 17$ mm, $D = 200$ mm, and $\varepsilon_r = 23$. Its configuration can be observed in Fig. 2.8. Considering these values, the reflection coefficient is calculated and compared to the DRA without cavity proposed in the previous section, as shown in Fig. 2.9. As expected both antennas are well-matched at the L5 and L1 bands, and the antenna with air cavity has simulated impedance bandwidth ($| S_{11} | < 10$ dB) of 3.24% (1153 MHz - 1191 MHz) and 10.07% (1490 MHz - 1648 MHz). We observe wider bandwidth that can be explained by the decreasing of the Q-factors of both $\mathrm{TE}^{y}_{1\delta 1}$ and $\mathrm{TE}^{x}_{\delta 11}$ modes due to the air cavity.

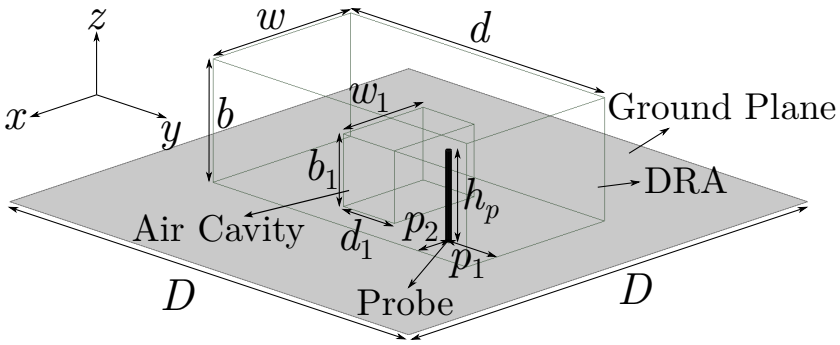

Figure 2.8: Proposed inhomogeneous dual-band linearly-polarized DRA.

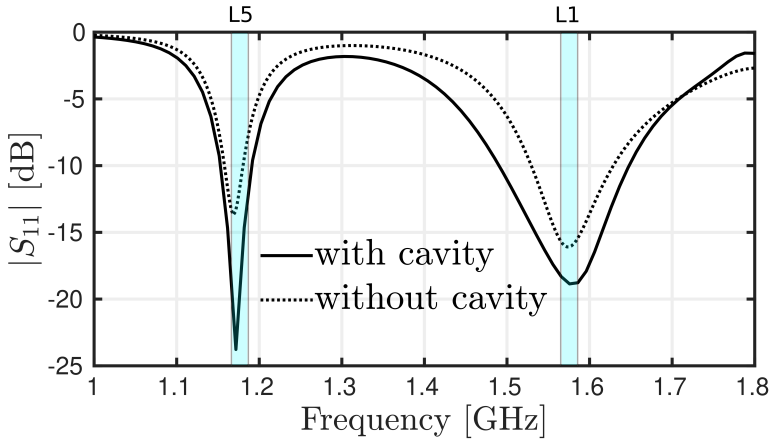

Figure 2.9: Simulated reflection coefficient of the dual-band linearly-polarized DRA with and without air cavity.

Figure 2.10 shows the simulated gain patterns of the DRA with and without air cavity at $\phi = 0°$ and $\phi = 90°$ planes calculated at the center frequencies of the L5 and L1 bands. At the lower band, the gain patterns are the same for both models, as expected. At the upper band, one can note that there is no angular shift anymore with the presence of the air cavity, as expected for the $\mathrm{TE}^{y}_{\delta 11}$ mode. Therefore, the gain patterns demonstrate that the use of an inhomogeneous DR is efficient to get rid of a given undesirable radiating mode.

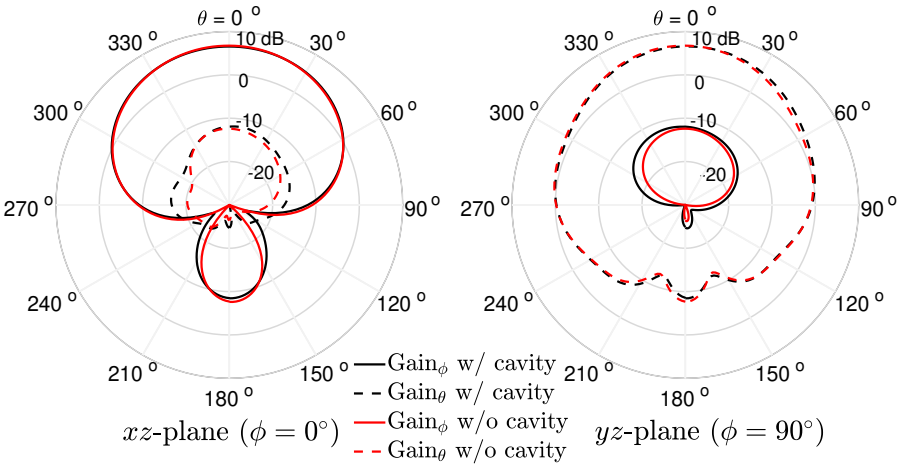

(a) $f = 1176.45$ MHz

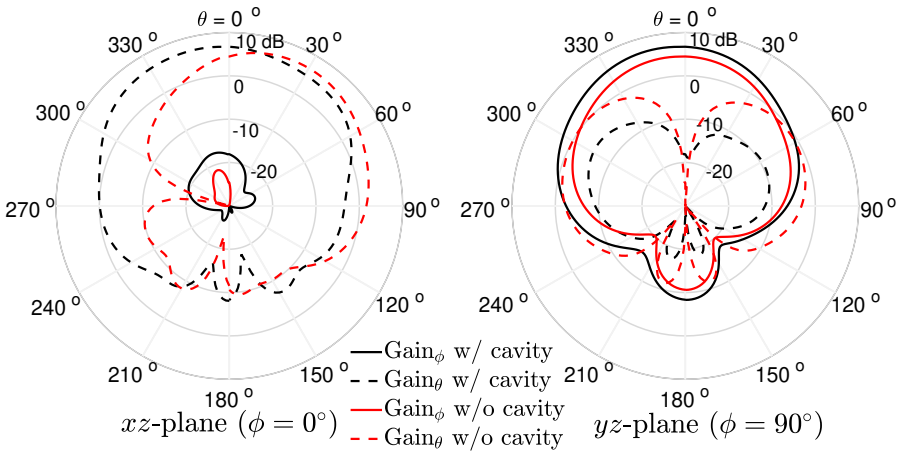

(b) $f = 1575.42$ MHz

Figure 2.10: Simulated gain patterns of the dual-band linearly-polarized DRA with and without the air cavity at (a) L5 and (b) L1 bands.

In order to better understand the effect of the presence of the air cavity in the radiation pattern of the $\mathrm{TE}^{y}_{1\delta1}$ mode, a parametric analysis is presented for different values of b_1, where $d = 54$ mm, $w = 25$ mm, $b = 25.5$ mm, $d_1 = 9$ mm, $w_1 = 20$ mm, $p_1 = 3$ mm, $p_2 = 2$ mm, $h_p = 17$ mm, $D = 200$ mm, and $\varepsilon_r = 23$. Figure 2.11 shows the θ-component of the gain pattern calculated at central frequency of the L1 band in the $\phi = 0°$ plane for different values of b_1. It is possible to observe how the pattern is getting closer to the one expected for the $\mathrm{TE}^{y}_{1\delta1}$ modes as the value of b_1 increases, since, at the same time, the $\mathrm{TE}^{x}_{\delta21}$ mode is moving away from the L1 band.

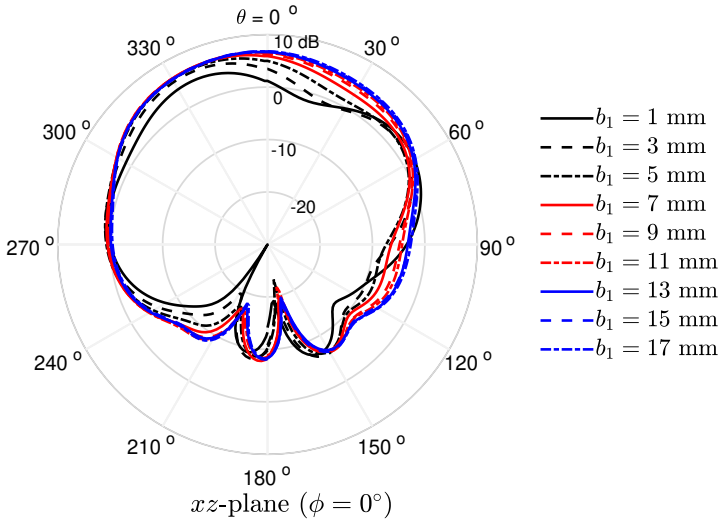

Figure 2.11: Simulated θ-component of the gain pattern at the L1 band in the $\phi = 0°$ plane for different values of b_1.

Note that the presence of an air cavity means that the overall permittivity of the DR is reduced and, then, the size of the DRA tends to increase. As a matter of comparison, Table 2.2 shows the main dimensions of the DRA, where both models are designed so that the $\mathrm{TE}^{x}_{\delta11}$ and $\mathrm{TE}^{y}_{\delta11}$ resonate at the center of the L5 and L1 bands, respectively. Besides, the percentage difference is presented as well, which is calculated as $(\mid X_{\mathrm{nocavity}} - X_{\mathrm{cavity}} \mid / X_{\mathrm{nocavity}})$, where X_{nocavity} and X_{cavity} are the parameters of the DRA without and with cavity, respectively. Thus, one can note that the volume of the dielectric with air cavity is 13.81% higher than without it.

	w	d	b	Volume
DRA without cavity	22.3 mm	53.2 mm	25.5 mm	30.25 cm^3
DRA with cavity	25 mm	54 mm	25.5 mm	34.43 cm^3
Percentage difference	12.11%	1.50%	0%	13.81%

Table 2.2: Parameters of the dual-band linearly-polarized DRA with and without air cavity.

Practically, circularly-polarized GNSS antennas are more suitable than linear-polarized ones, due to their immunity to multipath distortion and the Faraday rotation effect, and

insensitivity to the transmitter and receiver orientations. To do so, for a dual-band operation, one may excite a pair of orthogonal modes around the same frequency with the same amplitude and in phase quadrature at each band. For the proposed dual-band DRA with the air cavity, the axial ratio is shown in Fig. 2.12 and it is possible to note that this antenna does not have circular polarization as expected. Indeed, the values of axial ratio are higher than 3 dB at the L5 and L1 bands.

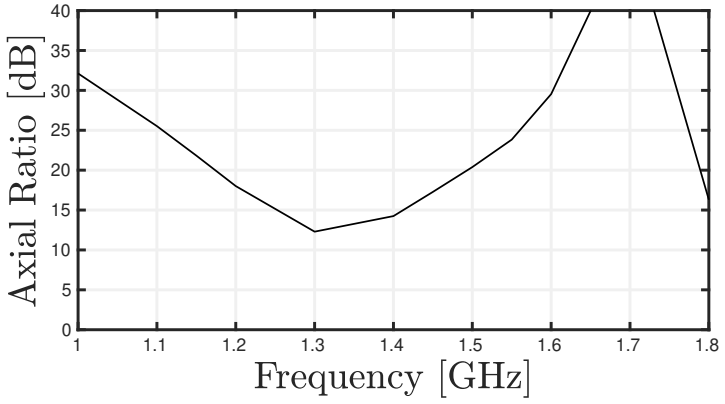

Figure 2.12: Simulated axial ratio of the dual-band linearly-polarized DRA with air cavity in the boresight direction ($\theta = 0°$ and $\phi = 0°$).

Using the dual-band LP DRA as a starting point to design a CP antenna, some structures were investigated to try to have circular polarization at two bands. For example, L- and cross-shaped DRAs have been studied as observed in Fig. 2.13. These designs intend to excite with only one probe a pair of orthogonal modes at each band using two identical DRAs with an air cavity at the center to get rid of the higher-order modes in the operational bandwidth. More precisely, at the L5 band, the $\mathrm{TE}^{x}_{\delta 11}$ of the DRA 2 and the $\mathrm{TE}^{y}_{1\delta 1}$ of the DRA 1 should be excited at the L1 band while the $\mathrm{TE}^{x}_{\delta 11}$ of the DRA 1 and the $\mathrm{TE}^{y}_{1\delta 1}$ of the DRA 2 should be excited at L5 band. At each band, the orthogonal modes have the same resonance frequency and amplitude, due to the position of the probe. However, we did not succeed in achieving the phase quadrature with this approach. Some other small variations from these models were investigated but it was not possible to have circular polarization at two bands using only one feeding point. We thus decided to explore another approach as shown in the next chapter.

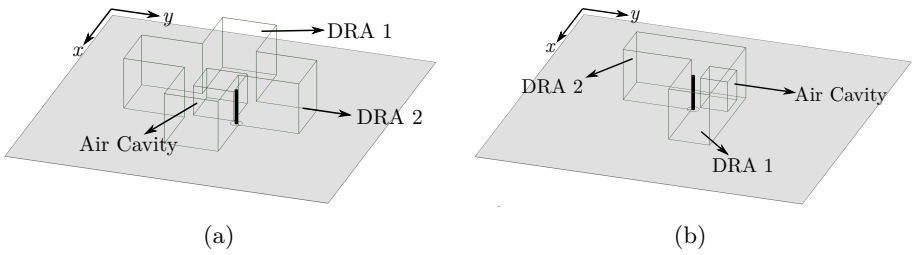

Figure 2.13: (a) Cross- and (b) L-shaped dual-band dielectric resonator antennas with air cavity.

2.3 Conclusion

An approach to shifting an undesirable mode away from a given frequency band is presented. It consists in locally controlling the permittivity of the DRA. To be more specific, a rectangular DR is designed so that the fundamental $TE^{x}_{\delta 11}$ and $TE^{y}_{1\delta 1}$ modes resonate at the GNSS L5 and L1 bands, respectively. However, the presence of the higher-order $TE^{x}_{\delta 21}$ mode is observed around the L1 band and, then, distorts the expected radiation pattern. To overcome this issue, an air cavity is introduced at the center of the DR leading to an inhomogeneous dielectric material. The results of reflection coefficient and radiation patterns demonstrate the efficiency of this approach for this type of issue.

Some other structures were investigated to achieve circular polarization in two bands. Nonetheless, it was not possible to achieve CP using only one feeding probe considering L- and cross-shaped DRAs, since the condition of the phase quadrature for the pair of orthogonal modes was not respected.

Even though we did not succeed to have a dual-band and CP antenna with the dielectric with an air cavity using only one probe, the development described in this chapter can open up new possibilities to do it. So far, two isotropic dielectrics were used to locally control the permittivity and, thus, controlling the resonance frequency of a given mode. However, instead of using only isotropic materials, the possibility of using anisotropic dielectrics could be explored to have circular polarization and this approach will be discussed in the following chapters.

Chapter 3

Inhomogeneous and Anisotropic Dual-Band DRA with Circular Polarization

Contents

In the previous Chapter, a rectangular inhomogeneous dielectric has been considered to design a dual-band DRA, where the inhomogeinity is obtained by adding an air cavity in the center of the antenna. However, it has not been possible to achieve circular polarization due to lack of degrees of freedom of this approach. This Chapter presents a dual-band DRA with circular polarization, in which the electrical permittivity of the dielectric resonator is locally manipulated to achieve the expected performance. In Section 3.1, the principle of operation of the proposed DRA is introduced with the support of the Eigenmode solution of Ansys HFSS, which is based on the natural resonance of the dielectric resonator by itself and the radiating $TE^{x}_{\delta 11}$, $TE^{y}_{1\delta 1}$, $TE^{x}_{\delta 13}$, and $TE^{y}_{1\delta 3}$ modes. Moreover, in Section 3.2, the proposed DRA is optimized taking into account a feeding slot, and results such as reflection coefficient, axial ratio, efficiency, and radiation pattern are presented. In Section 3.3, a parametric analysis of the DRA is made and a design guideline is presented. Finally, in Section 3.4, the relation between the 3-dB axial ratio bandwidth and the volume of the DRA is discussed.

3.1 Principle of Operation

The circular polarization in single-fed antennas is often achieved by exciting two orthogonal modes with the same amplitude and in phase quadrature at the same operational frequency. Considering a square-based rectangular DRA over an infinite ground plane as shown in Fig. 3.1, for instance, the fundamental $TE^{x}_{\delta 11}$ and $TE^{y}_{1\delta 1}$ modes could be used to achieve CP around

a given frequency. Both modes can be modeled as a dual-parallel RLC equivalent circuit as described and developed in [55, 56]. From this approach, the resonance frequency where the perfect circular polarization happens, *i.e.* axial ratio equal to 0 dB, can be predicted by using the following equations

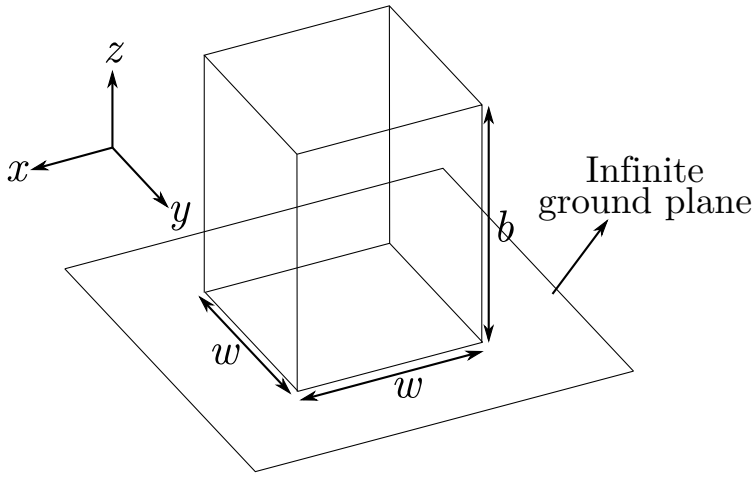

Figure 3.1: Perspective view of a square-based rectangular DRA over an infinite ground plane.

$$f_{01} \simeq \frac{f_1}{\left(1 - \frac{1}{2Q_1}\right)}, \tag{3.1}$$

$$f_{02} \simeq \frac{f_2}{\left(1 + \frac{1}{2Q_2}\right)}, \tag{3.2}$$

where the CP happens at f_0 when $f_0 = f_{01} = f_{02}$. In these equations, f_1 and f_2 are the resonance frequencies of the orthogonal modes, with f_1 lower than f_2, and Q_1 and Q_2 are their respective Q-factors. The goal of these equations is to find a good frequency shift between f_1 and f_2 that gives the phase shift and amplitudes necessary to have circular polarization, which happens when $f_{01} = f_{02}$. To illustrate this condition, Fig. 3.2 presents a simplified drawing of the quality factor as a function of the frequency of two orthogonal modes. For instance, in Fig. 3.2(a), there is frequency shift between f_1 and f_2 but not enough to make $f_0 = f_{01} = f_{02}$. In this case, it necessary to increase this frequency shift to fulfill the CP conditions, which is illustrated in Fig. 3.2(b), where $f_0 = f_{01} = f_{02}$.

In a previous work done in our team, a uniaxial anisotropic dielectric material has been considered to achieve circular polarization and the orthogonal $\mathrm{TE}^x_{\delta 11}$ and $\mathrm{TE}^y_{1\delta 1}$ modes are used. The relative permittivity has been expressed by the following tensor $\varepsilon_r = [\varepsilon_x\ 0\ 0;\ 0\ \varepsilon_y\ 0\ ;\ 0\ 0\ \varepsilon_z]$, where $\varepsilon_x \neq \varepsilon_y = \varepsilon_z$ or $\varepsilon_y \neq \varepsilon_x = \varepsilon_z$ [16]. This method has been proven to be useful for tuning the fundamental modes in order to obtain CP at a single frequency band. Figure 3.3 shows the manufactured anisotropic DRA wtih CP as wel as its axial ratio (for more details, see [16]). Therefore, to have a dual-band CP DRA, besides the fundamental modes, a pair of orthogonal modes can be considered to achieve CP at the upper band.

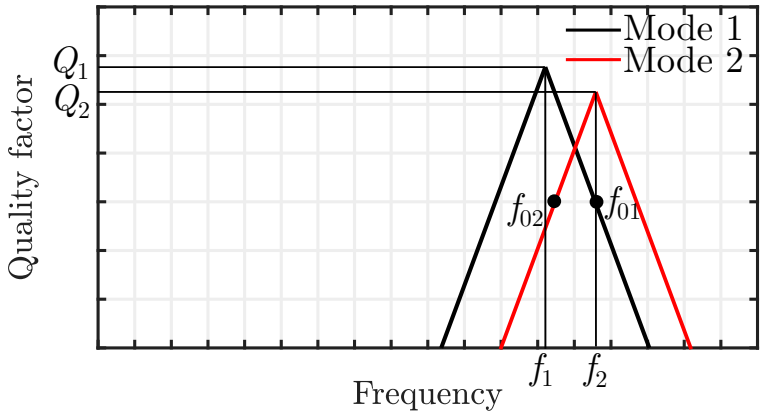

(a)

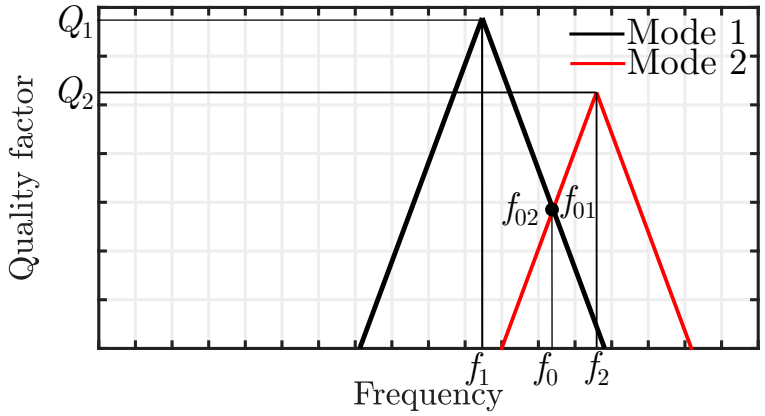

(b)

Figure 3.2: Curves of quality factor over frequency of two orthogonal modes in which the CP are (a) non-fulfilled and (b) fulfilled.

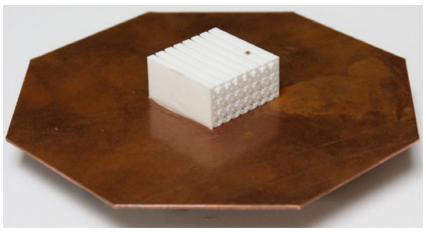

(a)

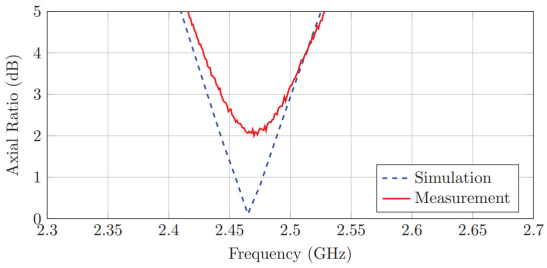

(b)

Figure 3.3: (a) Uniaxial anisotropic DRA with circular polarization and (b) its axial ratio [16].

When it comes to a dual-band operation, it is necessary to analyze the effects of the presence of a uniaxial dielectric for the higher-order modes as well as for the fundamental ones and whether it would be possible to achieve CP at both bands. To do so, besides the

fundamental modes $TE^x_{\delta 11}$ and $TE^y_{1\delta 1}$, the higher-order modes $TE^x_{\delta 13}$ and $TE^y_{1\delta 3}$ are used throughout this Chapter, since they present similar broadside radiation patterns and can be excited employing the same feeding method. Also, it is important to point out that, to have CP at two bands, each pair of orthogonal modes, namely ($TE^x_{\delta 11}$, $TE^y_{1\delta 1}$) and ($TE^x_{\delta 13}$, $TE^y_{1\delta 3}$), must satisfy Eq. 3.1 and 3.2 at once.

To investigate the influence of the use of a uniaxial dielectric to have a dual-band circularly-polarized DRA, the first step is to design a square-based DR using the Dielectric Waveguide Method (DWM) and the Eigenmode solution of Ansys HFSS. The center frequency of the L5 (1176.45 MHz ± 10.23 MHz) and L1 (1575.42 MHz ± 10.23 MHz) bands of the Global Positioning System (GPS) are taken as reference for the fundamental and higher-order modes, respectively. At first, considering an isotropic dielectric with $\varepsilon_r = 10$, the width w and height b of the DRA are defined as 50.5 mm and 61.0 mm, respectively. The resonance frequencies of the fundamental and higher-order modes are around 1.176 GHz and 1.575 GHz, respectively. Then, we assume a uniaxial anisotropic dielectric with:

$$\varepsilon_r = \begin{pmatrix} \varepsilon_x & 0 & 0 \\ 0 & \varepsilon_y & 0 \\ 0 & 0 & \varepsilon_z \end{pmatrix}, \tag{3.3}$$

and $\varepsilon_x = \varepsilon_z \neq \varepsilon_y$, and, thus, ε_y is varied and the resonance frequencies and Q-factors of the fundamental and higher-order modes are calculated using the Eigenmodes solution of Ansys HFSS, as can be seen in Fig. 3.4. One can note in Fig. 3.4(a) that the resonance frequencies of the $TE^y_{1\delta 1}$ and $TE^y_{1\delta 3}$ modes are almost constant for different values of ε_y. This result is expected since the electric field does not have a y-component for these two modes. However, the resonance frequencies decrease for the $TE^x_{\delta 11}$ and $TE^x_{\delta 13}$ modes when increasing ε_y. Also, it is possible to realize that the $TE^x_{\delta 13}$ mode is much more sensible than the $TE^x_{\delta 11}$ for variations of ε_y. From Fig. 3.4(b), the Q-factors of the higher-order modes are much higher than for the fundamental ones, as expected. Besides, the difference according to ε_y variation between the Q-factors of the fundamental modes is lower than for the higher-order modes.

With the resonance frequencies and Q-factors calculated for each mode at issue (Fig. 3.4), the parameters of Eq. 3.1 and 3.2 can be found. First, the resonance frequencies of each pair of orthogonal modes must be sorted into f_1 and f_2, where f_2 is always higher than f_1, which can be observed in Fig. 3.5(a). Q_1 and Q_2 are organized as well according to f_1 and f_2, as shown in Fig. 3.5(b). From these parameters, the frequencies f_{01} and f_{02} can be calculated using Eq. 3.1 and 3.2 as a function of ε_y, which are presented in Fig. 3.5(c). One can note that, for the higher-order modes, the curves of f_{01} and f_{02} intersect each other for $\varepsilon_y = 8.2$ and $\varepsilon_y = 11.9$, which means that the conditions for having CP are fulfilled for these two values of ε_y. On the other hand, for the fundamental modes, the curves of f_{01} and f_{02} do not intersect, which means that the CP conditions are not respected at the lower band whatever the value of ε_y. Therefore, with a homogeneneous uniaxial anisotropic dielectric resonator, it would not be possible to have CP at both bands at the same time, since f_{01} and f_{02} of the fundamental and higher-order modes do not intersect each other for the same value of ε_y.

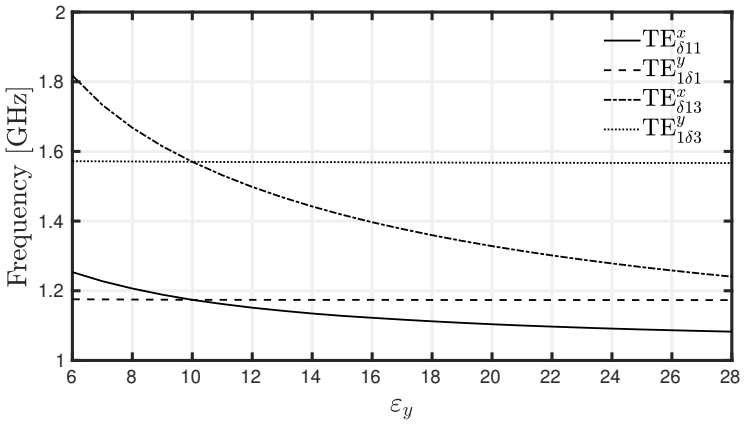

(a)

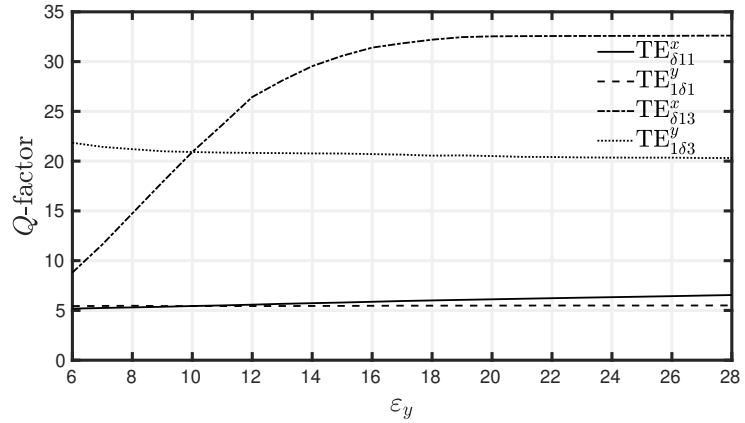

(b)

Figure 3.4: (a) Resonance frequencies and (b) Q-factors as a function of ε_y calculated using the Eigenmode solution of Ansys HFSS and considering a uniaxial anisotropic and homogeneous dielectric resonator.

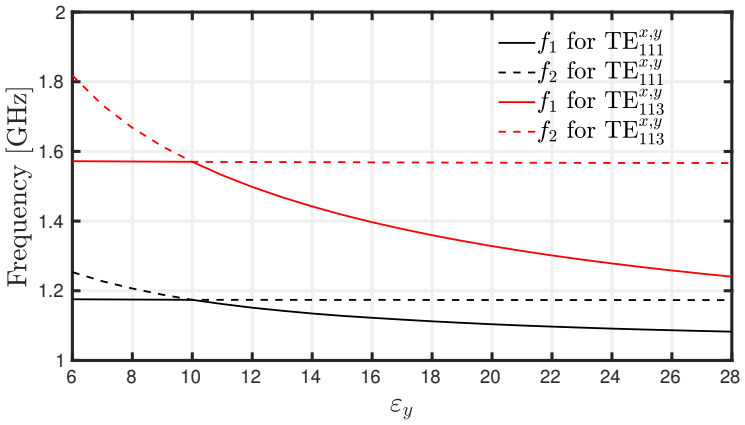

(a)

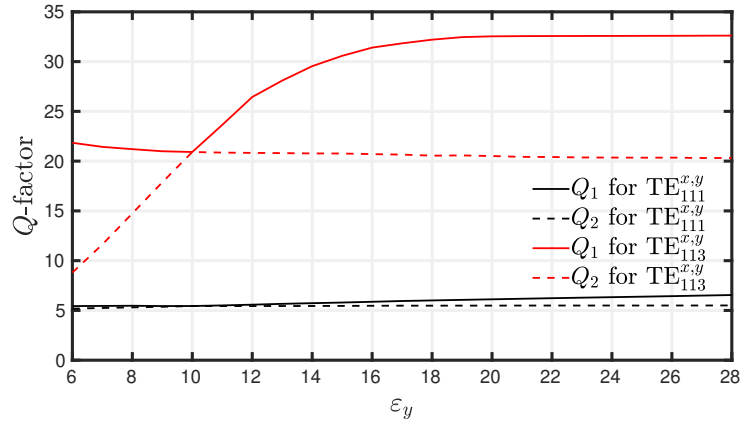

(b)

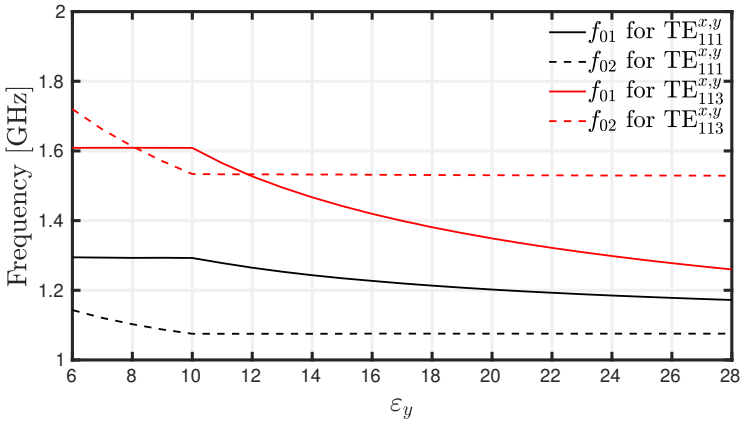

(c)

Figure 3.5: Curves of (a) f_1 and f_2, (b) Q_1 and Q_2 and (c) f_{01} and f_{02} of the $\mathrm{TE}_{\delta 11}^{x}$, $\mathrm{TE}_{1\delta 1}^{y}$, $\mathrm{TE}_{\delta 13}^{x}$ and $\mathrm{TE}_{1\delta 3}^{y}$ modes for different values of ε_y calculated for a homogeneous and uniaxial anisotropic dielectric resonator.

Instead of using a homogeneous and anisotropic dielectric resonator, one possible solution is to mix isotropic and anisotropic dielectric in a inhomogeneous material. Hence, it is necessary for our application to understand the electric field distribution of the modes at issue, as can be observed in Fig. 3.6, where a homogeneous and isotropic DR over an infinite PEC ground plane is considered. Looking to these figures, it is easier to understand what happened for the homogeneous and anisotropic case. Indeed, one can realize the reason why the $\mathrm{TE}^{x}_{\delta 13}$ mode is more sensible than the $\mathrm{TE}^{x}_{\delta 11}$ as ε_y changes, because the y-directed electric fields of the $\mathrm{TE}^{x}_{\delta 13}$ mode are stronger than the $\mathrm{TE}^{x}_{\delta 11}$. Thus, to have a dual-band and CP operation, more degrees of freedom must be found to design the antenna to control the CP at the lower and upper bands independently. To do so, it is possible to observe that, at the faces of DR parallel to the xz-plane, the z-directed electric field of the $\mathrm{TE}^{x}_{\delta 11}$ mode is stronger and more concentrated than for the $\mathrm{TE}^{x}_{\delta 13}$, especially at the lower region, for instance. So, if the electric permittivity were locally changed around this area, it would be possible to find variables to control the fundamental and higher-order modes more independently and, then, respect the CP conditions at both bands at the same time. Taking this information into account, the design shown in Fig. 3.7 is proposed, which presents an inhomogeneous dielectric resonator, with an isotropic permittivity region represented by ε_{ri}, and an anisotropic one, in which its relative permittivity ε_{ra} is described by the following tensor:

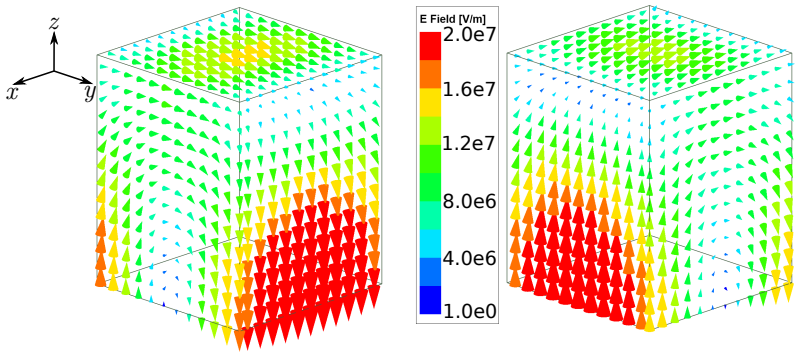

(a) $\mathrm{TE}^{x}_{\delta 11}$ (b) $\mathrm{TE}^{y}_{1\delta 1}$

(c) $\mathrm{TE}^{x}_{\delta 13}$ (d) $\mathrm{TE}^{y}_{1\delta 3}$

Figure 3.6: Electric field distribution of the fundamental ((a) $\mathrm{TE}^{x}_{\delta 11}$ and (b) $\mathrm{TE}^{y}_{1\delta 1}$) and higher ((c) $\mathrm{TE}^{x}_{\delta 13}$ and (d) $\mathrm{TE}^{y}_{1\delta 3}$) modes for a homogeneous and isotropic DR over an infinite PEC ground plane.

$$\varepsilon_{ra} = \begin{pmatrix} \varepsilon_x & 0 & 0 \\ 0 & \varepsilon_y & 0 \\ 0 & 0 & \varepsilon_z \end{pmatrix}, \tag{3.4}$$

where $\varepsilon_{ri} = \varepsilon_x = \varepsilon_y \neq \varepsilon_z$.

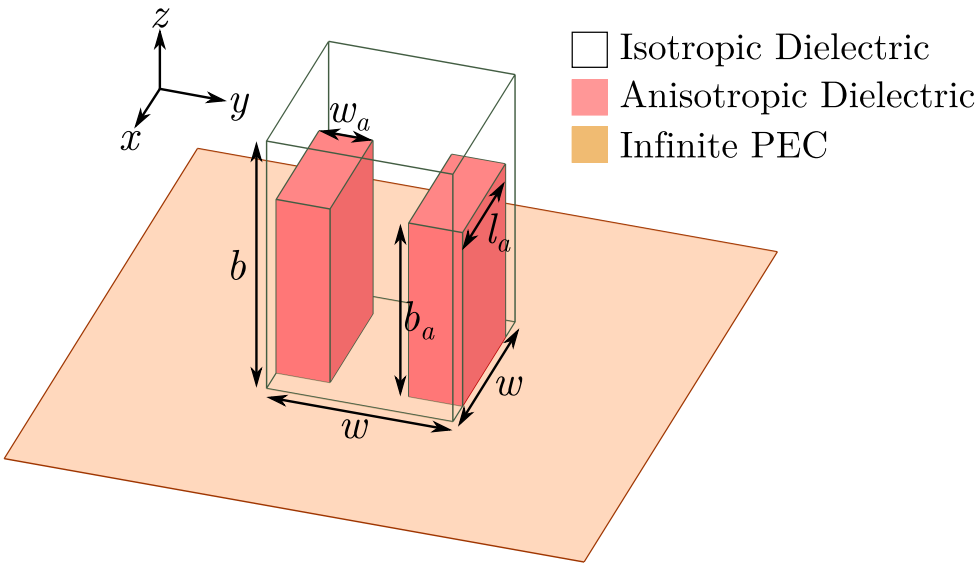

Figure 3.7: Perspective view of the proposed inhomogeneous DR over an infinite ground plane.

To verify the possibility of having CP at both L5 and L1 bands, Eq. 3.1 and 3.2 must be calculated but, first, it is necessary to optimize the parameters of the antenna. Thus, the electric field distributions of the modes at issue are analyzed to do so. As the Q-factors of the fundamental modes are much lower than the higher-order ones, the CP at the lower band is adjusted first, which is done by controlling l_a. Indeed, the electric field distribution of the $\text{TE}^x_{\delta 11}$ is stronger and more distributed than the $\text{TE}^x_{\delta 13}$ along the length of the anisotropic region, and ε_z is optimized since the z-componenent of the electric of the $\text{TE}^x_{\delta 11}$ are stronger at the anisotropic region. Secondly, the CP at the upper band is controlled by varying b_a, since the electric field of the $\text{TE}^x_{\delta 13}$ is more concentrated in the upper part of the anisotropic region than the fundamental mode. Last, the width w_a of the anisotropic region is optimized. Taking all these information into account and using the Eigenmode solution of Ansys HFSS, the parameters of the antenna can be optimized and the resonance frequencies and Q-factors are, for instance, shown as a function of ε_z in Fig. 3.8, where $\varepsilon_{ri} = \varepsilon_x = \varepsilon_y = 10$, $b = 75.0$ mm, $w = 41.5$ mm, $b_a = 42.0$ mm, $l_a = 29.0$ mm, and $w_a = 10.5$ mm. As expected, the resonance frequencies of the fundamental modes are more sensitive than the higher-order ones to the variation of ε_z, as can be observed in Fig. 3.8(a). From Fig. 3.8(b), one can note

that the Q-factors are directly proportional to ε_z and, as expected, they are higher for the higher-order modes. From this analysis, the resonance frequencies found on Ansys HFSS can be sorted into f_1 and f_2, as presented in Fig. 3.9(a), as well as the Q-factors into Q_1 and Q_2, as can be seen in Fig. 3.9(b), so that f_{01} and f_{02} can be calculated using Eq. 3.1 and 3.2, as shown in Fig. 3.9(c). It is possible to note that f_{01} and f_{02} intersect each other for both pairs of orthogonal modes for $\varepsilon_z = 25.1$ and, then, the CP conditions are fulfilled at both bands at the same time, showing the possibility of having a dual-band circularly-polarized DRA.

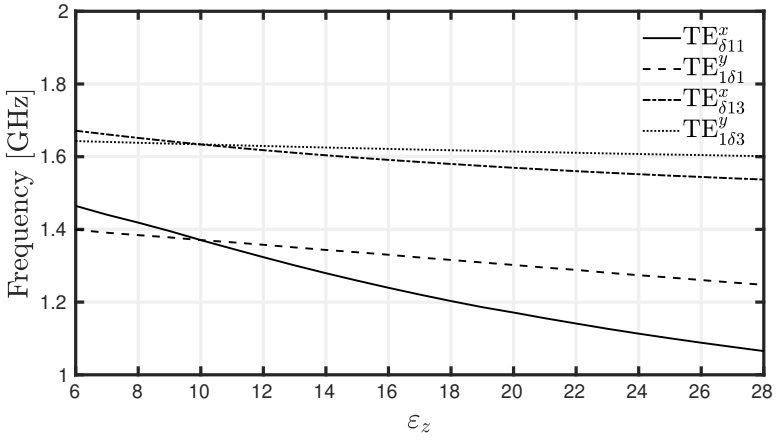

(a)

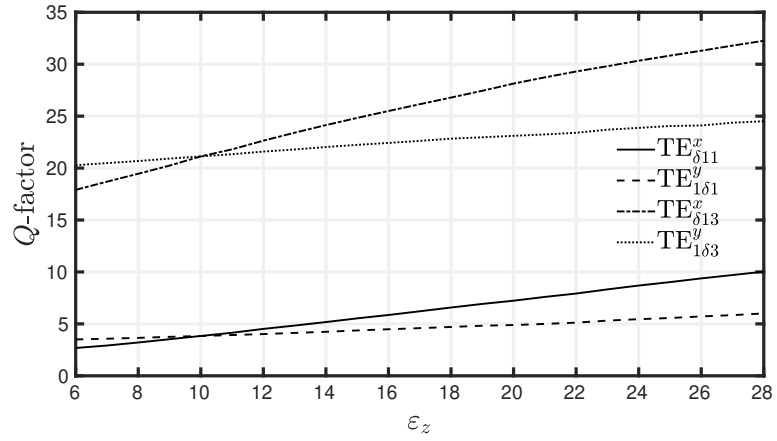

(b)

Figure 3.8: Curves of (a) resonance frequencies and (b) Q-factors calculated using the Eigenmode solution of Ansys HFSS considering the proposed inhomogeneous and anisotropic dielectric resonator with $\varepsilon_{ri} = \varepsilon_x = \varepsilon_y = 10$, $b = 75.0$ mm, $w = 41.5$ mm, $b_a = 42.0$ mm, $l_a = 29.0$ mm, and $w_a = 10.5$ mm.

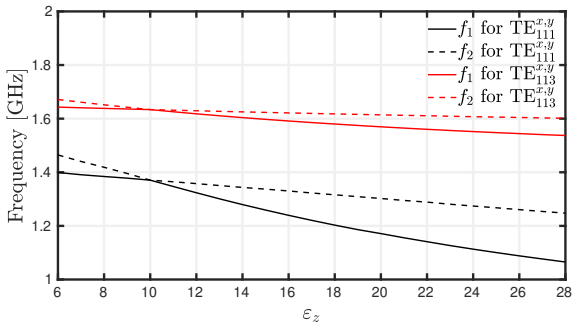

(a)

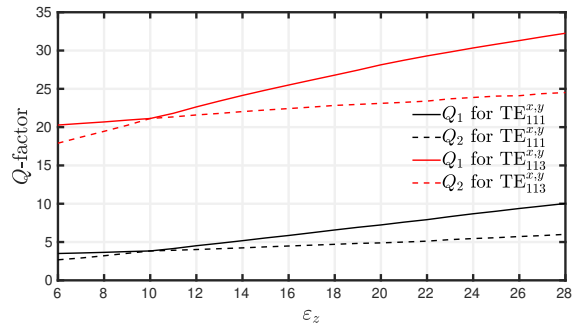

(b)

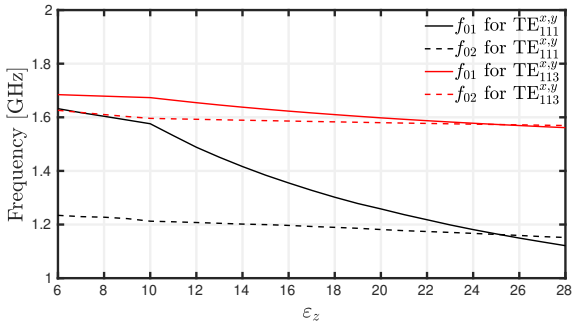

(c)

Figure 3.9: Curves of (a) resonance frequencies, (b) Q-factors, and (c) f_{01} and f_{02} of the $\mathrm{TE}_{\delta 11}^{x}$, $\mathrm{TE}_{1\delta 1}^{y}$, $\mathrm{TE}_{\delta 13}^{x}$, and $\mathrm{TE}_{1\delta 3}^{y}$ modes for different values of ε_z considering the proposed inhomogeneous and anisotropic DR with $\varepsilon_{ri} = \varepsilon_x = \varepsilon_y = 10$, $b = 75.0$ mm, $w = 41.5$ mm, $b_a = 42.0$ mm, $l_a = 29.0$ mm, and $w_a = 10.5$ mm.

To better understand the proposed DRA and their new variables, the curves of f_{01} and f_{02} are plotted as a function of the anisotropic region dimensions, namely b_a, l_a, and w_a, as can observed in Fig. 3.10. These results have been calculated using the Eigenmode analysis with $w = 41.5$ mm, $b = 75$ mm, $w_a = 10.5$ mm, $b_a = 42$ mm, $l_a = 29$ mm, $\varepsilon_{ri} = \varepsilon_x = \varepsilon_y = 10$, and $\varepsilon_z = 25.1$. In Fig. 3.10(a), one can note that the variable b_a has more influence on the CP for the higher-order modes than for the fundamental ones, since the curves for $\mathrm{TE}_{\delta 13}^{x}$

and $\mathrm{TE}^{y}_{1\delta 3}$ modes diverge more from each other as b_a varies. It agrees with their electric-field distributions since the z-components of the electric field of the $\mathrm{TE}^{x}_{\delta 13}$ mode are more concentrated at the upper part of the anisotropic region, as can be verified in Fig. 3.6. On the other hand, l_a affects more the CP of the fundamental modes since the z-components of the electric field of the $\mathrm{TE}^{x}_{\delta 11}$ mode are more distributed along the x-direction than the $\mathrm{TE}^{x}_{\delta 13}$. Finally, f_{01} and f_{02} of the fundamental modes are more sensitive than the higher-order ones for values w_a up to 9 mm, however, their behaviors are similar from around 9 mm to 18 mm, as can be observed in Fig. 3.10(c).

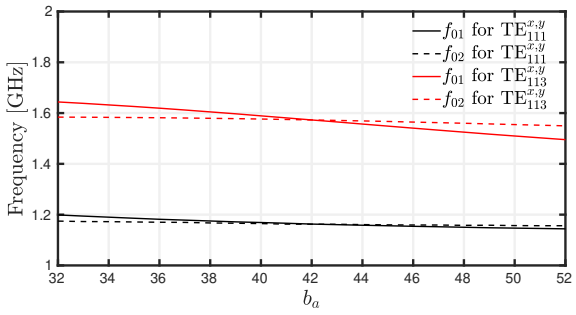

(a)

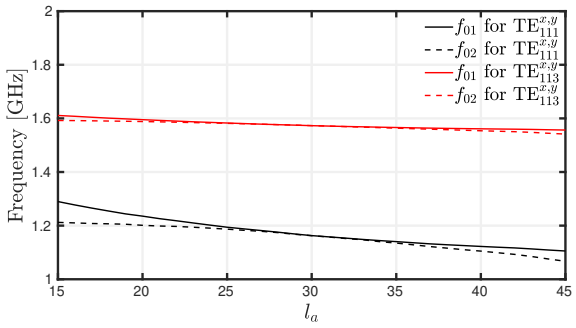

(b)

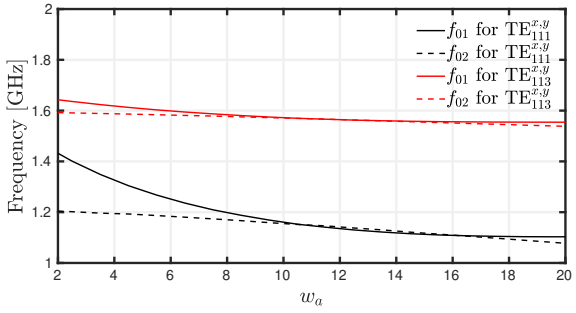

(c)

Figure 3.10: Curves of f_{01} and f_{02} of the $\mathrm{TE}^{x}_{\delta 11}$, $\mathrm{TE}^{y}_{1\delta 1}$, $\mathrm{TE}^{x}_{\delta 13}$, and $\mathrm{TE}^{y}_{1\delta 3}$ modes for different values of (a) b_a, (b) l_a, and (c) w_a, considering the proposed inhomogeneous and anisotropic DR with $\varepsilon_{ri} = \varepsilon_x = \varepsilon_y = 10$, $\varepsilon_z = 25.1$, $b = 75.0$ mm, $w = 41.5$ mm, $b_a = 42.0$ mm, $l_a = 29.0$ mm, and $w_a = 10.5$ mm.

3.2 Antenna Design and Results

In Section 3.1, the analyses were conducted considering a DR with an infinite ground plane without any feeding. In this section, a simple feeding scheme is implemented. As one of the goals of this work is to propose a dual-band DRA with CP due to the material by itself, a simple slot coupled to a microstrip line is considered rather than complex feeding methods or parasitic elements, as can be observed in Fig. 3.11. One can note that this slot, with width w_s and length l_s, is placed along the diagonal of the DR to excite the $\mathrm{TE}^{x}_{\delta 11}$, $\mathrm{TE}^{y}_{1\delta 1}$, $\mathrm{TE}^{x}_{\delta 13}$, and $\mathrm{TE}^{y}_{1\delta 3}$ modes at once with the same amplitude. Moreover, the slot is coupled to a 50-Ω microstrip transmission line with width w_l and length l_l, which are printed on an RF-301 Taconic ($\varepsilon_r = 2.97$ and $\tan\delta = 0.0012$) substrate with thickness h_s equal to 1.524 mm and a finite hexagonal-shaped ground plane is considered. To control the impedance matching at both bands, the dimensions of the slot and the stub length, *i.e.* the distance from the end of the microstrip line to the slot, are optimized. Also, the microstrip transmission line and the ground plane are made out of copper.

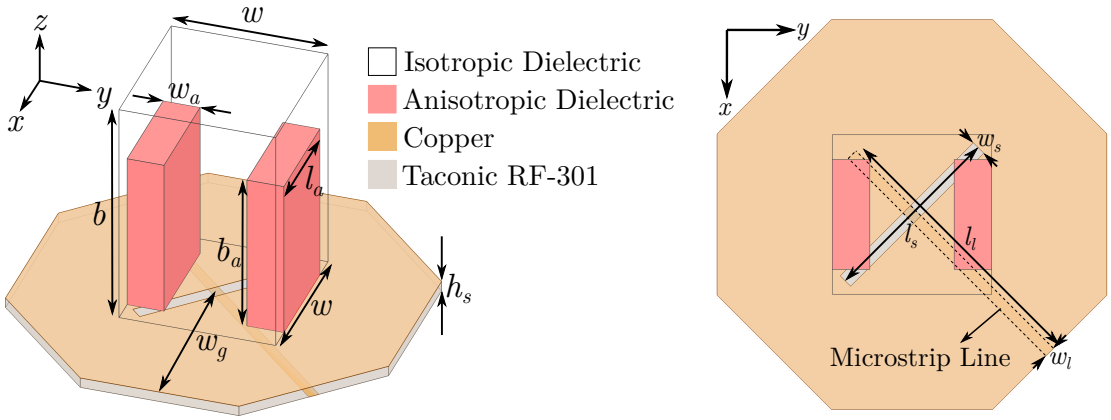

Figure 3.11: (a) Perspective and (b) top views of the proposed inhomogeneous and anisotropic DRA.

The dimensions of the DR optimized with the Eigenmode solution are considered as a starting point and this first design is referred to as *Initial model*. At first, the magnitude of the reflection coefficient $|S_{11}|$, in dB, for this model is computed using a full-wave simulation on Ansys HFSS of the DRA with a finite ground plane with radius w_g equal to 135 mm, as shown in Fig. 3.12(a). One can note that the antenna is well-matched at both L5 and L1 bands. Figure 3.12(b) presents the axial ratio (AR) at the boresight direction ($\theta = 0°$ and $\phi = 0°$). It is possible to realize that the CP is achieved only at the lower band, since the AR is below 3 dB, while, at the upper band, the AR is a little bit above 3 dB. This result is expected since the Eigenmode analysis does not consider a feeding and the finite ground plane. Then, it is necessary to optimize the DRA considering these elements.

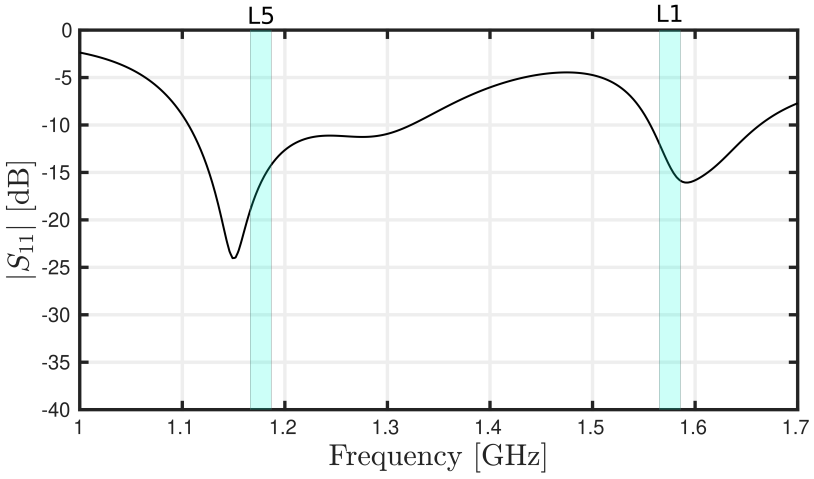

(a)

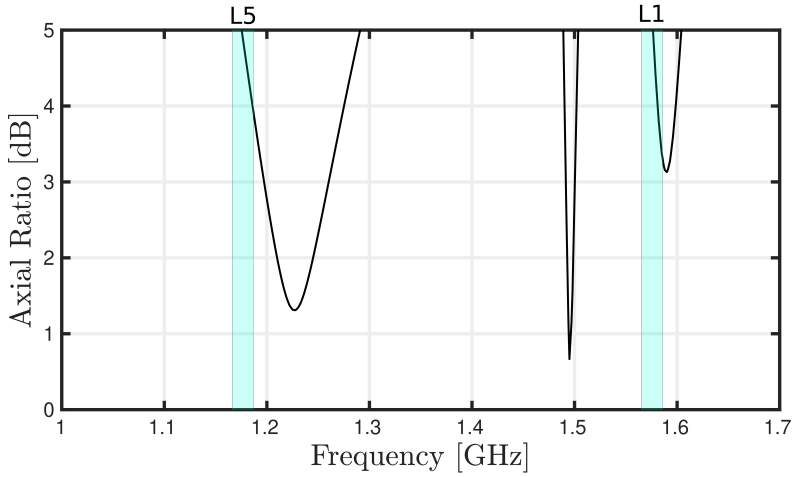

(b)

Figure 3.12: Simulated (a) reflection coefficient and (b) axial ratio of the initial model of the proposed DRA.

To find the ideal dimensions of the DRA, the parametric analysis performed in Section 3.1 is taken into account as well as the field distribution of the modes at issue. After an optimization, the new parameters are $w = 45$ mm, $b = 67$ mm, $w_a = 10.5$ mm, $l_a = 31$ mm, $b_a = 47$ mm, $w_g = 135$ mm, $h_s = 1.524$ mm, $\varepsilon_{ri} = \varepsilon_x = \varepsilon_y = 10$, and $\varepsilon_z = 22.2$, in which this design will be referred to as *Solid model*. Considering these parameters, Fig. 3.13(a) shows the magnitude of the reflection coefficient $|S_{11}|$ in dB. The simulated impedance bandwidths ($|S_{11}| < 10$ dB) of solid model are 17.96% (1065.0 MHz - 1275.1 MHz) and 10.62% (1513.8 MHz - 1668.4 MHz) covering both L5 and L1 bands, respectively. Moreover, Fig. 3.13(b) presents the axial ratio of the solid model at the boresight direction ($\phi = 0°$ and $\theta = 0°$). It is possible to note that now the minimums of AR are located at the center of the L5 and L1 bands and below 3 dB. Also, the simulated 3-dB AR bandwidths are 5.00% (1140.3 MHz - 1198.8 MHz) and 1.46% (1562.8 MHz - 1585.7 MHz), covering both L5 and L1 bands.

In addition, regarding the slot and microstrip line, for both initial and solid models, their dimensions are $w_s = 4.16$ mm, $l_s = 57.4$ mm, $w_l = 3.86$ mm, and $l_l = 163.9$ mm, and the stub length is 28.9 mm. For the sake of comparison, Table 3.1 shows the dimensions and properties of both models.

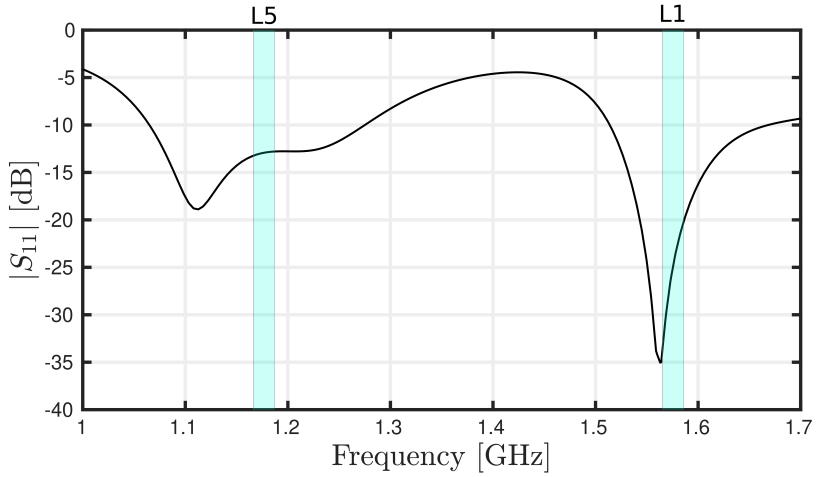

(a)

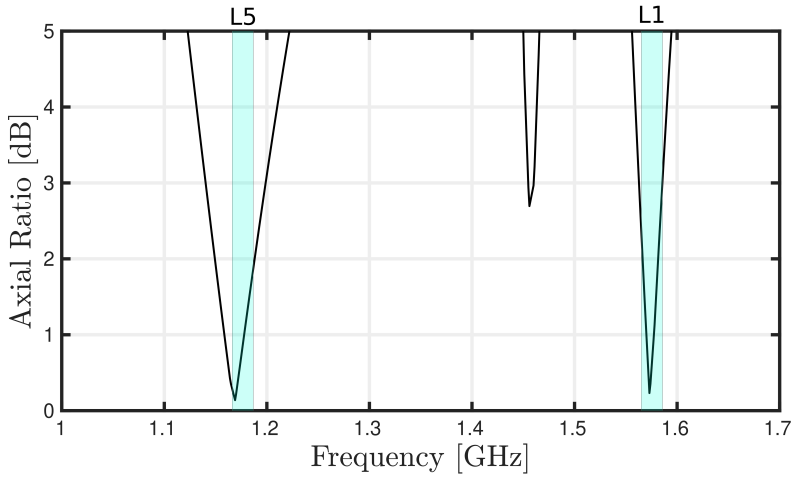

(b)

Figure 3.13: Simulated (a) reflection coefficient and (b) axial ratio of the optimized solid model of the proposed DRA.

Model	w	b	w_a	b_a	l_a	w_g	ε_r	ε_x	ε_y	ε_z
Initial	41.5 mm	75 mm	10.5 mm	42 mm	29 mm	135 mm	10	10	10	25.1
Solid	45 mm	67 mm	11.5 mm	47 mm	31 mm	135 mm	10	10	10	22.2

Table 3.1: Parameters of the initial and solid models of the proposed DRA.

The left- and right-handed components of the gain pattern, in dBi, at the L5 and L1 bands, *i.e.* calculated at the frequency of minimum axial ratio within the frequency bands at issue, are shown in Fig. 3.14. It is possible to observe that the proposed antenna presents broadside radiation patterns at both bands and cut planes, as expected for the $\mathrm{TE}^{x}_{\delta 11}$, $\mathrm{TE}^{y}_{1\delta 1}$, $\mathrm{TE}^{x}_{\delta 13}$ and $\mathrm{TE}^{y}_{1\delta 3}$ modes. Moreover, the simulated peak gains at 1.17 GHz and 1.57 GHz are 6.50 dBi and 5.38 dBi, respectively.

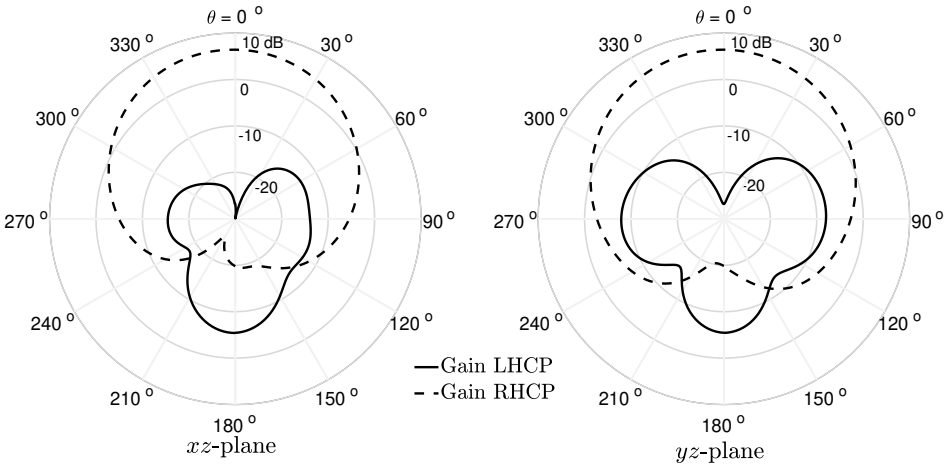

(a) $f = 1.17$ GHz

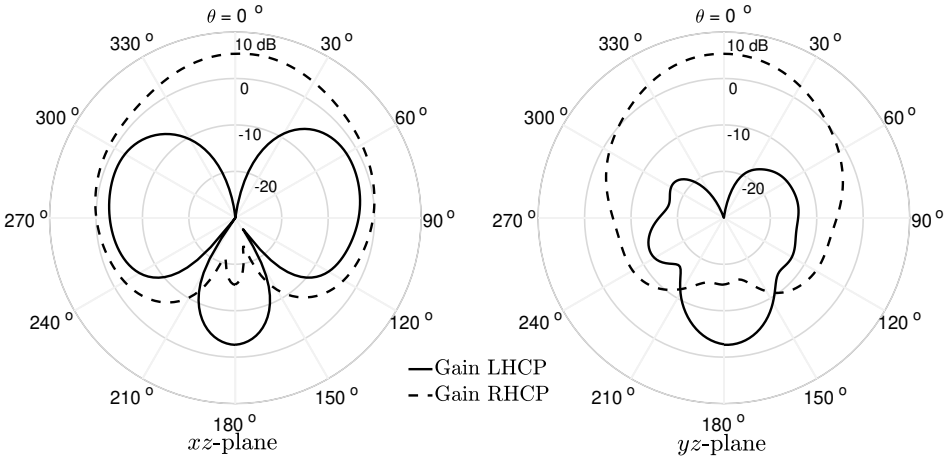

(b) $f = 1.57$ GHz

Figure 3.14: Simulated radiation patterns at (a) L5 and (b) L1 bands of the solid model of the proposed DRA.

Figure 3.15 shows the realized gain in dBi of the proposed dual-band circularly-polarized DRA at the boresight direction, *i.e.* for $\phi = 0°$ and $\theta = 0°$. With reference to the figure, the simulated realized gain at the center frequency of the L5 band is 6.23 dBi. At center of the L1 band, the realized gain is 6.6 dBi at the boresight direction.

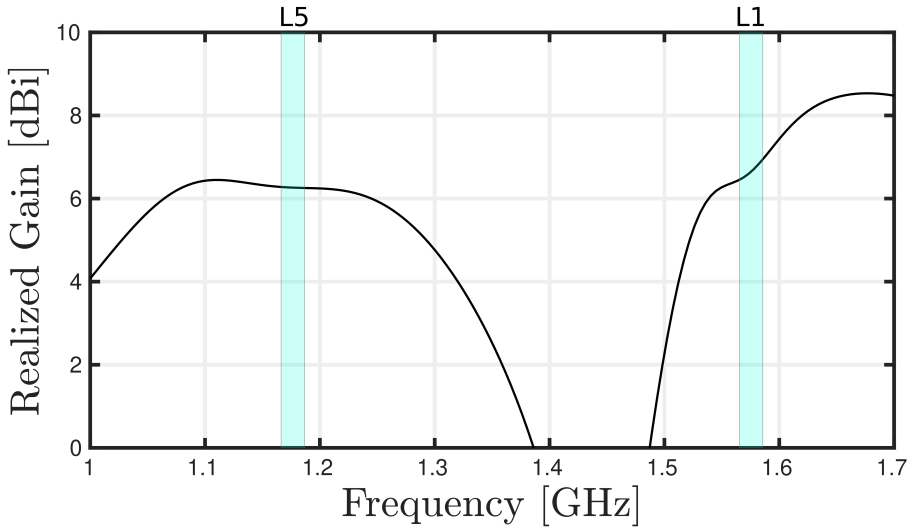

Figure 3.15: Simulated realized gain of the proposed dual-band circularly-polarized DRA at the boresight direction ($\phi = 0°$ and $\theta = 0°$).

One can observe also in Fig. 3.13(b) that the 3-dB AR bandwidth is narrower at the upper band than at the lower one and, to better understand it, the magnitude and phase of the ϕ- and θ-components of the electric field of the solid DRA are shown in Fig. 3.16. To obtain perfect CP and dual-band, each pair of orthogonal components of the electric field, *i.e.* E_ϕ and E_θ, must have the same amplitude and be in phase quadrature at each frequency band. As can be noted in Fig. 3.13(b), the minimum values of the AR are at 1.169 GHz and 1.573 GHz, where, in Fig. 3.16, the magnitude of the E_ϕ and E_θ are the same and the phase difference is approximately 270° and 90° at the lower and upper bands, respectively. Considering the magnitude of the electric fields, one can realize that their curves are steeper at the upper band than at the lower one, which means that the difference between $|E_\phi|$ and $|E_\theta|$ increases in a faster rate when the frequency slightly deviates from 1.573 GHz than from 1.169 GHz. So, this is the reason why the 3-dB AR bandwidth is broader at the L5 band than at the L1 band, but both bands are broad enough to cover both the L5 and L1 bands. This discussion is completed in Section 3.4, where we demonstrate the link with the Q-factors of these modes.

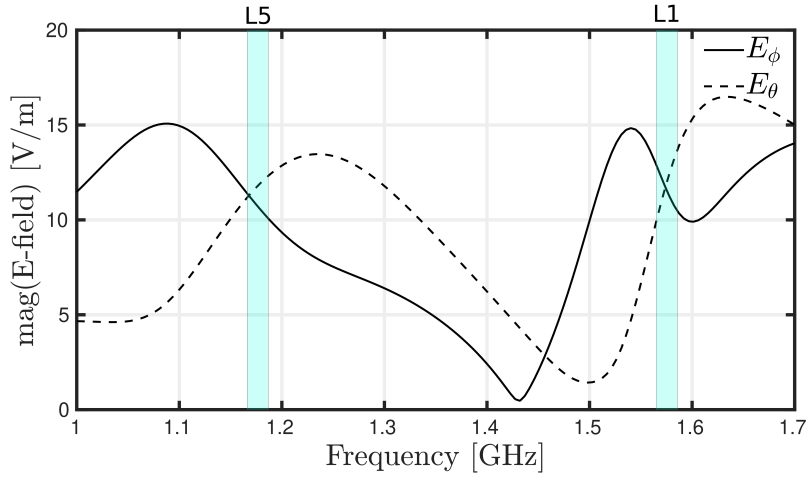

(a)

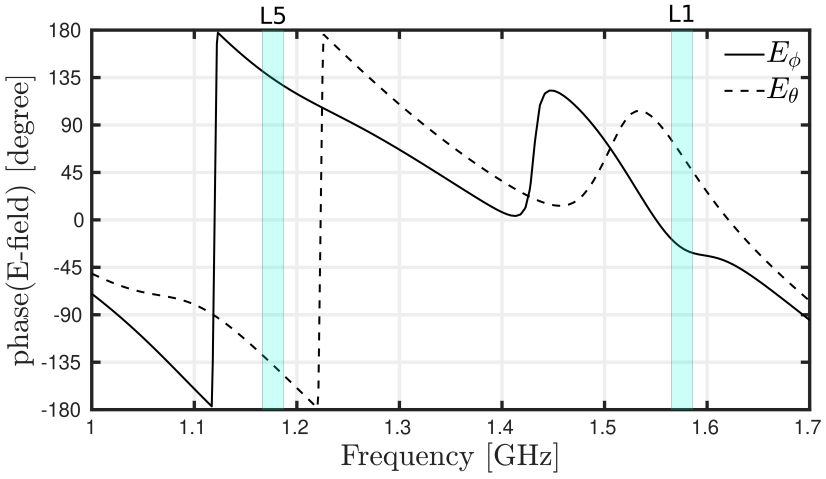

(b)

Figure 3.16: Simulated (a) magnitude and (b) phase of the ϕ- and θ-components of the electric field of the proposed dual-band circularly-polarized DRA at the boresight direction ($\phi = 0°$ and $\theta = 0°$).

Figure 3.17 presents the simulated axial ratio as a function θ at $\phi = 0°$ and $\phi = 90°$ calculated at 1.17 GHz and 1.57 Ghz, which are the frequencies of minimum axial ratio at the boresight direction ($\theta = 0°$ and $\phi = 0°$). At the lower band, the axial ratio is below 3 dB for $-44.84° \leq \theta \leq 46.96°$ and $-44.26° \leq \theta \leq 40.40°$ at $\phi = 0°$ and $\phi = 90°$, respectively. By contrast, at the upper band, the axial ratio is below 3 dB for $-20.67° \leq \theta \leq 22.10°$ and $-33.19° \leq \theta \leq 29.46°$ at $\phi = 0°$ and $\phi = 90°$, respectively.

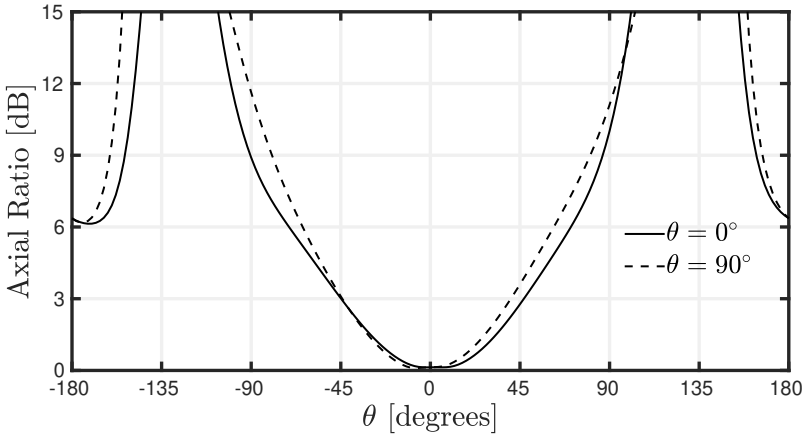

(a) 1.17 GHz

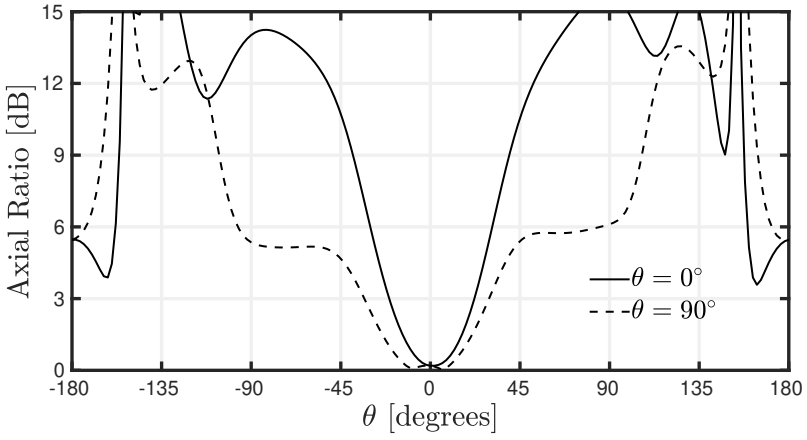

(b) 1.57 GHz

Figure 3.17: Simulated axial ratio as function of θ at the (a) L5 and (b) L1 bands of the proposed dual-band circularly-polarized DRA.

The simulated radiation efficiency of the proposed DRA is shown in Fig. 3.18. One can note that the efficiency is higher than 97 % from 1.0 to 1.7 GHz. In addition, considering the impedance bandwidth ($|S_{11}| < 10$ dB), *i.e.* from 1065.0 MHz to 1275.1 MHz and from 1513.8 MHz to 1668.4 MHz, the simulated efficiency is higher than 99 %. These results are good and highlight one of the main advantages of DRA over patch antennas which is due to the absence of conductor and surface-wave losses in DRA.

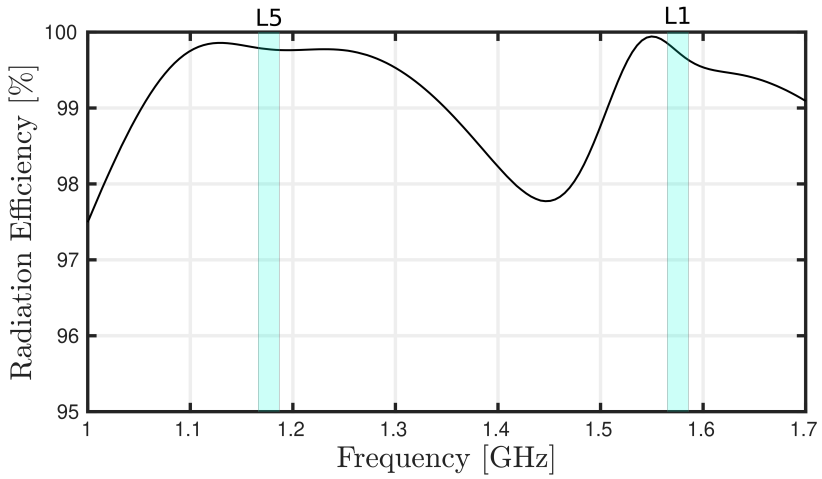

Figure 3.18: Simulated radiation efficiency of the proposed DRA.

3.3 Parametric Analysis

In Section 3.1, the influence of the new parameters of the DR has been investigated. However, this analysis was made considering an infinite ground plane without any feeding source and using the Eigenmode solution of Ansys HFSS where the theoretical frequencies of minimum axial ratio were computed. Therefore, in this Section, a similar study is carried but considering a finite ground plane and the feeding, and using the Driven Terminal solution of Ansys HFSS. Also, the reflection coefficient S_{11} and axial ratio are calculated as a function of b_a, l_a, w_a, w_g, and ε_z, where the parameters of the DRA are $w = 45$ mm, $b = 67$ mm, $w_a = 10.5$ mm, $l_a = 31$ mm, $b_a = 47$ mm, $w_g = 135$ mm, $h_s = 1.524$ mm, $w_s = 4.16$ mm, $l_s = 57.4$ mm, $w_l = 3.86$ mm, $l_l = 163.9$ mm, $\varepsilon_{ri} = \varepsilon_x = \varepsilon_y = 10$, and $\varepsilon_z = 22.2$.

The influence of the height b_a of the anisotropic region in the reflection coefficient and axial ratio is shown in Fig. 3.19. One can realize that both impedance bandwidth and AR are more sensitive at the upper band than at the lower one when b_a deviates from its optimal value of 47 mm. These results are following the electric field distribution of the modes at issue (see Fig. 3.6), since the z-component of the electric field of the higher-order modes around the anisotropic regions is more concentrated at the upper part of the DRA when compared to the fundamental modes. It agrees as well with the curves of f_{01} and f_{02} from the Eigenmode analysis, as it was observed in Fig. 3.10(a).

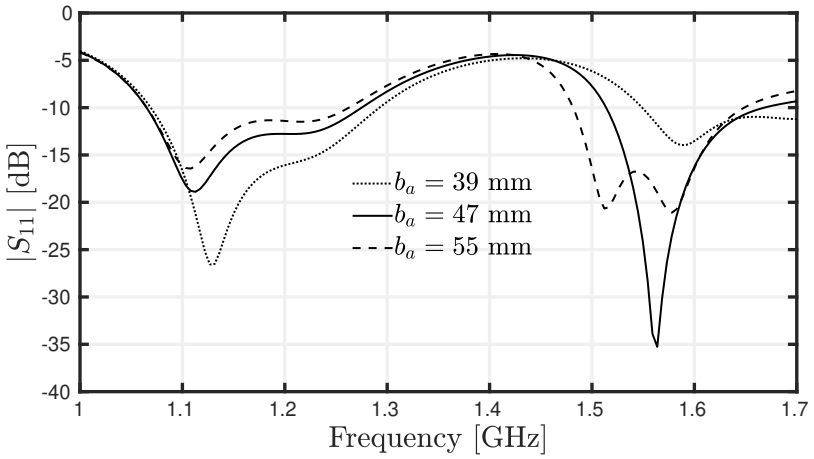

(a)

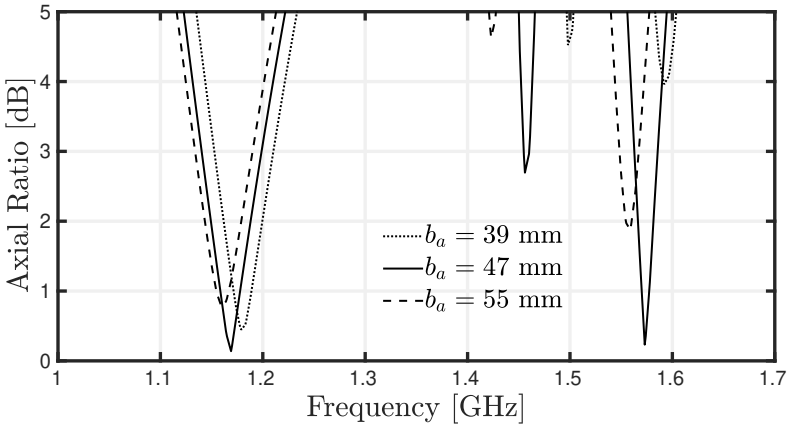

(b)

Figure 3.19: Simulated (a) reflection coefficient and (b) axial ratio for different values of height of b_a of the uniaxial anisotropic dielectric region.

Figure 3.20 presents the $|S_{11}|$ and AR as a function of the length l_a of the anisotropic regions. It is possible to note that variations of l_a result in a bigger relative frequency shift at the L5 band than at the L1 band, which can be better visualized in the AR curves. This conclusion agrees with the electric field distribution of the mode at issue since the electric field of the $\mathrm{TE}^x_{\delta 11}$ mode in the anisotropic region is more distributed along the x-direction in comparison to the $\mathrm{TE}^x_{\delta 13}$ mode. Also, the same behavior can be observed from the curves of f_{01} and f_{02} in Fig. 3.10(b).

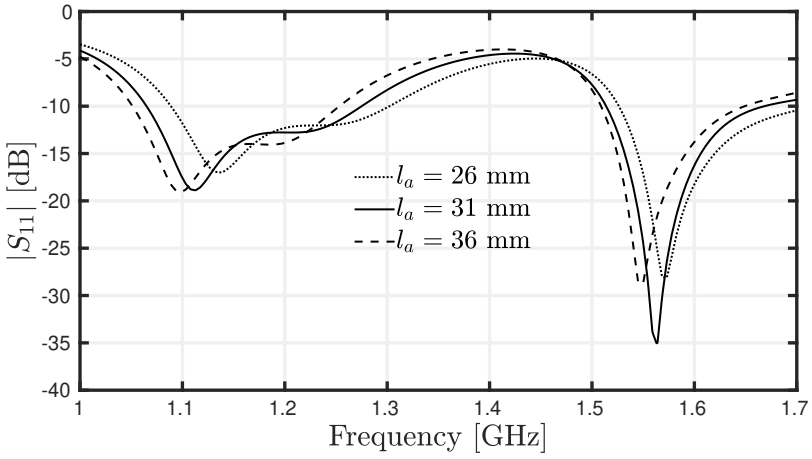

(a)

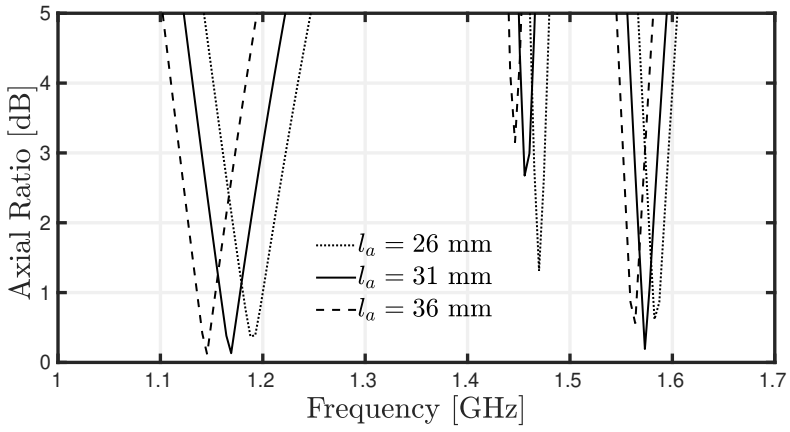

(b)

Figure 3.20: Simulated (a) reflection coefficient and (b) axial ratio for different values of the length l_a of the uniaxial anisotropic dielectric region.

In Fig. 3.21 the effect of w_a on the antenna is investigated. It is possible to note that this parameter has virtually the same effect on both bands, which is in agreement with the Eigenmode analysis from Fig. 3.10(a). The 3-dB AR bandwidths shift downwards as w_a increases at the L5 and L1 bands.

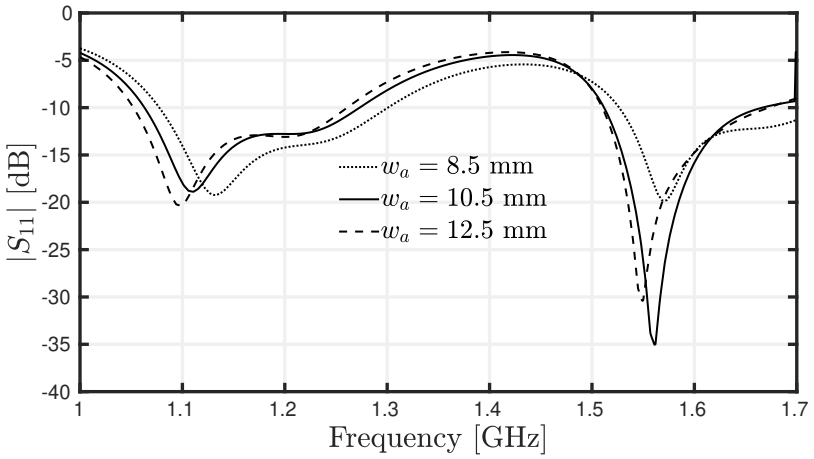

(a)

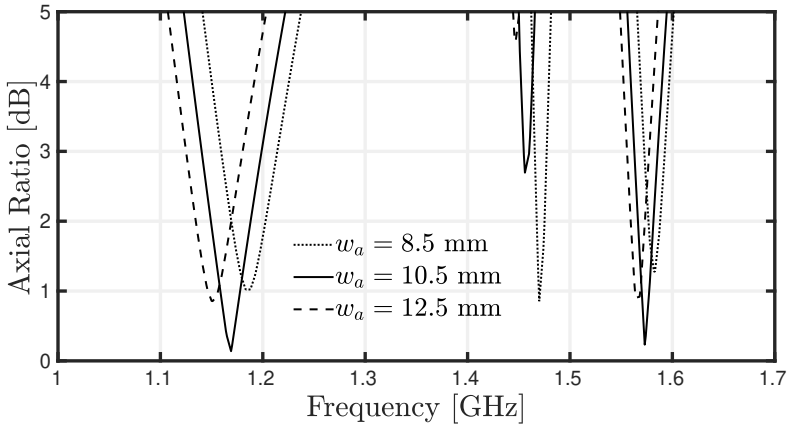

(b)

Figure 3.21: Simulated (a) reflection coefficient and (b) axial ratio for different values of width w_a of the uniaxial anisotropic dielectric region.

The effect of the z-component of the tensor of permittivity of the uniaxial dielectric ε_z is presented as well in Fig. 3.22. The level of axial ratio is more sensitive to variations of ε_z at both bands than for the other parameters, as expected, since a variation of ε_z means a change in the relative permittivity of the whole volume of the anisotropic regions.

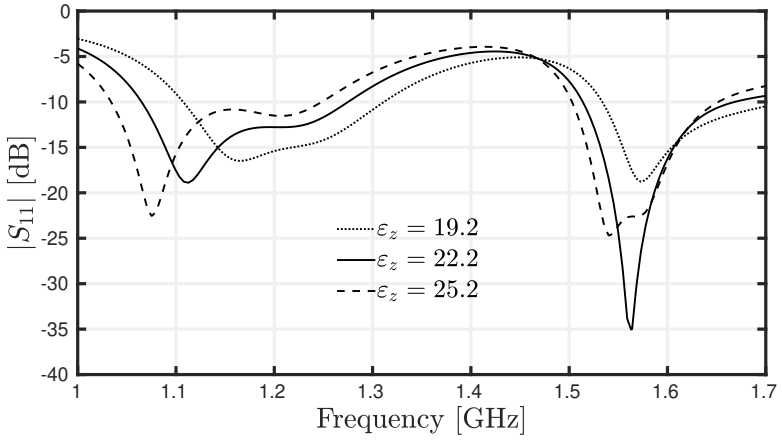

(a)

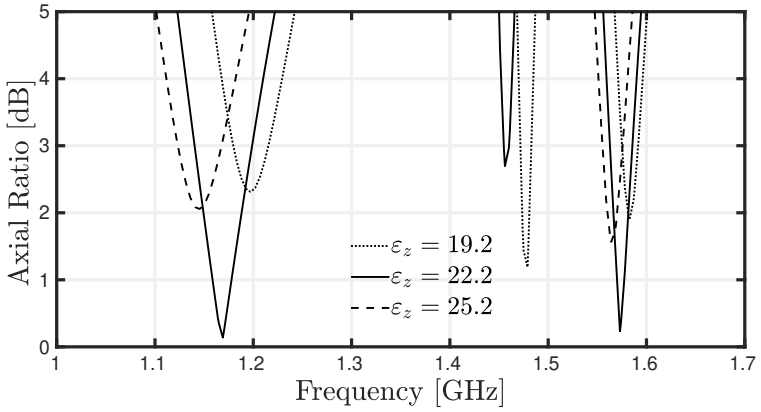

(b)

Figure 3.22: Simulated (a) reflection coefficient and (b) axial ratio for different values of ε_z of the uniaxial anisotropic dielectric region.

The $|S_{11}|$ and AR of the proposed DRA are calculated as well considering different sizes of ground plane, as can be observed in Fig. 3.23. It is important to point out that the stub length is the same for all different values of w_g and, thus, one can note that there are no relevant frequency shifts in the $|S_{11}|$ as w_g varies. When it comes to the axial ratio, the ground plane plays an important role, as can be seen in Fig. 3.23(b). As the size of the ground plane is getting smaller than one half of the wavelength, *i.e.* $2 \cdot w_g = \lambda_{\mathrm{L5}}/2 = 95$ mm and $2 \cdot w_g = \lambda_{\mathrm{L1}}/2 = 128$ mm, the axial ratio is getting worse. Therefore, for optimal performance in terms of AR, it is necessary to choose sizes of ground plane higher than $\lambda/2$, namely $2 \cdot w_g = 128$ mm in our case.

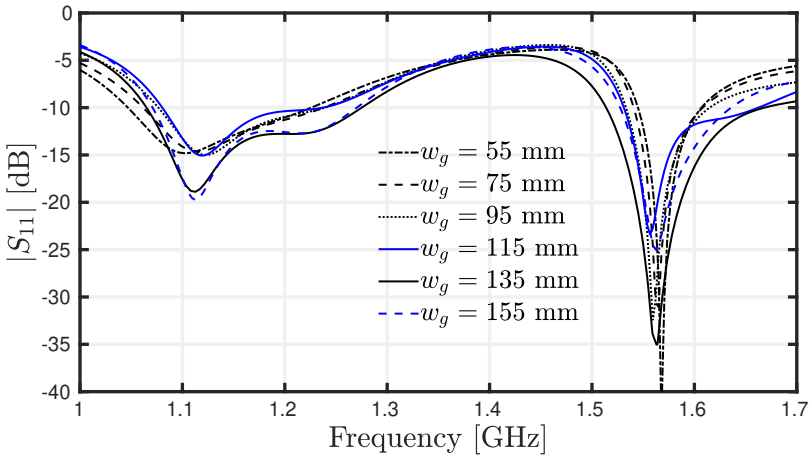

(a)

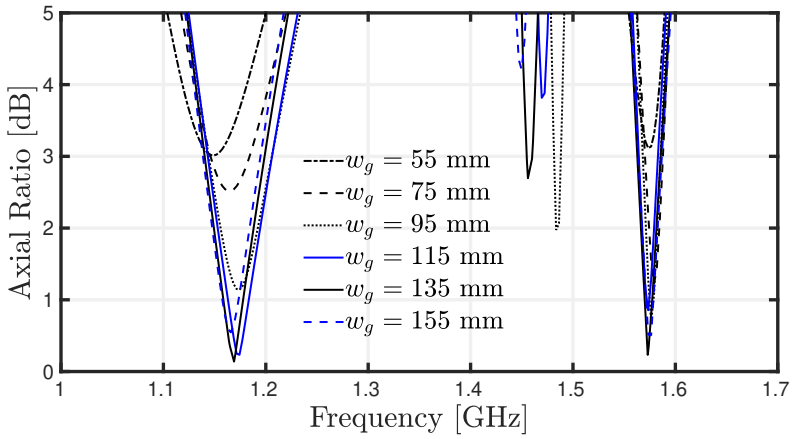

(b)

Figure 3.23: Simulated (a) reflection coefficient and (b) axial ratio for different values of w_g.

From the parametric study, a design guideline of the proposed DRA can be devised as follows. First, the width w and height b of the DRA are computed using the DWM so that the TE_{111} and TE_{113} modes resonate at frequencies a little bit higher than the L5 and L1 bands, respectively. Then, to excite properly these modes, the width and length of the slot and microstrip line are calculated as well [36] and a size of ground plane bigger than $\lambda/2$ at the lower band is defined. At this stage, the DRA is dual-band with linear polarization and, to turn this antenna into a circularly-polarized one, the anisotropic regions are introduced. Next, w_a and ε_z are tuned to achieve values of axial ratio at least close to 3 dB at both bands. Afterward, l_a is optimized to tune the results mainly at the lower band and, finally, b_a is adjusted to achieve almost perfect circular polarization at the upper band as well.

3.4 Trade-off Between Axial Ratio Bandwidth and DRA Volume

The goal of this chapter is to control the permittivity of a dielectric to create a dual-band CP DRA. In other words, this performance is achieved without relying on complex feeding methods and/or modifications of the overall shape of the DRA. In this scenario, it is important to understand the limitations of the 3-dB axial ratio (AR) bandwidth that could be achieved by relying only upon the dielectric itself. From [56], the theoretical AR bandwidth $BW_{\mathrm{CP}}^{\mathrm{AR}}$ of a single-fed antenna exploiting orthogonal modes can be written as

$$BW_{\mathrm{CP}}^{\mathrm{AR}} \approx AR_{\mathrm{max}}^{\mathrm{dB}} \left[\frac{\ln(10)}{20}\right] \frac{1}{Q} \approx 0.115 \frac{AR_{\mathrm{max}}^{\mathrm{dB}}}{Q}, \tag{3.5}$$

where Q is the quality factor of the resonating mode and $AR_{\mathrm{max}}^{\mathrm{dB}}$ is the level of axial ratio considered as reference to calculate the bandwidth. Throughout this work, $AR_{\mathrm{max}}^{\mathrm{dB}}$ will be equal to 3 dB. From this equation, it is important to have in mind that the AR bandwidth $BW_{\mathrm{CP}}^{\mathrm{AR}}$ is inversely proportional to the Q-factor.

To understand the natural limitation in terms of 3-dB AR bandwidth, an isotropic and homogeneous DRA with a square base is considered. The Q-factors and resonance frequencies of its $\mathrm{TE}_{111}^{x,y}$ and $\mathrm{TE}_{113}^{x,y}$ modes are calculated using the Eigenmode solution of Ansys HFSS considering an infinite ground plane. In addition, the theoretical 3-dB AR bandwidths of the fundamental and higher-order modes are calculated using Eq. 3.5 as a function of the relative permittivity ε_r of the dielectric. For every single value of ε_r the width w and height b of the dielectric are recalculated so that the resonance frequencies of the $\mathrm{TE}_{111}^{x,y}$ and $\mathrm{TE}_{113}^{x,y}$ modes appear always at the center of the L5 and L1 bands, respectively. Therefore, Fig. 3.24 shows the Q-factor and the theoretical 3-dB axial ratio (AR) bandwidth calculated using Eq. 3.5. One can note that the Q-factor of the $\mathrm{TE}_{113}^{x,y}$ modes are always higher than for the $\mathrm{TE}_{111}^{x,y}$ ones, which means that these higher-order modes will always present a narrower AR bandwidth. Also, the AR bandwidth is inversely proportional to ε_r. It is important to point out that, as the value of ε_r decreases to values close to 1, it becomes more difficult to excite the modes, especially the ones with lower Q-factor.

To keep $\mathrm{TE}_{111}^{x,y}$ and $\mathrm{TE}_{113}^{x,y}$ modes resonating at the L5 and L1 bands, respectively, for different values of ε_r, it is necessary to adjust the width and height of the square-based DRA. The volume of the DRA thus changes as ε_r varies. Figure 3.25 presents the volume, in cm^3, of the DRA as a function of ε_r. As expected, it is possible to note that the volume is inversely proportional to the relative permittivity of the dielectric. Therefore, as the AR bandwidth is inversely proportional to ε_r as well, it is necessary to take into account the specifications of the system in order to properly chose the permittivity of the DRA.

Even though the analysis of the 3-dB AR bandwidth is made considering an isotropic and homogeneous DRA, this analysis can be used as a reference for the inhomogeneous and anisotropic DRA to provide a good estimation of the maximum 3-dB AR bandwidth that could be achieved, since most of the proposed antenna is isotropic and only one component

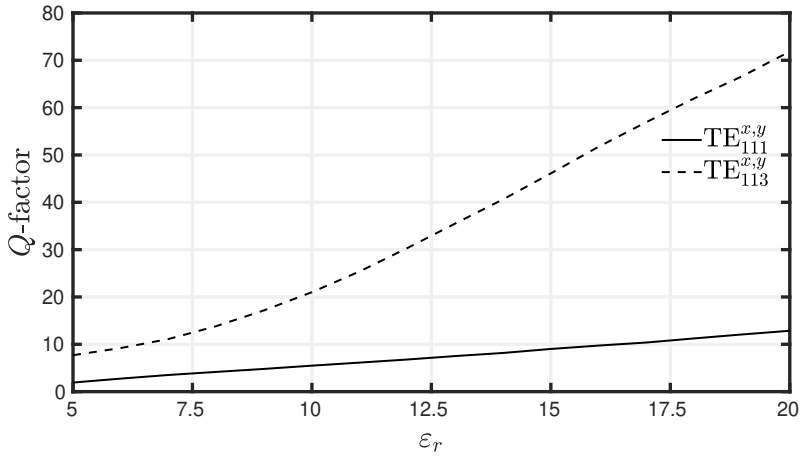

(a)

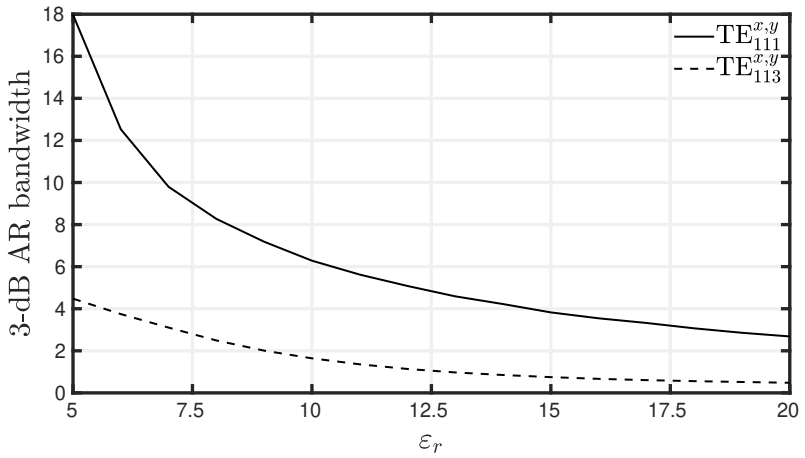

(b)

Figure 3.24: (a) Q-factor and (b) theoretical 3-dB axial ratio bandwidth as a function of ε_r.

of the tensor of permittivity of the anisotropic region has a different value. For the sake of comparison, Table 3.2 presents the values of maximum theoretical 3-dB AR bandwidth for $\varepsilon_r = 10$ calculated using Eq. 3.5 and the values obtained in Section 3.2 for the inhomogeneous and anisotropic DRA, which are referred to as theoretical and simulated, respectively. One can note that the simulated results are lower than the theoretical ones, as expected, as the ε_z is higher than 10, which increases the Q-factor and decreases the AR bandwidth. However, the results are reasonable, which means that the isotropic and homogeneous case can be used to estimate the maximum AR bandwidth of the proposed model. Also, there is an important relationship between the volume and AR bandwidth, which can be chosen according to the specifications of a given communication system. For instance, for the L5 and L1 bands, the axial ratio bandwidth presented in Section 3.2 would be enough to cover both bands, once the required bandwidths are 1.74% and 1.30% and it was achieved 5.00% and 1.46% at the lower and upper bands, respectively. However, depending on the platform, the proposed

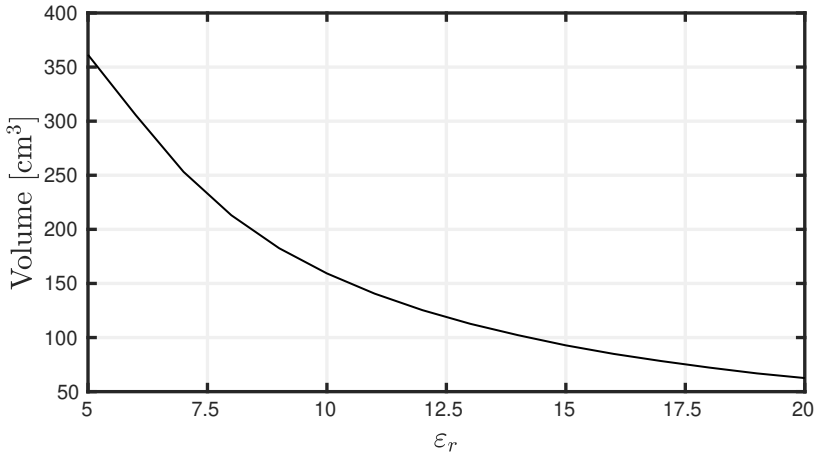

Figure 3.25: Volume of the DRA as a function of ε_r.

antenna could be too bulky. Therefore, it would be necessary to carefully check the required specifications and the space available. Then, the permittivity can be chosen and the same reasoning presented in Sections 3.1 and 3.2 can be applied to design the proposed dielectric resonator antenna at different frequencies with different materials.

	3-dB AR bandwidth	
	lower band	upper band
Theoretical	6.1%	1.8%
Simulated	5%	1.46%

Table 3.2: Maximum theoretical and simulated 3-dB AR bandwidth.

3.5 Conclusion

A dual-band circularly-polarized dielectric resonator antenna has been proposed and investigated. It is designed to operate at the L5 and L1 bands of the GNSS system. The circular polarization is achieved by adding two anisotropic regions inside the square-based rectangular DRA, which allows the presence of circular polarization at two bands using a single microstrip-coupled slot to excite the radiating modes of the DRA.

The novelty of the proposed DRA relies on the fact that the circular polarization is achieved at two bands due to the manipulation of the artificial electric properties of the dielectric by itself and not due to shape modifications and/or complex feeding methods. A single slot is used to excite a pair of fundamental ($\mathrm{TE}^x_{\delta 11}$ and $\mathrm{TE}^y_{1\delta 1}$) and higher-order ($\mathrm{TE}^x_{\delta 13}$ and $\mathrm{TE}^y_{1\delta 3}$) modes at the L5 and L1 bands, respectively, with the same amplitude, while the phase quadrature at each band is achieved due to the presence of two uniaxial anisotropic regions.

The proposed design has simulated impedance bandwidths ($|S_{11}| < 10$ dB) of 17.96% (1065.0 MHz - 1275.1 MHz) and 10.62% (1513.8 MHz - 1668.4 MHz). The simulated 3-dB axial ratio bandwidths are 5.00% (1140.3 MHz - 1198.8 MHz) and 1.46% (1562.8 MHz - 1585.7 MHz), covering both L5 and L1 bands, respectively. Finally, broadside radiation patterns are observed as expected, due to the radiating modes at issue.

In this chapter, the properties of the isotropic and anisotropic dielectrics have directly been assigned on Ansys HFSS. However, in real life, it would not be so simple to manufacture this antenna, since materials with such electric properties would not necessarily be available. On the other hand, the concept of periodic structures and additive manufacturing can be used to do so, as presented in the following chapter.

Chapter 4

Dielectric Periodic Structures and Additive Manufacturing

Contents

In the previous chapter, an inhomogeneous and anisotropic dielectric resonator antenna has been proposed. This antenna presents isotropic and anisotropic regions with optimized values of permittivity. To manufacture this antenna, dielectrics with the needed features will not necessarily be available. To overcome this issue, additive manufacturing can be employed. Thus, in this chapter, an introduction to additive manufacturing (AM) of dielectric periodic structures is presented. In Section 4.1, an overview of AM is introduced, where a historical perspective and their different processes are discussed. Section 4.2 then presents more specifically a state-of-the-art of 3D-printed dielectric resonator antennas. In Section 4.3, an isotropic unit cell is proposed and different methods to retrieve their effective permittivity are discussed. Finally, in Section 4.4, a uniaxial anisotropic unit cell is presented.

4.1 Additive Manufacturing

Additive manufacturing (AM), also referred to as three-dimensional (3D) printing, is a transformative approach to create three-dimensional objects by deposing a printing material. This material can be metal, plastic, or ceramic, to name a few. Also, 3D-printing technology uses data computer-aided-design (CAD) models or 3D object scanners to control the 3D printer, allowing the fabrication of complex objects, layer upon layer, with great flexibility and low-manufacturing cost [1].

Even though the AM has been in the spotlight over the last decade, its first stage dates from 1981, when Hideo Kodama developed a rapid prototyping method using a layer-upon-layer approach [8]. In 1986, Charlie Hull filed the first patent for a 3D-printing technology known as stereolithography (SL), and, then, in 1988, he founded the 3D Systems Corporation, which was the first company to commercialize a 3D printer. This method is the most common vat photopolymerization process, where a photosensitive-liquid resin is polymerized by ultraviolet light, layer by layer, and this process is illustrated in Fig. 4.1. Also, Hull developed the STL file format, which is the file that 3D printers most commonly use today.

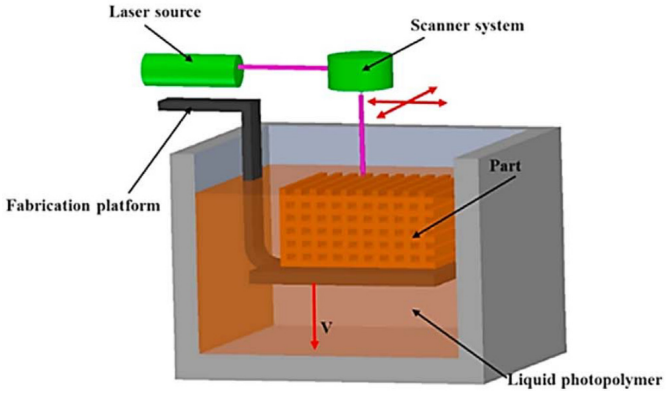

Figure 4.1: Scheme of the SL process [57].

In 1989, Carl Deckard, at the University of Texas, submitted the patent for Selective Laser Sintering (SLS) technology. This method belongs to the class of powder bed fusion (PBF) processes, which are techniques that employ a laser or an electron beam to sinter a powdered material into a solid object. The usual setup of the SLS technology is illustrated in Fig. 4.2. Moreover, SLS can be used for a variety of plastics, ceramics, glass, metals, and alloy powders [58].

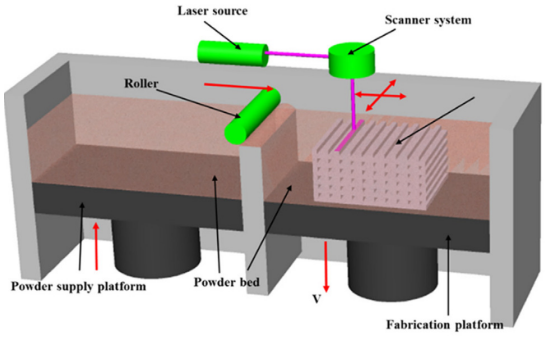

Figure 4.2: Scheme of the SLS process [57].

In the meantime, Scott Crump filed a patent for the Fused Deposition Method (FDM) technology. Differently from the SLS method that uses a laser or an electron beam, in the FDM, the filament is directly extruded from a heated nozzle to create the desired 3D object and the scheme of this method can be seen in Fig. 4.3. With his wife Lisa Crump, he founded the company Stratasys Inc., which is a worldwide leader in FDM technology.

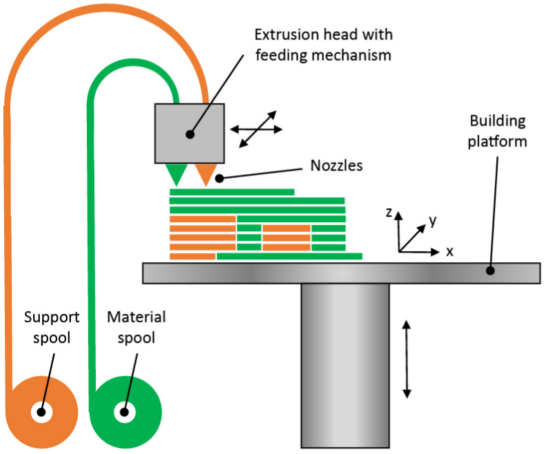

Figure 4.3: Scheme of the FDM process [59].

Even today, the SL, SLS, and FDM are the most used AM techniques. However, with the widely interesting in AM, different techniques have been proposed lately, such as Laminated Engineered Net Shaping (LENS) [60], Polyjet [61], Direct Metal Laser Sintering (DMLS) [62], Selective Laser Melting (SLM), and Electron Beam Melting (EBM) [63], among others.

With the fast development of different AM methods, different industry segments have been exploring this technology. Nowadays, 3D-printed components are highly demanded in the aviation [64], automotive [65], medical [3], construction [5], food [6], and aerospace [66] industries due to their design flexibility, low cost, easy and fast prototyping when compared to other traditional methods [1].

When it comes to the 3D-printing technology, the selection of the printing material is a key element. It is necessary to ensure that the printing material has the characteristics needed for the application. In this context, 3D printing brings a lot of possibilities since it is possible to use a wide variety of materials such as ceramics, metals, polymers, carbon fibers, and concrete, among others.

Owing to their various excellent properties, the use of ceramics in 3D printing has been increasing with each passing day due to their advantages over traditional materials such as polymers and metal. Ceramics present outstanding mechanical, electrical, chemical, and thermal properties such as electrical insulation, resistance to corrosion and high temperature, ionic conduction, chemical inertness, strength, and stiffness, which are very important characteristics for different applications. Due to these features, ceramics are highly demanded in applications that go from gas turbines, nuclear reactors, batteries, and heat exchangers to medical tooling, dental products, and decoration components [67, 68, 69, 70].

In this work, zirconia (zirconium dioxide, ZrO_2) is used as printing material due to its electromagnetic properties such as low loss ($\tan\delta = 1.9 \times 10^{-4}$) and high relative permittivity ε_r equal to 32.5 while presenting high mechanical robustness and resistance. Also, this material has been extensively investigated due to its biocompatibility [68] and chemical resis-

tance [71]. Such characteristics make the zirconia very useful to create components for harsh environments such as space, for instance.

4.2 Additive Manufacturing for Dielectric Resonator Antennas

Over the last couple of years, the three-dimensional (3-D) printing technology, also known as additive manufacturing (AM), has been extensively employed and investigated in the context of antenna applications due to its numerous advantages such as low cost, high degree of freedom regarding the design, eco-friendliness, easy and fast prototyping, to name a few [1, 59]. In this context, 3D printing allows the realization of different devices for a variety of purposes such as horn [72], reflector [73], lens [74, 75], spiral [76], and dipole antennas [77].

The 3D-printing technology has the potential to increase the use of DRAs since it allows the design of complex shapes at a reduced cost. The influence of the use of this technology in DRAs can be summarized by Stuart A. Long, one of the first authors to publish about DRAs in the early 1980s, and David R. Jackson, who stated recently in [78]: "*The dielectric resonator antenna has to date not seen as many applications as the microstrip antenna; the main obstacle seems to be the higher cost of its more complicated fabrication. However, once new manufacturing techniques such as 3-D printing are further established, and reduced size versions of these radiators for use at very high-frequency operations become available, their use is likely to become much more pervasive.*" Finally, as the developments of 3D-printed DRAs are recent and not completely established, the literature about the subject is still limited and some of these works are discussed in the following.

In [79], to show the potential of the 3D-printing technology, super-shaped dielectric resonator antennas (S-DRAs) have been manufactured, as shown in Fig. 4.4, using a photopolymer ($\varepsilon_r = 2.7$ and $\tan\delta = 0.003$) as printing material. From the measured results, the S-DRAs presented good results and a drastic volume reduction is achieved when compared to the rectangular and cylindrical DRAs made out of the same material. In this paper, the manufactured DRAs are isotropic and their effective permittivities are the same as the printing material.

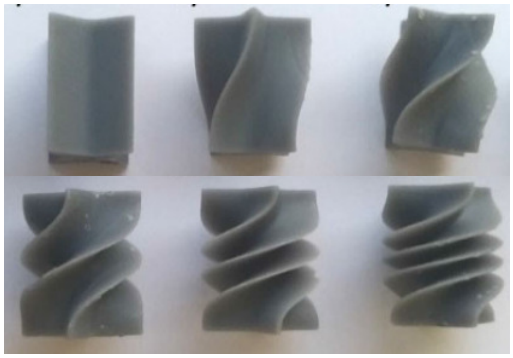

Figure 4.4: 3D-printed super-shaped dielectric resonator antennas [79].

The 3D printing technology has been also used to design circularly-polarized DRAs, as in [14]. In this paper, the authors propose an isotropic elliptical DRA to operate at the L1 band (1575.42 MHz ± 10.23 MHz) for the Global Navigation Satellite System (GNSS) applications, as can be observed in Fig. 4.5(a). Zirconia ($\varepsilon_r = 32.5$ and $\tan\delta = 1.9 \cdot 10^{-4}$ at 10 GHz) is employed as reference material to design the antenna. The unit cell shown in Fig. 4.5(b) was used, where ε_{eff} is controlled by varying the air-dielectric ratio inside the cell. Additionally, the antenna has circular polarization over the L1 band since two orthogonal modes are excited by a coaxial probe, where its position is carefully chosen to excite these modes with the same amplitude and in phase quadrature.

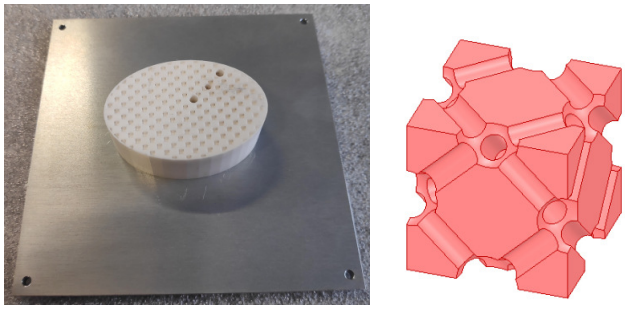

(a) (b)

Figure 4.5: Perspective view of the (a) 3D-printed elliptical DRA and (b) its unit cell [14].

A parametric study is performed in [80] of a 3D-printed hemispherical DRA loaded with a metallic cap. To do so, low-loss dielectric filaments and high-conductive filaments are employed to print the antenna using a low-cost dual-extruding 3D printer. Five hemispherical DRA with different internal patterns with the same external size were designed and evaluated, which can be observed in Fig. 4.6. Also, it has been shown that the introduction of metallic caps can compensate for the different internal designs, *i.e.* different infill percentage, and, thus, maintaining the same resonant frequency for the proposed DRAs. Finally, a maximum reduction of 22% of the weight of the DRA is observed compared to the DRA with 100% of infill percentage.

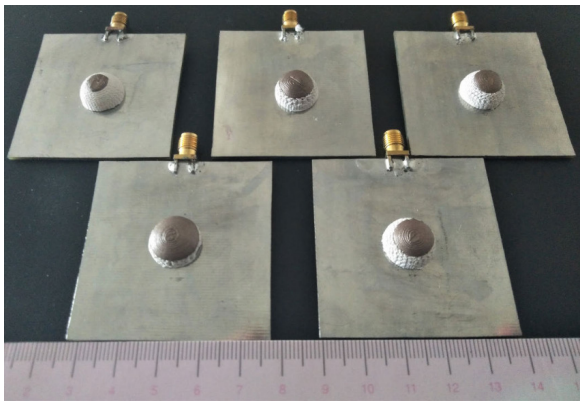

Figure 4.6: Perspective view of the prototypes of the 3D-printed hemispherical DRA loaded with metallic caps [80].

In [81], Xia *et al.* propose a 3D-printed multi-ring dielectric resonator antenna to obtain a wideband of operation, as can be noted in Fig. 4.7(a). This structure consists of four concentric rings in which the value of permittivity decreases from the inner to the outermost ring. More specifically, the relative effective permittivity ε_{eff} of the first (central), second, third, and fourth layers are 10, 8.25, 4.0, and 2.5, respectively. Also, the same printing material is used for the different layers of the antenna, where $\varepsilon_r = 10 \pm 0.4$ (0.1 - 6.0 GHz). To achieve different values of ε_{eff}, dielectric square rings are used, as can be seen in Fig. 4.7(b). The filling ratio theory [75] is employed by varying the periodicity a and thickness t_c of the unit cell to control the value of ε_{eff}. The prototype finally presented a wide measured 10-dB impedance bandwidth of 60.2% (4.3-8.0 GHz) and the overall material cost was less than $20 USD.

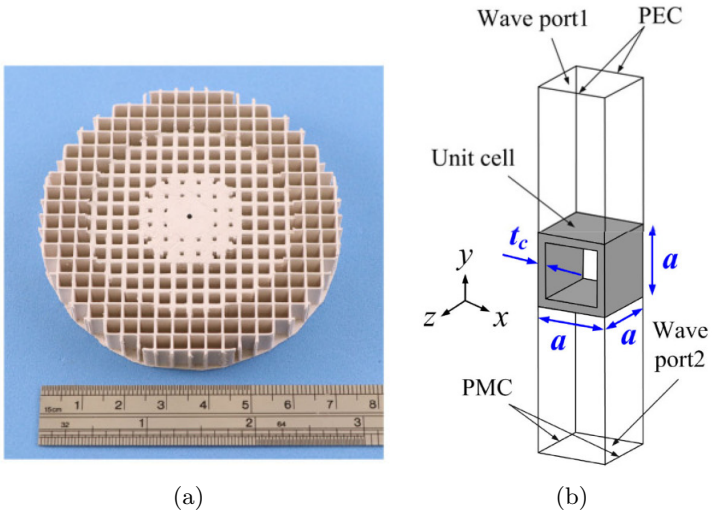

(a) (b)

Figure 4.7: Perspective view of the (a) 3D-printed multi-ring DRA and (b) its unit cell [81].

In [15], a nonhomogeneous dielectric resonator antenna is 3D-printed in ceramics for space applications, as can be seen in Fig. 4.8. This DRA presets two isotropic regions with different values of effective permittivity, even though the antenna is printed using only zirconia as the printing material. The different values of permittivity are achieved due to the use of periodic subwavelength unit cells. The antenna presents dual-band and circular polarization at upper-L-Band (1.559 - 1.61GHz) and S-band (2.025 - 2.29GHz), and the CP is achieved mainly due to a complex feeding network.

In [16], a uniaxial anisotropic rectangular DRA, as can be seen in Fig 4.9(a), is proposed to achieve circular polarization at 2.45 GHz. The authors proposed a unit cell able to create an effective uniaxial anisotropic medium due to its lack of rotational symmetry as shown in Fig. 4.9(b). In addition, this cell presents an effective relative permittivity tensor ε_{eff} equal to [20 0 0; 0 14.5 0; 0 0 14.5]. Differently from [14], the CP is achieved mainly due to the effective dielectric properties of the antenna and not due to its physical shape, since the proposed rectangular DRA is square-based. Also, the reference material to design the antenna is zirconia as well.

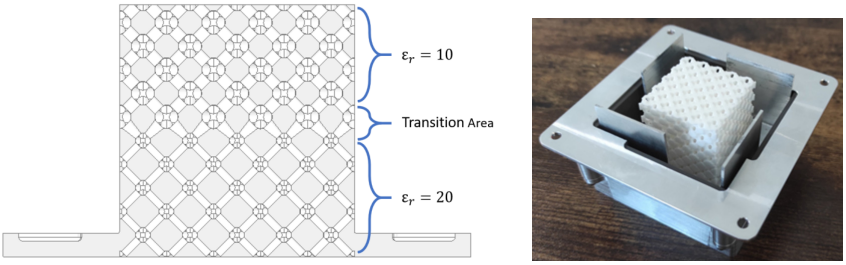

(a) (b)

Figure 4.8: (a) Schematic and (b) perspective views of the 3D-printed nonhomogeneous dielectric resonator antenna [15, 82].

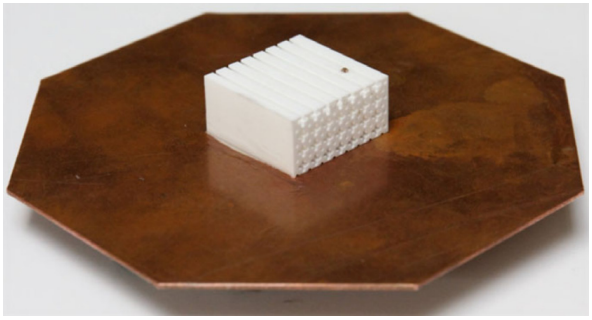

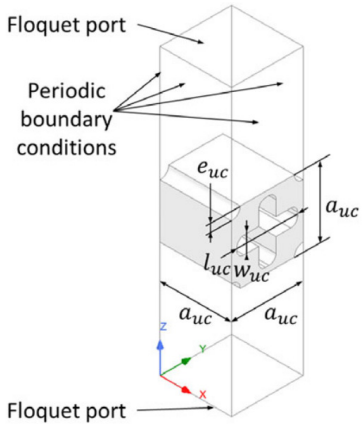

(a) (b)

Figure 4.9: Perspective view of the (a) 3D-printed anisotropic rectangular DRA and (b) its unit cell [16].

Finally, in this section, some of the few works on 3D-printed DRAs found in the literature have been shown, which can demonstrate the advantages of this type of technology. To be more specific, from only one reference material, it is possible to design artificial isotropic, anisotropic, homogenous, and/or inhomogeneous dielectrics, which opens up a variety of new possibilities in this research field. In the previous chapter, the use of isotropic and anisotropic dielectric regions is proposed to design a dual-band circularly-polarized DRA, which has not been investigated so far in the literature. Therefore, the possibility of having these artificial dielectric media is studied in the next sections by using the 3D printing of ceramics.

4.3 Design of the 3D-Printed Isotropic Unit Cell

This section presents a unit cell proposed to emulate an artificial isotropic medium considering different parameter retrieval methods to provide a better and complete understanding of it. To have an effective isotropic medium, the cell has to present symmetry along the x-, y- and

z-axes. In this scenario, different cubic lattices can be used and the main ones are the simple cubic, body-centered cubic (BCC), and face-centered cubic (FCC), which are presented in Fig. 4.10 [83]. All of these structures are typically used to design isotropic cells, however, the effective permittivity ε_{eff} can slightly change according to the electric-field polarization used to calculate it. In other words, depending on the electric-field polarization and on the symmetry of the cell, the ε_{eff} can be slightly anisotropic. The list from the most to the least symmetric lattices is: FCC, BCC, and simple cubic [84].

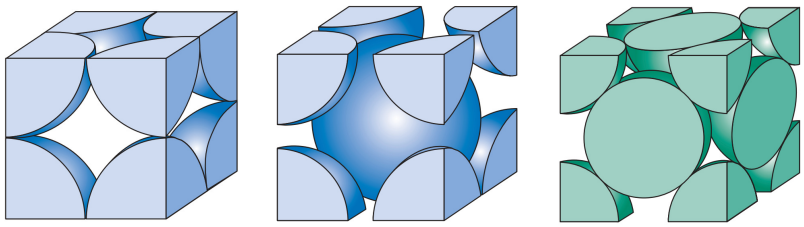

(a) Simple cubic (b) BCC (c) FCC

Figure 4.10: (a) Simple, (b) body-centered, and (c) face-centered cubic lattices [85].

In this work, the simple cubic has been chosen because the proposed antenna needs an anisotropic region with a large birefringence, which could be achieved by modifying a lesser symmetric lattice initial isotropic unit cell. The proposed unit cell is presented in Fig. 4.11, where zirconia is used as a reference material, which has $\varepsilon_r = 32.5$ and $\tan\delta = 1.9 \cdot 10^{-4}$ at 10 GHz. It consists of cubic zirconia elements in each corner of the unit cell connected to each other by small pieces of zirconia.

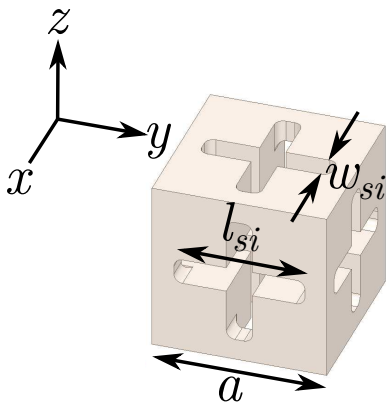

Figure 4.11: Proposed isotropic unit cell.

It should be noted that the elementary cell must be much smaller than the operating wavelength so that the medium can be considered homogeneous and characterized by an effective permittivity. Different parameter retrieval methods are now presented in the following to calculate the effective permittivity of the proposed unit cell.

4.3.1 Parameter Retrieval Methods

4.3.1.1 *S*-Parameters Retrieval Method

The *S*-parameters are here used to characterize the isotropic unit cell using Ansys HFSS, which consists in the employment of Floquet ports and Master/Slave boundary conditions, as described in Appendix A. This method is used in different works to compute the effective permittivity of unit cells for dielectric resonator antennas [14, 15, 16]. The idea here is to control the permittivity of a zirconia-made unit cell in order to have an effective permittivity ε_{eff} equal to 10, which is the optimal value needed to design the antenna proposed in Chapter 3.

The effective relative permittivity of the unit cell ε_{eff} is controlled by the filling ratio $\delta_i = \frac{V_{\text{zirconia}}}{V_{\text{cell}}}$, where V_{zirconia} is the volume of zirconia inside the unit cell and V_{cell} is the total volume of a cube of periodicity a. In other words, to control the effective permittivity, it is necessary to control the volume of air and zirconia inside the cell. To illustrate it, Fig. 4.12 shows ε_{eff} as a function of δ_i computed considering an x-directed electric field polarization at 1.575 GHz, where a is equal to 4 mm. As expected, one can note that the ε_{eff} and δ_i are proportional to each other. Finally, the effective permittivity ε_{eff} is equal to 10 for a filling ratio $\delta_i = 0.64$.

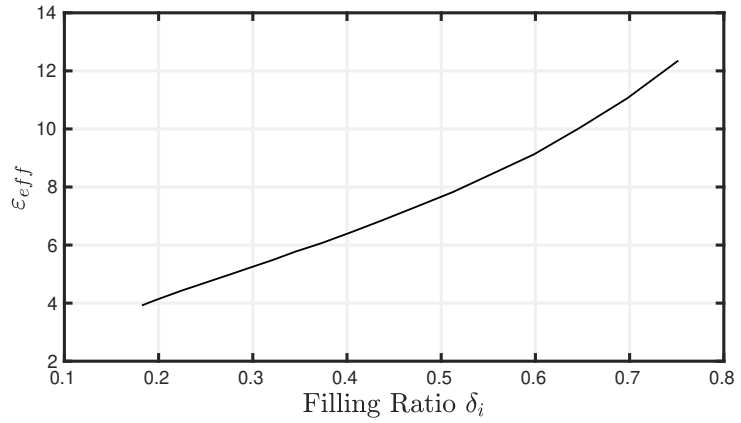

Figure 4.12: Calculated effective dielectric constant of the cells computed on Ansys HFSS with respect to the filling ratio δ_i of the unit cell at 1.575 GHz using the *S*-parameters retrieval method.

A common rule-of-thumb found in the literature suggests that the lattice of the unit cell is supposed to be smaller than a quarter of the wavelength to avoid dispersion, which happens when the unit cells start to resonate by themselves [86]. To verify it, Fig. 4.13(a) shows the effective permittivity ε_{eff} as a function of the frequency with $a = 4$ mm, $w_{si} = 0.6$ mm, and $l_{si} = 2.99$ mm, namely what has been calculated to achieve permittivity of 10 at the L5 and L1 bands. One can note that the calculated effective permittivity decreases as the frequency increases. To understand better this variation, Fig. 4.13(b) presents the absolute difference using $\varepsilon_{eff} = 10$ as a reference. For instance, for $a = \frac{\lambda}{10}$ the difference is only 0.6%,

which could be acceptable depending on the application. Therefore, to avoid dispersion and eventually a lack of accuracy of the S-parameters retrieval method for electrically-large cells, the best practice is to use a unit cell as small as possible taking into account the manufacturing limitations.

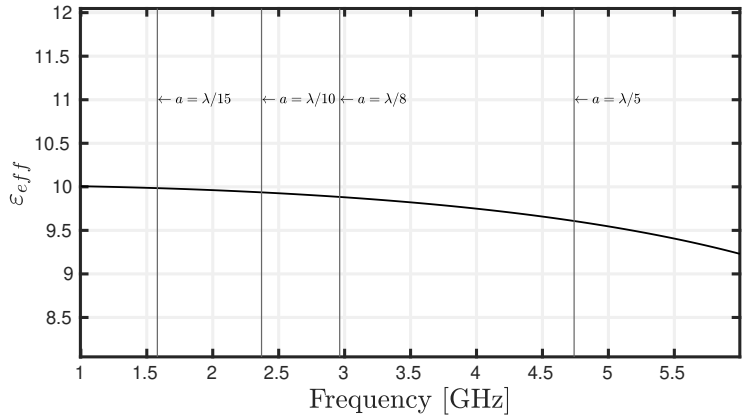

(a)

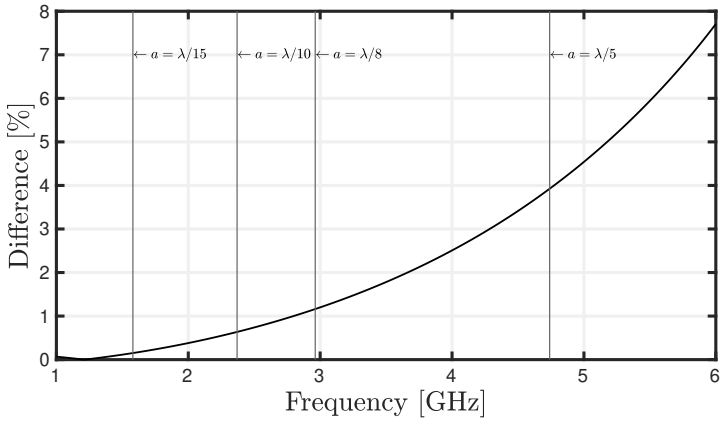

(b)

Figure 4.13: (a) Calculated effective permittivity and (b) absolute difference of the proposed unit cell calculated using the S-parameters retrieval method and for $a = 4$ mm, $w_{si} = 0.6$ mm, and $l_{si} = 2.99$ mm.

Finally, the S-parameters retrieval method is a fast and straightforward way to calculate the effective permittivity of a periodic structure made up of subwavelength unit cells. However, it relies on several assumptions that restrict its ability to compute the unit cell dispersion with a good accuracy, which can be a problem for electrically-large cells. Therefore, the dispersion diagram can be useful in this scenario, which is presented following in this section.

4.3.1.2 Dispersion Diagram

Dispersion can be defined as any situation where the electromagnetic properties change. Different types of dispersion can be observed such as chromatic, polarization, and spatial ones. The chromatic dispersion occurs when the material/medium electromagnetic properties change as a function of frequency. A classical example is a dispersive prism since it separates the light into its spectral components, *i.e.* the colors of the rainbow, since each color has a different wavelength and, thus, experiencing a different refractive index and refracting at different angles, as can be seen in Fig. 4.14(a). On the other hand, when the material properties are a function of the polarization of the wave, the polarization dispersion takes place, as can be observed in Fig. 4.14(b). Finally, spatial dispersion is present when the material property is a function of the direction of the wave. To be more specific, this effect appears when waves in different directions travel at a different velocity, as can be observed in Fig. 4.14(c).

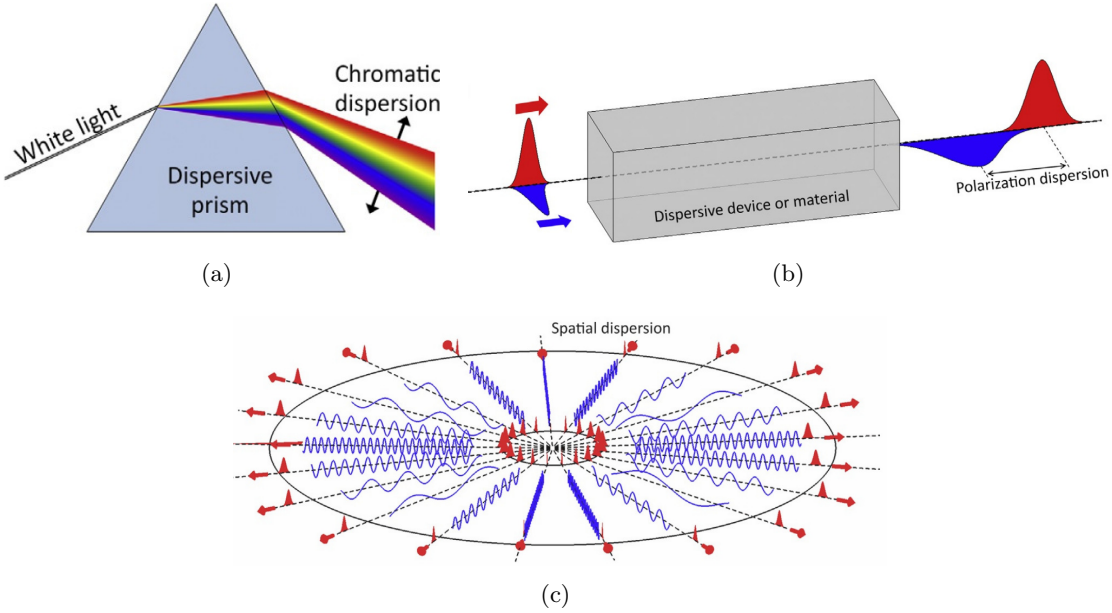

Figure 4.14: Illustration of (a) chromatic, (b) polarization, and (c) spatial dispersions [86].

In this scenario, the dispersion relation is an important expression that relates the wave vector $\vec{k}$ to the frequency ω, which can be interpreted as quantification of $\vec{k}$ as a function of the direction and frequency. Considering a linear, homogeneous and isotropic (LHI) medium, and replacing the plane wave solution with its wave equation, the dispersion relation can be written as

$$k_x^2 + k_y^2 + k_z^2 = k^2 = (k_0 n)^2, \tag{4.1}$$

which describes the surface of a sphere, since waves in LHI media experience the same refractive index in all directions and where n is the refractive index of the material. This surface is known as a dispersion surface and describes the spatial dispersion of a material.

For anisotropic media, the dispersion relation is a little bit more complicated, however, almost the same reasoning used for LHI media can be used here. The only difference is that the permittivity in the wave equation in an LHI medium is scalar and, thus, the mathematical development is easier. On the other hand, for a linear, homogeneous, and anisotropic (LHA) medium, the permittivity is a tensor and, then, the mathematical development is a little bit more complicated but it is still straightforward. For a biaxial medium, *i.e.* $n_x \neq n_y \neq n_z$, the dispersion relation can be written as [86]

$$\begin{aligned} &|\vec{k}|^2 \left[\left(\frac{k_x}{n_y n_z} \right)^2 + \left(\frac{k_y}{n_x n_z} \right)^2 + \left(\frac{k_z}{n_x n_y} \right)^2 \right] \\ &- k_0^2 \left[\frac{k_y^2 + k_z^2}{n_x^2} + \frac{k_z^2 + k_x^2}{n_y^2} + \frac{k_x^2 + k_y^2}{n_z^2} \right] + k_0^4 = 0, \end{aligned} \tag{4.2}$$

where n_x, n_y, and n_z are the refractive index experienced by the waves purely polarized in the x-, y-, and z-directions, respectively.

When $n_x = n_y \neq n_z$, the material is said to be uniaxial anisotropic and its dispersion relation can be rewritten as [86]

$$\underbrace{\left(\frac{k_x^2 + k_y^2 + k_z^2}{n_o^2} - k_0^2 \right)}_{\text{Sphere Ordinary Wave}} \underbrace{\left(\frac{k_x^2 + k_y^2}{n_e^2} + \frac{k_z^2}{n_o^2} - k_0^2 \right)}_{\text{Ellipse Extraordinary Wave}} = 0, \tag{4.3}$$

where $n_o = n_x = n_y$ is the ordinary refractive index and $n_e = n_z$ is the extraordinary refractive index. One can note that the dispersion relation of the uniaxial material has two solutions, which correspond to the two polarizations (TE and TM). The first solution is the same as an isotropic medium and describes a sphere, *i.e.* it is like the wave is propagating through an isotropic medium with refractive index n_o. However, the second solution describes an ellipsoid, which means that the refractive index will be somewhere between n_o and n_e, depending on its direction.

When it comes to periodic structures, it is important to retrieve their effective electromagnetic properties to properly use them at a given frequency. However, these properties can be different for different frequency ranges. To be more specific, for periodic structures made out of dielectric with small lattices compared to the wavelength, it is possible to retrieve consistent effective properties from DC up to a cutoff frequency. Below this cutoff frequency, the periodic structure is nonresonant and, above it, a resonant behavior is observed and, thus, its properties can change significantly. This cutoff frequency can be determined from the electromagnetic band diagram, or simply dispersion diagram, by identifying the frequency in which the lowest-order electromagnetic band of the periodic structure starts to deviate from the light line, *i.e.* when the dispersion begins. Also, the dispersion diagram can be used to calculate the effective permittivity of the unit cell by using the following equation

$$\varepsilon_r = \left(\frac{k\lambda_0}{2\pi}\right)^2. \tag{4.4}$$

In this work, the dispersion diagram is computed using the Eigenmode solution of the Ansys HFSS, where three pairs of Master/Slave boundary conditions are assigned on each face of the proposed isotropic unit cell shown in Fig. 4.11. Here, the analyses are made considering the dimensions of the unit cells calculated previously with the S-parameter retrieval method and, then, the dispersion diagram is presented to provide a complete investigation of the unit cell at issue.

Considering $a = 4$ mm, $w_{si} = 0.6$ mm, and $l_{si} = 2.99$ mm, the dispersion diagram of the lowest-order electromagnetic (EM) band is shown in Fig. 4.15, taking into account the irreducible Brillouin zone (IBZ) shown in the same figure, which is appropriate for simple cubic crystal structures. It is possible to note that the EM band starts to deviate from the light line around 4 GHz and, thus, the structure is dispersive above this cutoff frequency. In other words, the effective parameters of the unit cell is consistent for frequencies up to 4 GHz, which is illustrated by the blue region. Considering an effective permittivity of 10, at the cutoff frequency, the lattice of the unit cell is equivalent to $\lambda/5.93$.

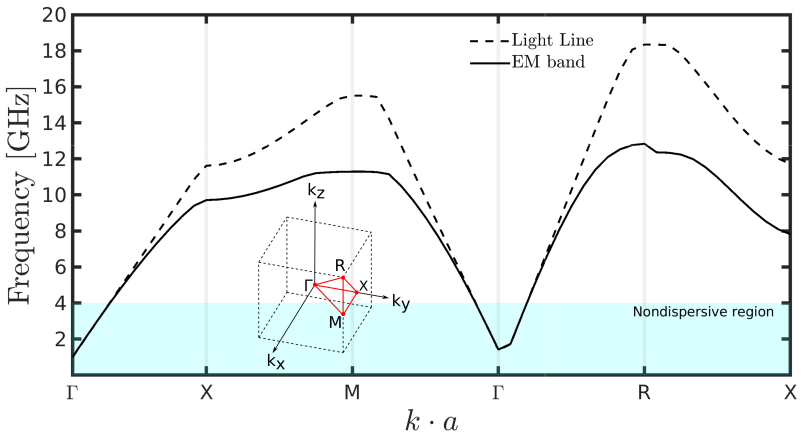

Figure 4.15: Dispersion diagram of the proposed isotropic unit cell and its irreducible Brillouin zone considering a unit cell with $a = 4$ mm, $w_{si} = 0.6$ mm, and $l_{si} = 2.99$ mm.

Using Eq. (4.4), the effective permittivity is calculated considering the path Γ-X of the IBZ of the proposed unit cell and compared to the one obtained from the S-parameters retrieval method, as shown in Fig. 4.16, where the same x-directed electric field polarization is taken into account for both analyses. The dimensions of the cell are $a = 4$ mm, $w_{si} = 0.6$ mm, and $l_{si} = 2.99$ mm. In Fig. 4.16(a), one can note that the curves of effective permittivity have different behaviors. More precisely, for cells smaller than $\lambda/10$, the results are different but the difference considering $\varepsilon_{eff} = 10$ as a reference is lower than 2%, as can be seen in Fig. 4.16(b), which we consider acceptable since two different analytical and numerical methods are employed. It is important to point out that this difference is calculated using $\varepsilon_{eff} = 10$

as a reference and the cells are optimized with the S-parameters method, which means that the difference is relative to the retrieval method used in this analysis. Moreover, as the cell is getting electrically bigger, the permittivity for the dispersion diagram method increases whereas it reduces for the S-parameters method, which could indicate a limitation of some of these methods for electrically-large cells. However, when the cell is smaller than $\lambda/10$, both methods are equivalents with a small discrepancy.

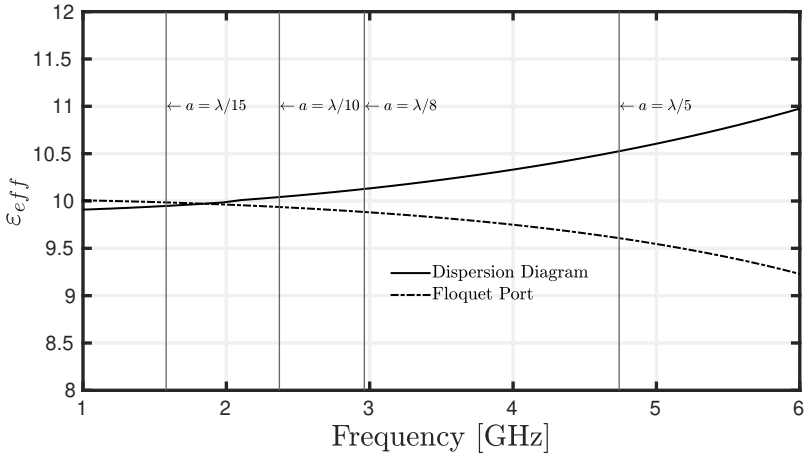

(a)

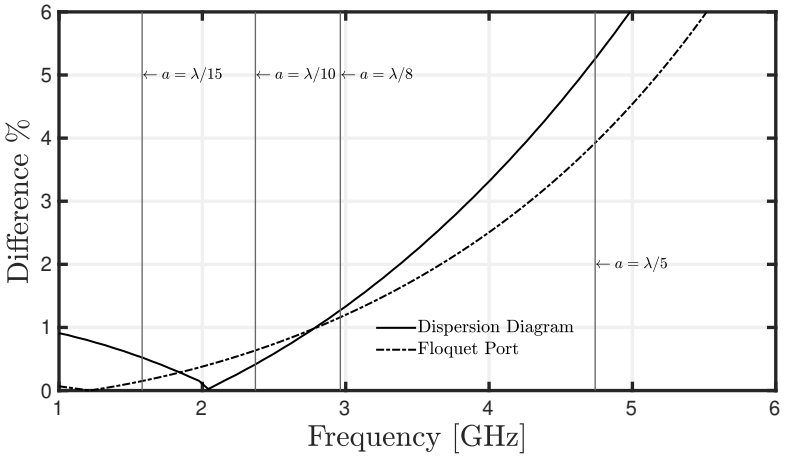

(b)

Figure 4.16: (a) Effective permittivity and (b) absolute permittivity difference of the proposed unit cell calculated using the dispersion diagram and the S-parameters method with $a = 4$ mm, $w_{si} = 0.6$ mm, and $l_{si} = 2.99$ mm.

As aforementioned, the effective permittivity can be extracted from the dispersion diagram using Eq. (4.4), however, depending on the path of the IBZ considered, the electric field polarization may change. To verify the effective permittivity from 1 to 6 GHz, the paths Γ-X, M-Γ, and Γ-R from the dispersion diagram are used, as shown in Fig. 4.17 for $a = 4$ mm and

$a = 12$ mm. Both unit cells are initially designed with the S-parameters retrieval method to achieve $\varepsilon_{eff} = 10$ at 1.575 GHz, assuming that this method works regardless of the electric size of the cell. For $a = 4$ mm, one can note that the curves of permittivity are the same at lower frequencies and they slightly separate from each other as the frequency is getting higher. More precisely, at 6 GHz, the maximum difference between the permittivity curves for $a = 4$ mm is 3.3%, where the cell is electrically bigger, *i.e.* $\lambda/3.95$. On the other hand, for $a = 12$ mm, the difference between the curves of permittivity is important even for lower frequencies. At 3 GHz, the maximum permittivity difference is 18%, where a is equivalent to $a < \lambda/2.64$. Therefore, if the cell is electrically small, *i.e.* $a < \lambda/10$, even considering a simple cubic lattice, the permittivity curves are the same, which means that the level of isotropy of this cell remains good. However, if the cell is electrically large, the lack of isotropy can be a problem, and the FCC or BCC lattices would certainly be more appropriate.

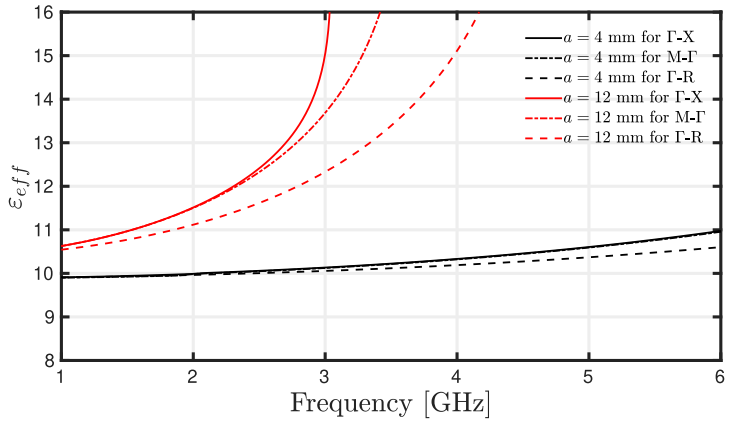

Figure 4.17: Effective permittivities calculated from the dispersion diagram considering different paths of the IBZ for $a = 4$ mm, $w_{si} = 0.6$ mm, and $l_{si} = 2.99$ mm, and for $a = 12$ mm, $w_{si} = 2.9$ mm, and $l_{si} = 7.49$ mm.

4.3.1.3 Dielectric Resonator Based on Periodic Structures

Previously in this section, the S-parameters retrieval and dispersion diagram methods were used to calculate the effective permittivity of the proposed isotropic unit cell. However, especially for electrically-large cells, the results from both methods are quite different. To evaluate which method is more accurate, a cubic dielectric resonator made up of several unit cells can be used to estimate the effective permittivity of the periodic structure using the Eigenmode solution of Ansys HFSS. In this analysis, the resonance frequency of the fundamental $\text{TE}^{x}_{\delta 11}$ mode is tracked by identifying its electric field distribution.

As a starting point, a cubic dielectric resonator is designed so that the fundamental $\text{TE}^{x}_{\delta 11}$ mode resonates at 1.57 GHz considering a homogeneous bulk dielectric with permittivity of 10 directly assigned on Ansys HFSS. This model is referred to as *solid model* and can be observed in Fig. 4.18(a), where w is found to be 37.4 mm. Then, unit cells are used to achieve $\varepsilon_{eff} = 10$ for different sizes a of unit cells, and the models made up of these periodic

structures are referred to as *3D-printed models*, as shown in Fig. 4.18(b). It is important to point out that both models have the same value of w.

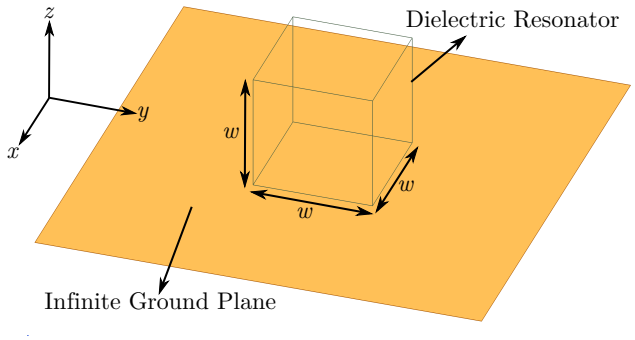

(a) Solid model

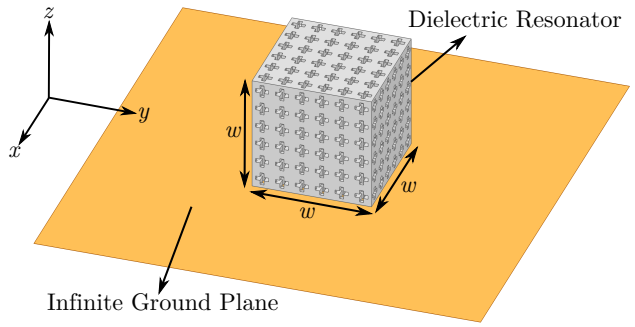

(b) 3D-printed model

Figure 4.18: (a) Solid and (b) 3D-printed models of a cubic dielectric resonator mounted over an infinite ground plane.

In this analysis, the unit cells are designed using the S-parameters retrieval method to achieve an effective permittivity ε_{spar} of 10 at 1.57 GHz for different values of a assuming that this method works regardless of the electric size of the cell. Also, only cells with lattice a that give w/a equal to an entire number are taken into account to avoid issues with incomplete cells in the DR. Table 4.1 shows the dimensions of the cells considered in this analysis.

a	w_{si}	l_{si}	w/a
5.31 mm	1.4 mm	3.35 mm	7
6.23 mm	1.3 mm	4.17 mm	6
7.44 mm	1.6 mm	4.91 mm	5
9.35 mm	2.4 mm	5.83 mm	4
12.4 mm	3.0 mm	7.71 mm	3
18.7 mm	4.4 mm	10.3 mm	2

Table 4.1: Dimensions of the unit cell for different lattices a using the S-parameters retrieval method.

Figure 4.19 shows the resonance frequency of the $TE^{x}_{\delta 11}$ mode as a function of w/a for the 3D-printed model considering values presented in Table 4.1. One can note that, as w/a is increasing, *i.e* the cells are getting electrically and physically smaller, the resonance frequency is getting closer to 1.57 GHz. In other words, for electrically-small cells, the effective permittivity of the cell as calculated by the S-parameters retrieval method is accurate.

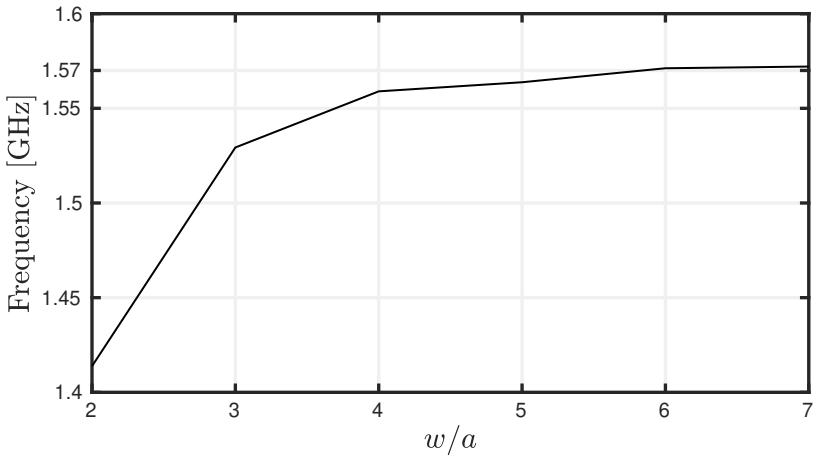

Figure 4.19: Resonance frequency of the $TE^{x}_{\delta 11}$ mode as a function of w/a calculated by the Eigenmode analysis of the 3D-printed DR.

Using the results from Fig. 4.19 and solid model (see Fig. 4.18(a)), it is possible to estimate the effective permittivity of the full DR made up og unit cells. Using this model, its effective permittivity is varied in order to achieve the same resonance frequency for the $TE^{x}_{\delta 11}$ mode obtained with the 3D-printed models. Thus, the effective permittivity ε_{dr} extracted from the dielectric resonator using the Eigenmode solution of Ansys HFSS is presented in Fig. 4.20. As expected, for electrically-small cells, the permittivity is close to 10. However, the effective permittivity increases as a is getting bigger, which is the opposite of what happens with the S-parameters retrieval method described in Subsection 4.3.1.1. On the other hand, the behavior is similar to the one found with the dispersion diagram analysis in the Subsection 4.3.1.2.

Table 4.2 compares the effective relative permittivity found with the S-parameters retrieval method (ε_{spar}), dispersion diagram (ε_{dd}), and Eigenmode analysis with the DR (ε_{dr}). One can note that the column of ε_{spar} is equal to 10 since the cells have been designed to have effective permittivity of 10 using the S-parameters retrieval method. However, for this method, it was observed previously that permittivity decreases as the electric size of the cell increases, which is the opposite behavior observed for the dispersion diagram method (see Fig. 4.16(a)). Using a dielectric resonator to try to understand which method is more accurate for our case, it is possible to note that the dispersion diagram method is more appropriate, especially for electrically-large unit cells, since the effective permittivity increases with the frequency. Figure 4.21 shows the absolute difference of the effective permittivity obtained with the dispersion diagram and S-parameters retrieval method using the results from the Eigenmode analysis with the DR as a reference. One can note that the difference is lower for effective permittivity

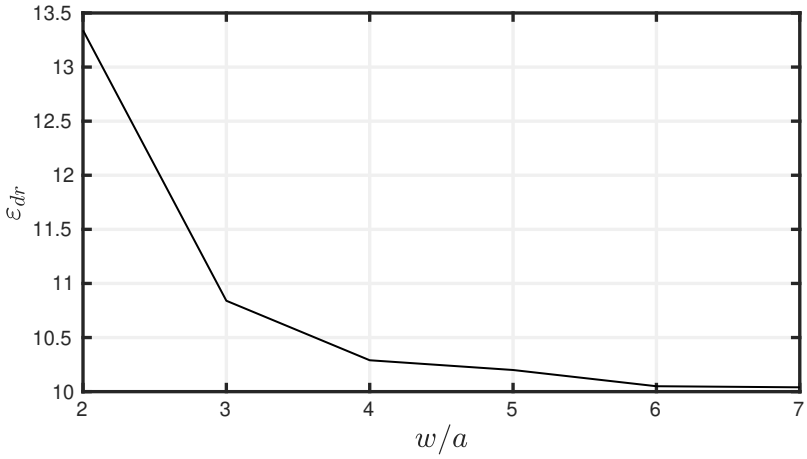

Figure 4.20: Effective permittivity ε_{dr} as a function of w/a calculated from the resonance frequency of the $\mathrm{TE}^{x}_{\delta 11}$ mode.

obtained with the dispersion diagram, as expected. Therefore, it is important to point out that, for electrically-small cells, *i.e.* $a < \lambda/10$ both S-parameters retrieval method and dispersion diagram can be used. Nevertheless, when it comes to electrically-large cells, the dispersion diagram is more accurate to design dielectric resonators using periodic unit cells.

a	ε_{spar}	ε_{dd}	ε_{eigen}
5.31 mm $= w/7 = \lambda/11.33$	10	10.07	10.04
6.23 mm $= w/6 = \lambda/9.27$	10	10.09	10.05
7.44 mm $= w/5 = \lambda/7.44$	10	10.23	10.20
9.35 mm $= w/4 = \lambda/6.40$	10	10.50	10.29
12.4 mm$= w/3 = \lambda/4.99$	10	11.12	10.84
18.7 mm$= w/2 = \lambda/3.22$	10	15.24	13.34

Table 4.2: Effective permittivity computed using the S-parameters retrieval method (ε_{spar}), dispersion diagram (ε_{dd}), and Eigenmode analysis with the DR (ε_{dr}).

So far, the analyses are made considering a dielectric resonator without any feeding source. However, the main goal of this thesis is to design antennas, and, thus, it would be interesting to compare the Eigenmode analysis with the results considering a full-wave simulation of a dielectric resonator antenna. To do so, the models presented in Fig. 4.22 are considered, which are mounted over an infinite ground plane. The antennas are here fed by a coaxial probe and its position allows the excitation of the $\mathrm{TE}^{x}_{\delta 11}$. Also, the same dimension for the dielectric resonator is considered, *i.e.* $w = 37.4$ mm, as well as the unit cell parameters presented in Table 4.1.

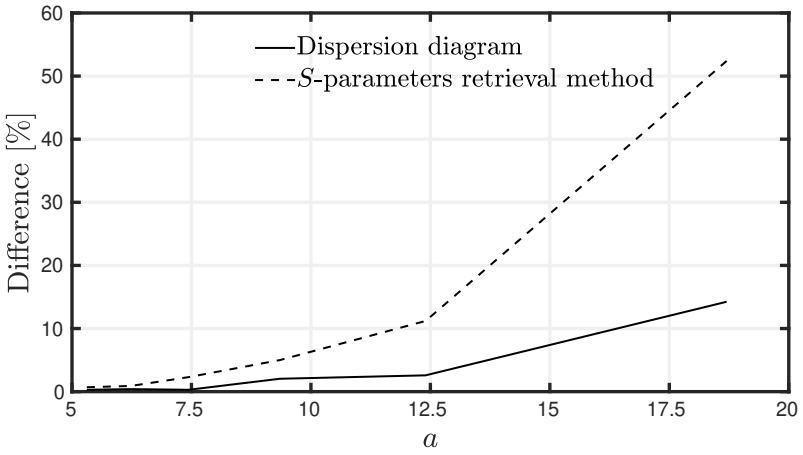

Figure 4.21: Absolute difference of the effective permittivity from the dispersion diagram method and S-parameters retrieval method using the Eigenmode analysis with the DR as a reference.

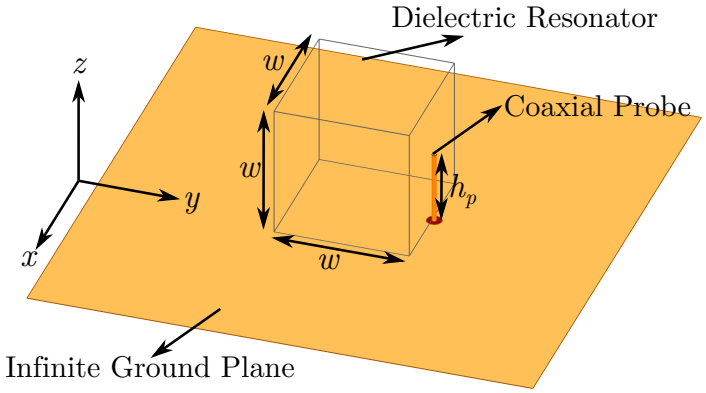

(a) Solid model

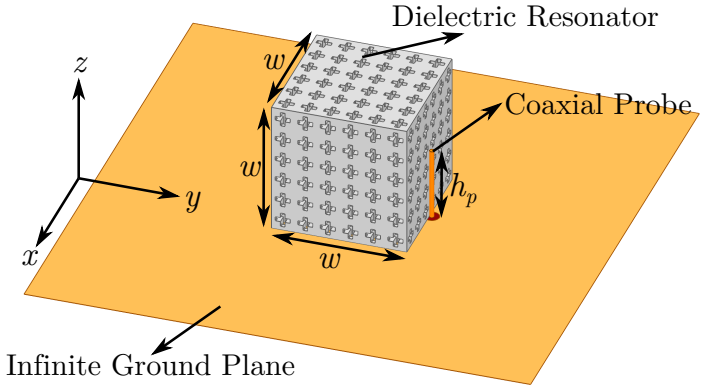

(b) 3D-printed model

Figure 4.22: (a) Solid and (b) 3D-printed models of a cubic dielectric resonator antenna.

Figure 4.23 shows the magnitude of the reflection coefficient $|S_{11}|$, in dB, for the solid and 3D-printed models considering the dimensions of unit cell presented in Table 4.1. For this simulation, the overall dimensions of the DRA are the same for all cases with exception of the height of the coaxial probe that is adjusted for each model to assure impedance matching to 50-Ω. One can note that, as the cells are getting larger, the resonance frequency of the antenna decreases, which means that its effective permittivity is increasing.

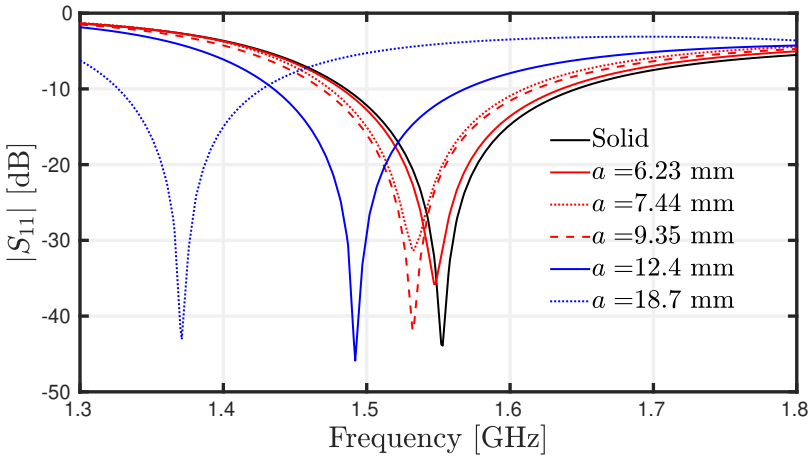

Figure 4.23: Simulated reflection coefficient for the solid and 3D-printed models considering the dimensions of unit cell.

The magnitude of the reflection coefficient $|S_{11}|$ can be used as well to estimate the effective permittivity of the unit cells. In this case, the permittivity of the solid model (see Fig. 4.22(a)) is varied in order to have the minimum $|S_{11}|$ at the same frequencies as the 3D-printed models. Table 4.3 compares the results of effective permittivity obtained with the full-wave and Eigenmode analyses, which are referred to as ε_{fw} and ε_{eigen}, respectively. In the last column, the absolute difference between these methods is presented which is lower than 2%. Therefore, the results are similar for both Eigenmode and full-wave analyses, which agree with the dispersion diagram method as well.

a	ε_{eigen}	ε_{fw}	Difference
6.23 mm $= w/6 = \lambda/9.27$	10.05	10.10	0.50%
7.44 mm $= w/5 = \lambda/7.44$	10.20	10.40	1.96%
9.35 mm $= w/4 = \lambda/6.40$	10.29	10.40	1.07%
12.4 mm$= w/3 = \lambda/4.99$	10.84	11.00	1.48%
18.7 mm$= w/2 = \lambda/3.22$	13.34	13.40	0.45%

Table 4.3: Effective permittivity computed using the S-parameters retrieval method (ε_{spar}), dispersion diagram (ε_{dd}), and Eigenmode analysis with the DR (ε_{dr}).

4.3.1.4 Conclusion

The effective permittivity is here calculated considering three methods that are S-parameters retrieval method, dispersion diagram, and Eigenmode analysis with a DR. It is observed that, for electrically-small cells, both S-parameters retrieval method and dispersion diagram give equivalent results. However, as the cells get electrically larger, their behaviors are completely different. To overcome this issue, an Eigenmode analysis using a DR has been performed. This analysis indicates that the dispersion diagram is more accurate to extract the effective permittivity of the cells for the designing of dielectric resonators since it better takes into account the chromatic dispersion. In other words, the S-parameters retrieval method is not useful when the periodic structure is not homogeneous anymore, which happens when the cell is electrically large. Therefore, if the cell is smaller than $\lambda/8$, *i.e.* considering a difference lower than 1.5% (see Fig. 4.16(b)), we suggest the use of the S-parameters retrieval method, which is much faster than the dispersion diagram analysis, and its results were already verified in different works on DRAs [14, 15, 16]. Nevertheless, if electrically larger unit cells are used, the dispersion diagram seems to be more accurate for dielectric resonators. Also, the Eigenmode analysis can provide accurate results taking into account the dispersion. However, this method demands a lot of computational effort.

4.3.2 Manufacturing Limitations

Previously, it has been observed that it is possible to achieve different values of effective permittivity by just controlling the dimensions of the cell. However, to manufacture these cells, it is important to take into account the capabilities of the 3D printer. In this work, the 3D-printer C900 developed by 3DCeram in France is employed. Like any manufacturing process, some constraints must be respected to ensure the fabrication of a prototype. For the 3D-printer C900 and considering our cell, the main constraints are: the zirconia walls must be thicker than 1 mm and the diameter of the holes must be at least 0.6 mm. Therefore, these constraints may limit the range of effective permittivity that could be achieved with the proposed isotropic unit cell shown in Fig. 4.11.

Taking all of this into account, in Fig. 4.24(a), the effective permittivity of the proposed unit cell is represented at 1 GHz for a equal to 4 mm. Here, it has been calculated with the S-parameters retrieval method that is supposed to work correctly (see Subsection 4.3.1.1). The inner part of the region highlighted on the plot corresponds to the 3D printer capabilities. One can note that it is possible to have printable unit cells with effective permittivity from 1.62 up to 29.7. It is important to understand the maximum frequencies for which these printable cells could be used, taking into consideration the dispersion and limitations of the retrieval method at issue. The maximum frequency depends thus on the criterion adopted to design the cells. For instance, if the criterion is $a < \lambda/10$, the maximum frequency varies from 1.38 GHz to 5.88 GHz, as seen in Fig. 4.24(b). Otherwise, if the criterion is $a < \lambda/6$, as shown in Fig. 4.24(c), the maximum frequency goes from 2.29 GHz up to 9.80 GHz. Therefore, the maximum frequency that a printable unit cell could be used depends on the chosen criterion.

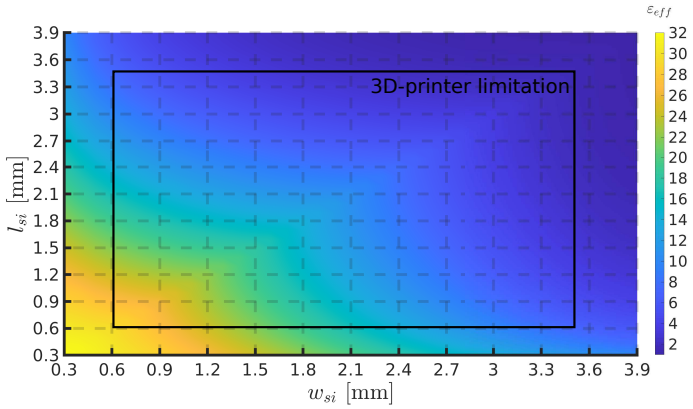

(a) Effective permittivity

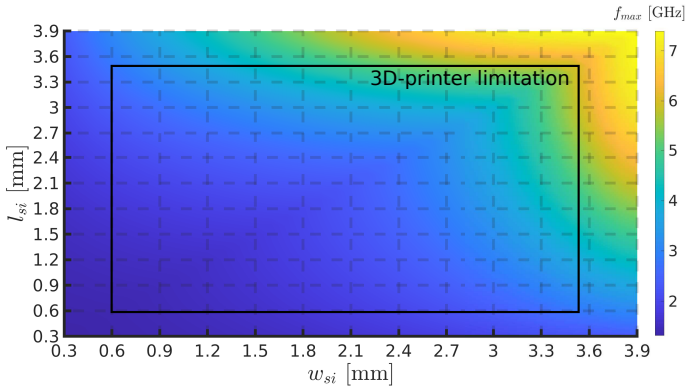

(b) Maximum frequency for $a < \lambda/10$

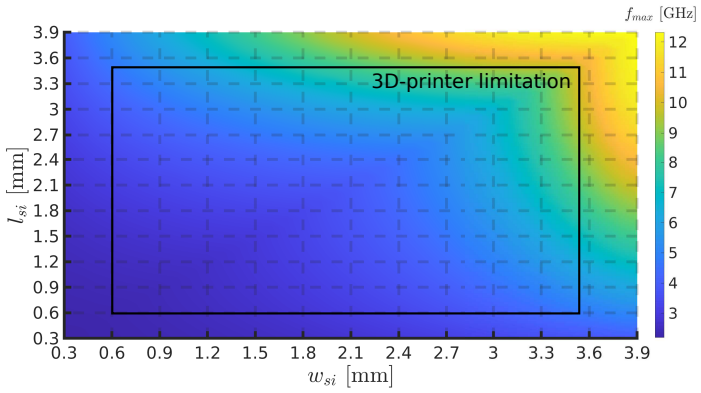

(c) Maximum frequency for $a < \lambda/6$

Figure 4.24: (a) Effective dielectric constant ε_{eff}, (b) maximum frequency f_{max} for $a < \lambda/10$, (c) maximum frequency f_{max} for $a < \lambda/6$ as a function of w_{si} and l_{si} for $a = 4.0$ mm.

To increase f_{max}, it is intuitive that it is necessary to reduce the lattice a of the unit cell. Considering the printable values of w_{si} and l_{si} for for a smaller $a = 2.5$ mm, the effective permittivity ε_{eff} now varies from 1.46 to 18.54, as seen in Fig. 4.25(a). The maximum frequency for $a < \lambda/10$ goes from 1.99 GHz to 6.23 GHz as can be observed in Fig. 4.25(b).

For $a < \lambda/6$, the maximum frequency varies between 3.32 GHz and 11.08 GHz, as illustrated in Fig. 4.25(c). Therefore, it is possible to conclude that, as expected, it is possible to increase the maximum frequency by decreasing the size a of the cell, but the range of printable effective permittivity decreases since it is limited by the 3D-printer constraints.

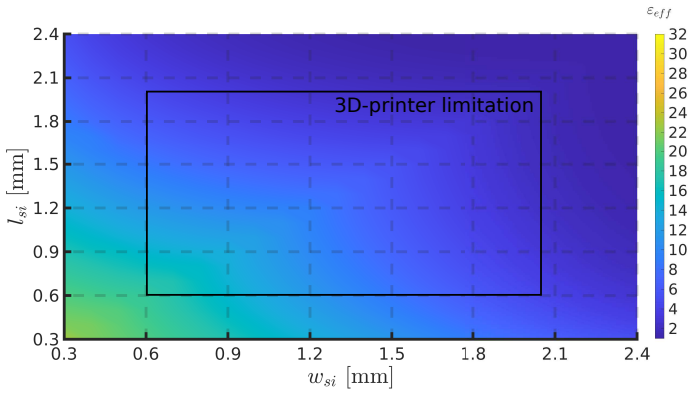

(a) Effective permittivity

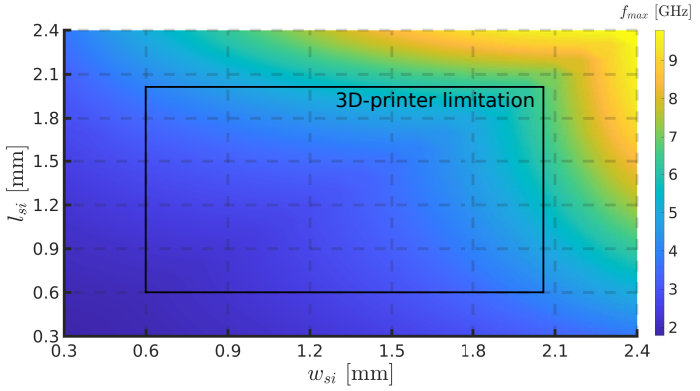

(b) Maximum frequency for $a < \lambda/10$

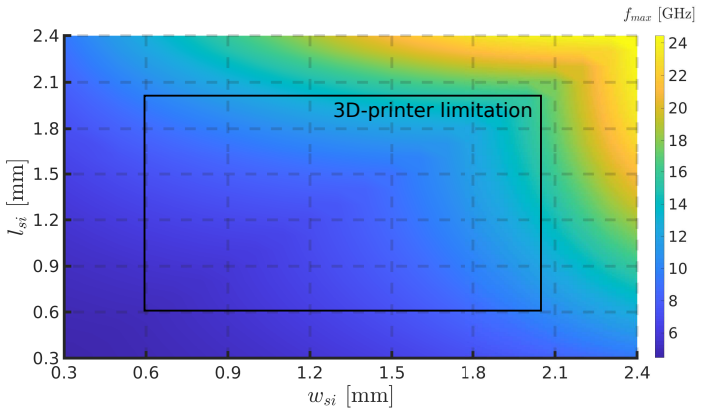

(c) Maximum frequency for $a < \lambda/6$

Figure 4.25: (a) Effective dielectric constant ε_{eff}, (b) maximum frequency f_{max} for $a < \lambda/10$, (c) maximum frequency f_{max} for $a < \lambda/6$ as a function of w_{si} and l_{si} for $a = 2.5$ mm.

4.4 Design of the 3D-Printed Anisotropic Unit Cell

The dual-band CP DRA proposed in Chapter 3 presents an isotropic region as well as two anisotropic regions with high birefringence. To facilitate the transition between these different dielectric regions, the isotropic unit cell proposed in Section 4.3 is slightly modified to have a uniaxial anisotropic behavior. The anisotropic unit cell, shown in Fig. 4.26, exhibits a lack of rotational symmetry. Thus, this structure presents an artificial anisotropy. The effective permittivity of this unit cell is represented by the following tensor $[\varepsilon_x\ 0\ 0;\ 0\ \varepsilon_y\ 0;\ 0\ 0\ \varepsilon_z]$, where $\varepsilon_x = \varepsilon_y \neq \varepsilon_z$. In addition, zirconia ($\varepsilon_r = 32.5$ and $\tan\delta = 1.9 \cdot 10^{-4}$ at 10 GHz) is again assigned as the material of the proposed unit cell.

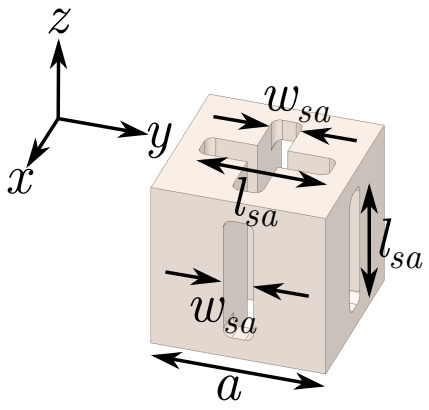

Figure 4.26: Proposed anisotropic unit cell.

To control the effective permittivity and birefringence of the unit cell, the parameters w_{sa} and l_{sa} can be varied, while the lattice $a = 4$ mm and $\varepsilon_r = 32.5$ are fixed. For instance, Fig. 4.27(a) shows the effective permittivity of the unit cell calculated with the S-parameters retrieval method at 1.575 GHz as a function of w_{sa} for $l_{sa} = 2.89$ mm. As w_{sa} increases, the permittivity components decrease, as expected, since the volume of air inside the cube is increasing as well. The permittivity components experience a similar behavior when l_{sa} increases, as can be seen Fig. 4.27(b) for $w_{sa} = 0.76$ mm. Also, the strength of anisotropy, or birefringence, $\Delta\varepsilon = \varepsilon_z - \varepsilon_{y,x}$ is shown as a function of w_{sa} and l_{sa} in Fig. 4.27(c) and 4.27(d), respectively. One can note that $\Delta\varepsilon$ tends to increase as w_{sa} decreases until it reaches its maximum value, which is 13.5 for w_{sa} equal to 0.45 mm. However, the maximum printable birefringence is 13.1 since it would not be possible to print cells with holes with diameter smaller than 0.6 mm. On the other hand, l_{sa} is proven to be proportional to $\Delta\varepsilon$ and its maximum printable value is 15.3 for $l_{sa} = 3.5$ mm.

The dispersion diagram and the irreducible Brillouin zone of the proposed anisotropic cell is shown in Fig. 4.28, where $a = 4$ mm, $w_{sa} = 0.76$ mm, $l_{sa} = 2.89$ mm, and $\varepsilon_r = 32.5$. One can note that the cutoff frequency defining a homogenous medium is around 3.0 GHz since this is the frequency where the EM band starts to deviate from the light line. So, to retrieve the effective parameters of this periodic structure, it is recommended to work with frequencies below 3 GHz, since, above this frequency, the unit cells start to resonate by themselves and some unusual and complex effects can appear.

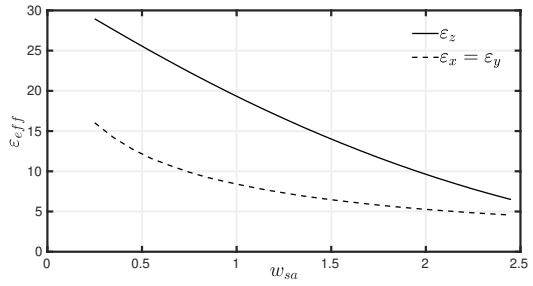

(a) for $l_{sa} = 2.89$ mm

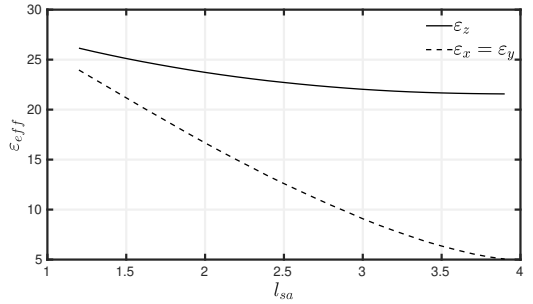

(b) for $w_{sa} = 0.76$ mm

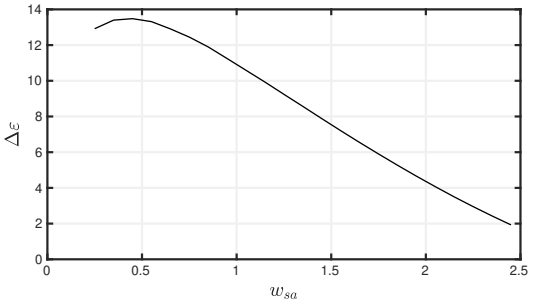

(c) for $l_{sa} = 2.89$ mm

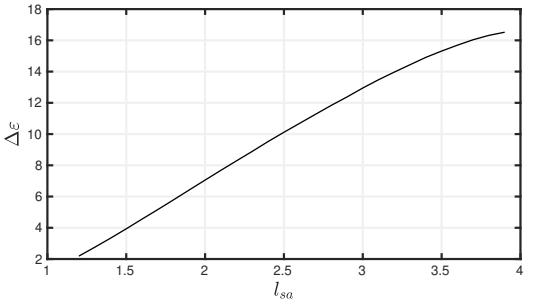

(d) for $w_{sa} = 0.76$ mm

Figure 4.27: Effective dielectric constant ε_{eff} as a function of (a) w_{sa} and (b) l_{sa} as well as the birefrigence $\Delta\varepsilon$ for different values of (c) w_{sa} and (d) l_{sa} computed with the S-parameters retrieval method at 1.575 GHz.

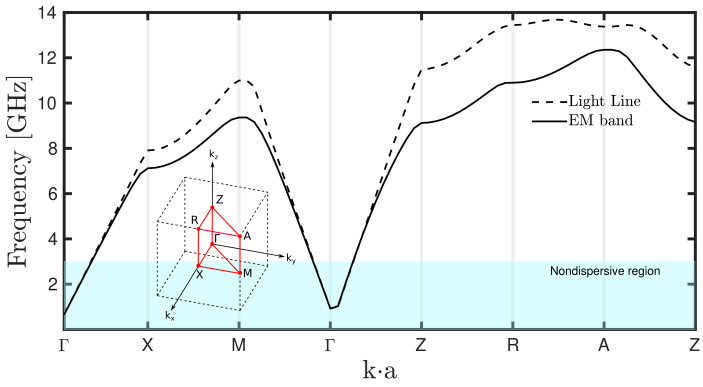

Figure 4.28: Dispersion diagram of the proposed uniaxial anisotropic unit cell and its irreducible Brillouin zone.

Therefore, the proposed anisotropic unit cell allows the possibility of having large birefringence, which is necessary to design the proposed dual-band CP DRA developed in Chapter 3. Also, its shape facilitates the transition between the isotropic and anisotropic of the DRA.

4.5 Conclusion

Even though dielectric resonator antennas have several advantages when compared to some other traditional antennas, their usage was still limited due to the complicated fabrication process in terms of materials and complex shapes. The establishment of 3D-printing technology has the potential to overcome this issue, which can be combined with periodic structure theory to allow the realization of artificial isotropic, anisotropic, homogeneous, inhomogeneous, dispersive, and/or nondispersive media, for instance. In other words, from a single printing material and properly choosing the unit cell that will form this periodic medium, different media with different effective dielectric properties can be achieved.

In this chapter, it has been proposed two different types of electrically-small unit cells, which are made out of zirconia ($\varepsilon_r = 32.5$ and $\tan\delta = 1.9 \cdot 10^{-14}$ GHz) that is a ceramic material with high performance. The unit cells are electrically small at the L5 and L1 bands, thus, avoiding the dispersion effects. First, an isotropic cell is proposed, which has rotational symmetry along the x-, y- and z-axes and, then, presents an isotropic behavior. The value of effective relative permittivity ε_{eff} of the cell is controlled by the relation between the amount of air and zirconia in it.

Three different methods are used to investigate the isotropic unit cell which are the S-parameters retrieval method, dispersion diagram, and Eigenmode analysis with a DR. It is demonstrated that for electrically-small cells both S-parameters retrieval method and dispersion diagram can be used to compute the effective permittivity. On the other hand, using an Eigenmode analysis, it is shown that the dispersion diagram is more accurate for electrically-large unit cells that can be used to design dielectric resonators, since this method takes

into account the dispersion, as its name suggests, which is a limitation of the S-parameters retrieval method.

A unit cell with a uniaxial anisotropic behavior is proposed as well. The anisotropy is achieved due to the lack of its rotational symmetry and its design allows the realization of an effective medium with an effective permittivity of $[\varepsilon_x\ 0\ 0;\ 0\ \varepsilon_y\ 0;\ 0\ 0\ \varepsilon_z]$, where $\varepsilon_x = \varepsilon_y \neq \varepsilon_z$, using the zirconia, which is an isotropic material. For a unit cell with lattice of 4 mm and considering the restrictions of the 3D-printer, birefringence, *i.e.* $\Delta\varepsilon = \mid \varepsilon_z - \varepsilon_{x,y} \mid$, up to 15.7 can be achieved. Also, the effective permittivity components can be easily adjusted by controlling the dimensions of the proposed unit cell.

As in Chapter 3 the permittivity of the isotropic and anisotropic regions were directly assigned on Ansys HFSS, the unit cells proposed in this chapter allow the realization of the proposed inhomogeneous and anisotropic DRA with the use of 3D-printing technology. Therefore, in the next chapter, the unit cells and the proposed DRA will be combined to manufacture the proposed antenna.

Chapter 5

3D-Printed Dual-Band Circularly-Polarized DRA

Contents

In Chapter 3, a dual-band circular-polarized dielectric resonator antenna (DRA) has been proposed. This design relies on the local control of the dielectric properties of the resonator, which is made up of an isotropic and two anisotropic regions. So far in this thesis, the properties of these dielectric regions have directly been assigned on Ansys HFSS. To manufacture this antenna, it is therefore necessary to use the unit cells proposed in Chapter 4 to create artificial isotropic and anisotropic media with the needed permittivities. In this chapter, isotropic and anisotropic unit cells are first designed for the proposed dual-band circularly-polarized DRA. In Section 5.1, the simulation results of the antenna used in Chapter 3 and the antenna made out of subwavelength unit cells are presented. In Section 5.2, the manufacturing process is described. Finally, in Section 5.3, the measured results are presented.

5.1 3D-Printed Model

Previously, the local control of the dielectric properties of a resonator is used to conceive a dual-band CP antenna. However, these properties were directly assigned on Ansys HFSS. To manufacture this antenna, it is not sure that these dielectrics will be available on market, which limits the degree of freedom to design this type of structure. Nevertheless, subwavelength unit cells can be used to do so.

In Chapter 3, the proposed antenna presented an isotropic dielectric with relative permittivity $\varepsilon_{\mathrm{ri}}$ equal to 10, and an anisotropic one represented by the following tensor:

$$\varepsilon_{\mathrm{ra}} = \begin{pmatrix} \varepsilon_{\mathrm{x}} & 0 & 0 \\ 0 & \varepsilon_{\mathrm{y}} & 0 \\ 0 & 0 & \varepsilon_{\mathrm{z}} \end{pmatrix} = \begin{pmatrix} 10 & 0 & 0 \\ 0 & 10 & 0 \\ 0 & 0 & 22.1 \end{pmatrix}. \tag{5.1}$$

To create artificial media with these dielectric properties, the isotropic and anisotropic subwavelength unit cells proposed in Section 4.3 and 4.4 are used, respectively. These elementary cells are recalled in Fig. 5.1. It is important to point out that both cells are made out of zirconia, which has $\varepsilon_{\mathrm{r}} = 32.5$ and $\tan\delta = 1.9 \cdot 10^{-4}$ at 10 GHz.

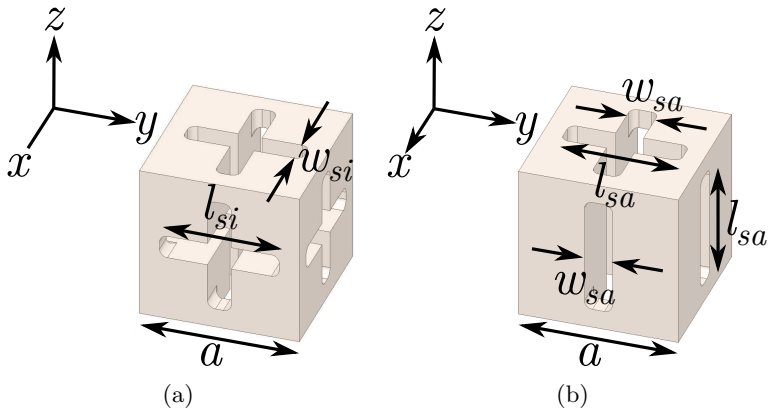

Figure 5.1: (a) Isotropic and (b) anisotropic subwavelength unit cells.

The proposed unit cell shown in Fig. 5.1(a) has symmetry along the x-, y-, and z-axes, presenting isotropic behavior. After optimization, we find w_{si} and l_{si} equal to 0.6 mm and 2.99 mm, respectively. Considering these dimensions, the curve of effective permittivity over frequency can be observed in Fig. 5.2 as calculated using the S-parameters retrieval method. One can note that effective permittivity is equal to 10.08 and 10.06 around 1.17 GHz and 1.57 GHz, respectively. This difference is only about 0.2% because the unit cell is only a fraction of the wavelength, *i.e.* $a \simeq \frac{\lambda}{15}$ at the L1 band.

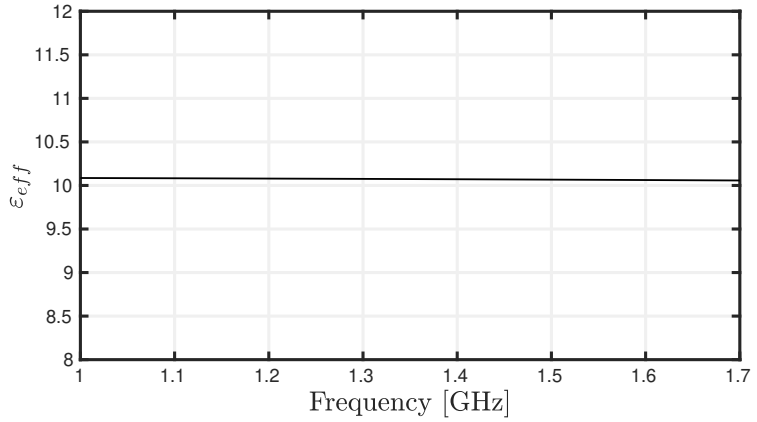

Figure 5.2: Effective dielectric constant over frequency of the isotropic unit cell.

For the proposed uniaxial anisotropic unit cell shown in Fig. 5.1(b) and considering $a = 4$ mm, $w_{\mathrm{sa}} = 0.76$ mm, and $l_{\mathrm{sa}} = 2.89$ mm, the permittivity as a function of the frequency is presented in Fig. 5.3. It is possible to observe that at 1.17 GHz, $\varepsilon_{\mathrm{x}} = \varepsilon_{\mathrm{y}} = 9.9$ and $\varepsilon_{\mathrm{z}} = 22.2$, and at 1.57 GHz, $\varepsilon_{\mathrm{x}} = \varepsilon_{\mathrm{y}} = 9.8$ and $\varepsilon_{\mathrm{z}} = 22.2$. Moreover, at the L1 band and considering the highest permittivity component, the lattice a of the unit cell is equivalent to around $\frac{\lambda}{10}$.

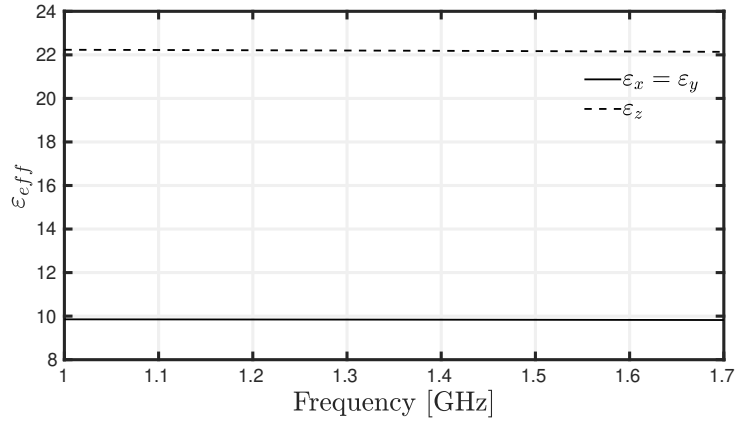

Figure 5.3: Effective dielectric constant over frequency of the anisotropic unit cell.

Considering the unit cells with the aforementioned dimensions, the 3D-printed model of the DRA is designed, as can be observed in Fig. 5.4. The proposed subwavelength unit cells replace the isotropic and anisotropic regions of the solid model. The overall dimensions of both models are the same, *i.e.* $w = 45$ mm, $b = 67$ mm, $w_{\mathrm{a}} = 10.5$ mm, $l_{\mathrm{a}} = 31$ mm, $b_{\mathrm{a}} = 47$ mm, and $w_{\mathrm{g}} = 135$ mm. Moreover, the width w_{s} and length l_{s} of the slot are 4.16 mm and 57.4 mm. It is coupled to a 50-Ω microstrip line with length l_{l} of 163.9 mm and width w_{l} of 3.86 mm. They are separated by a Taconic RF-301 substrate with thickness h_{s} equal to 1.524 mm (see Fig. 3.11 for more details about the feeding network).

Taking into account the aforementioned parameters, the magnitude of the simulated reflection coefficient $|S_{11}|$ of the 3D-printed and solid models of the proposed DRA is shown in Fig. 5.5. One can note that the simulated impedance bandwidths ($|S_{11}| < 10$ dB) of the solid model are 17.96% (1065.0 MHz - 1275.1 MHz) and 10.62% (1513.8 MHz - 1668.4 MHz) at the L5 and L1 bands, respectively. On the other hand, for the 3D printed model, the impedance bandwidths are 15.56% (1067.5 MHz - 1247.6 MHz) and 9.90% (1511.0 MHz - 1668.4 MHz). Therefore, even with a slight difference in the bandwidth between both models, the curves present a very similar behavior, and the L5 and L1 bands are still covered in both cases.

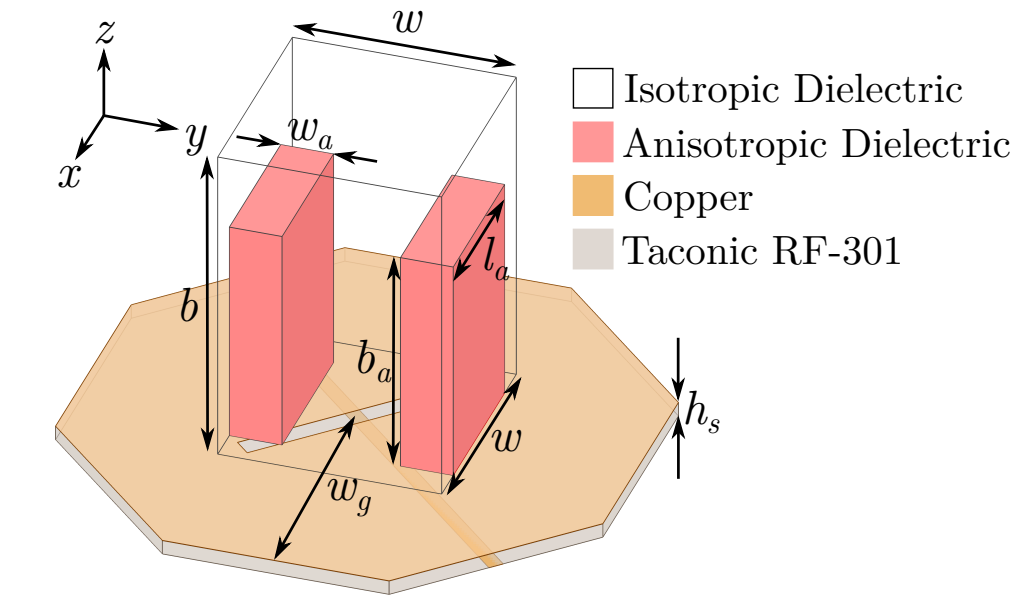

(a) Solid model

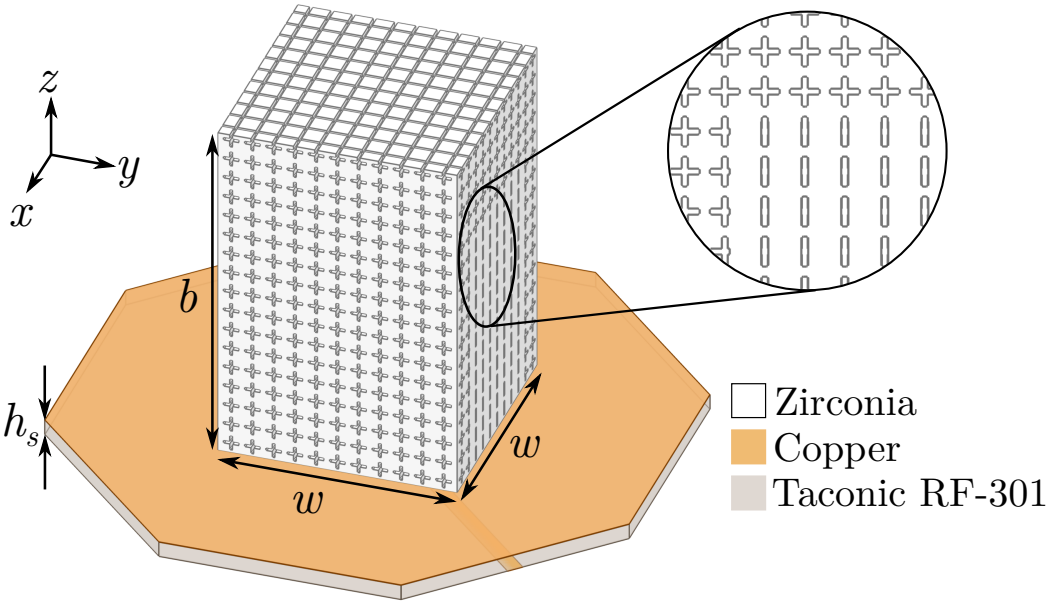

(b) 3D-printed model

Figure 5.4: Perspective view of the (a) solid and (b) 3D-printed models of the proposed dual-band CP DRA.

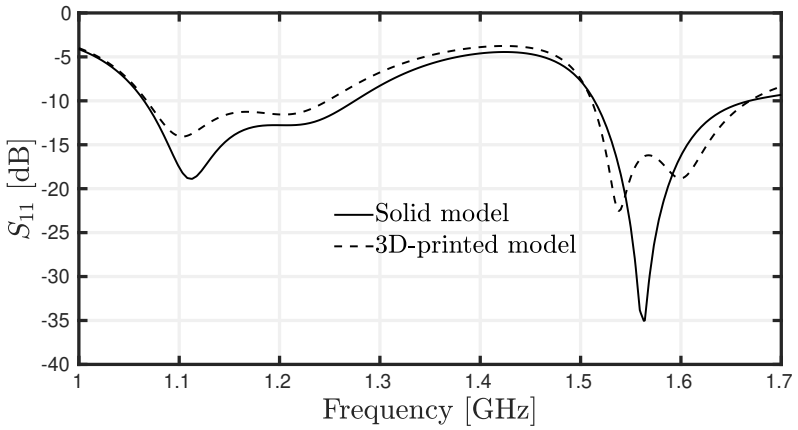

Figure 5.5: Simulated reflection coefficient of the solid and 3D-printed models of the proposed dual-band CP DRA.

Figure 5.6 presents the axial ratio (AR) of the proposed antenna at the boresight direction ($\theta = 0°$ and $\phi = 0°$). The simulated 3-dB AR bandwidths of the solid model are 5.00% (1140.3 MHz - 1198.8 MHz) and 1.46% (1562.8 MHz - 1585.7 MHz), covering both L5 and L1 bands. For the 3D-printed model, the 3-dB AR bandwidths are 4.84% (1121.9 MHz - 1177.5 MHz) and 1.42% (1552.9 MHz - 1575.1 MHz). One can note a downward frequency shift for the 3D-printed model in comparison to the solid one and, to fix it, it is necessary to re-optimize the 3D-printed model. However, the simulation of this model requires high-computational effort, which does not allows computational optimization.

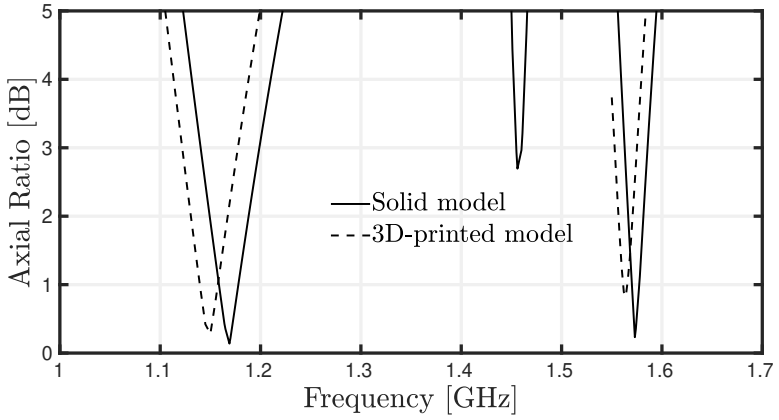

Figure 5.6: Simulated axial ratio of the solid and 3D-printed models of the proposed dual-band CP DRA.

The left- and right-handed components of the gain pattern, in dBi, at the L5 and L1 bands, are shown in Fig. 5.7 for both 3D-printed and solid models in $\phi = 0°$ and $\phi = 90°$ planes. One can note that the patterns are similar at both frequencies. Also, broadside radiation patterns are observed, as expected for the radiating modes at issue. Both models are observed to present right-hand circular polarization at the L5 and L1 bands.

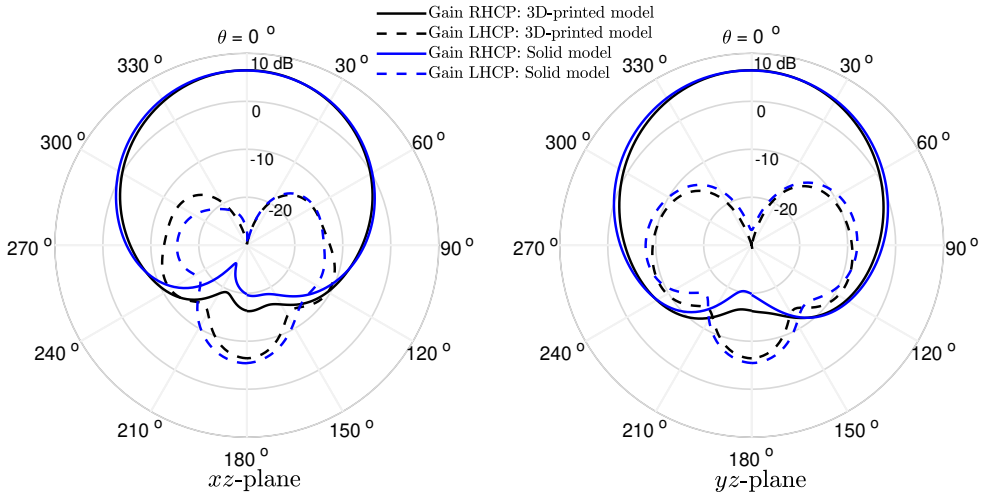

(a) L5 band

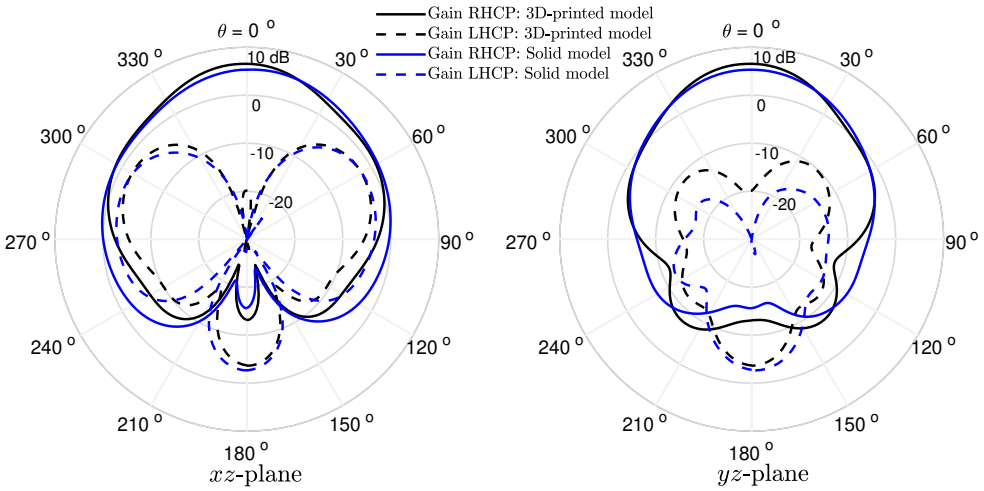

(b) L1 band

Figure 5.7: Simulated gain patterns at (a) L5 and (b) L1 bands for solid and 3D-printed models of the proposed dual-band CP DRA.

5.2 Manufacturing Process

The 3DCeram's C900 printer is used to manufacture the proposed dual-band CP DRA. It employs a stereolithography laser during the fabrication process. Like any manufacturing process, some constraints must be considered and the main ones are: the zirconia walls must be thicker than 1 mm and the diameter of the holes must be at least 0.6 mm. Even though the constraints were respected, these types of unit cells were printed for the first time using a technology not completely established and, despite several attempts, the DRA broke into small pieces during the sintering, as can be seen in Fig. 5.8.

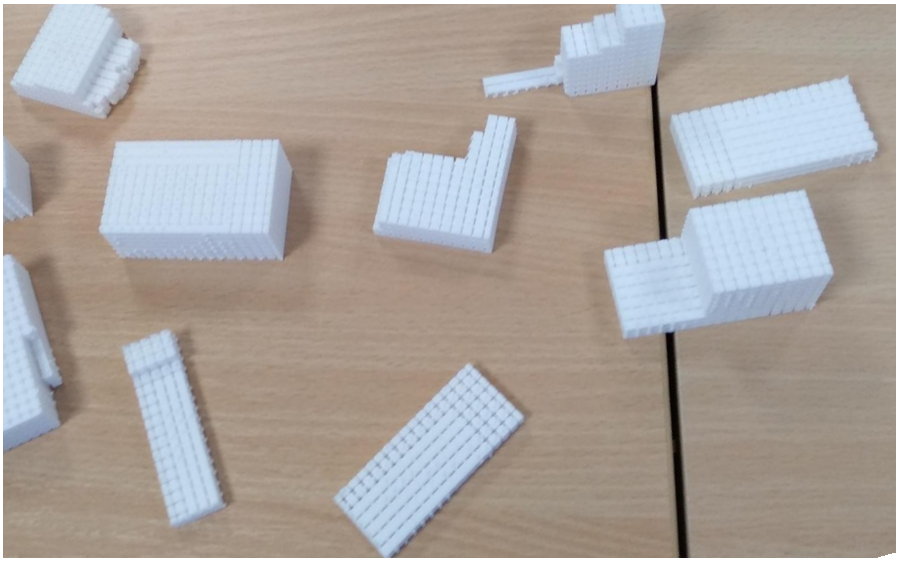

Figure 5.8: Broken pieces of the proposed 3D-printed DRA.

To increase the chance of 3D printing the proposed antenna, 3DCeram suggested reducing the volume of the antenna, reducing l_{si}, and increasing w_{si}. Regarding the volume issue, the DRA has to be re-designed to operate at higher frequencies. To properly choose the frequencies, it is necessary to take into account the dispersion of the unit cells (see Fig. 4.15 and 4.28) and the frequency range that it would be possible to measure in the anechoic chamber available in our facilities. Also, this DRA could be designed for different frequencies by controlling mainly its width w, height b, and permittivity ε_r of the DRA, as can be seen in Fig. 5.9. For this analysis, an isotropic, homogeneous, and rectangular DRA with a square base and $w = 51$ mm and $\varepsilon_{\mathrm{r}} = 10$ is considered while b varies, for instance. From this plot, it is possible to realize that the separation between fundamental $\mathrm{TE}_{111}^{x,y}$ and higher-order $\mathrm{TE}_{113}^{x,y}$ modes is highly sensitive to b, which shows the possibility of designing this antenna at different frequency bands. Regarding the isotropic unit cell, l_{si} and w_{si} can be adjusted to the desired permittivity by controlling the filling ratio δ_{i}, which is discussed in Section 4.3.

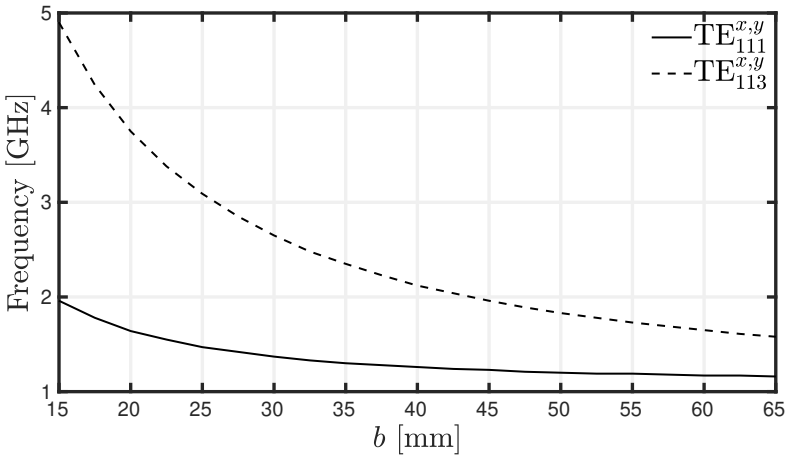

Figure 5.9: Resonance frequencies of the $TE^{x,y}_{111}$ and $TE^{x,y}_{113}$ modes as a function of the height b of the DRA.

Taking all of the aforementioned issues into consideration, the proposed DRA has been designed again taking as reference the L1 (1565.19 MHz - 1585.65 MHz) and up-link of the TT&C (2025 MHz - 2110 MHz) bands. The dimensions of this new antenna are shown in Table 5.1 and compared to the DRA designed to operate for the L5 and L1 bands. The new design has an overall volume of 59.41 cm^3, which is 56.21% smaller than the L5 and L1 bands antenna, in which its volume is 135.68 cm^3. Therefore, a relevant size reduction is achieved by simply increasing the operating frequencies of the DRA.

Bands	w	b	w_a	b_a	l_a	l_{si}	w_{si}	l_{sa}	w_{sa}	ε_{ri}	ε_z
L1 & TT&C	33.8 mm	52.0 mm	10.7 mm	39.2 mm	17.6 mm	2.52 mm	1.08 mm	2.72 mm	0.91 mm	10	20.5
L5 & L1	45.0 mm	67.0 mm	11.5 mm	47.0 mm	31.0 mm	2.99 mm	0.6 mm	2.89 mm	0.76 mm	10	22.2

Table 5.1: Parameters of the proposed DRAs designed for the L1 and up-link TT&C bands and for the L5 and L1 bands, where $\varepsilon_{ri} = \varepsilon_x = \varepsilon_y$.

In Table 5.1, it is possible to note that the tensor of permittivity of the anisotropic unit cell changed with the new design, *i.e.* $\varepsilon_{\mathrm{x}} = \varepsilon_{\mathrm{y}} = 10$ and $\varepsilon_{\mathrm{z}} = 20.5$. Using the concepts discussed in Section 4.4, the dimensions of the anisotropic cell are $a = 4$ mm, $w_{\mathrm{sa}} = 0.91$ mm, and $l_{\mathrm{sa}} = 2.72$ mm. Moreover, to increase our chance of successfully 3D-print the proposed DRA, the isotropic cell is re-designed also, where $a = 4$ mm, $w_{\mathrm{si}} = 1.08$ mm, and $l_{\mathrm{si}} = 2.52$ mm. Note that w_{si} increases and l_{si} decreases when compared to the first design. The curves of effective permittivity are presented in Fig. 5.10 for the isotropic and anisotropic cells considering the aforementioned parameters and the desired permittivity values are achieved. Also, the electric size of the isotropic and anisotropic at the up-link of the TT&C band is equivalent to $\lambda/11.5$ and $\lambda/8.0$, respectively.

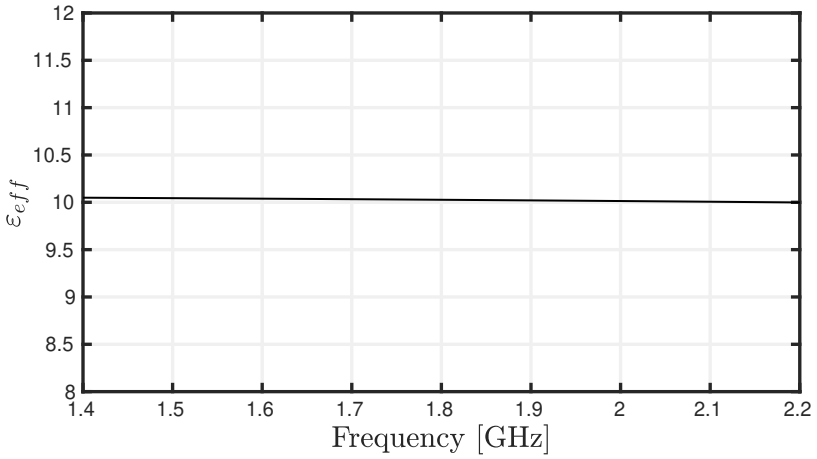

(a) Isotropic unit cell

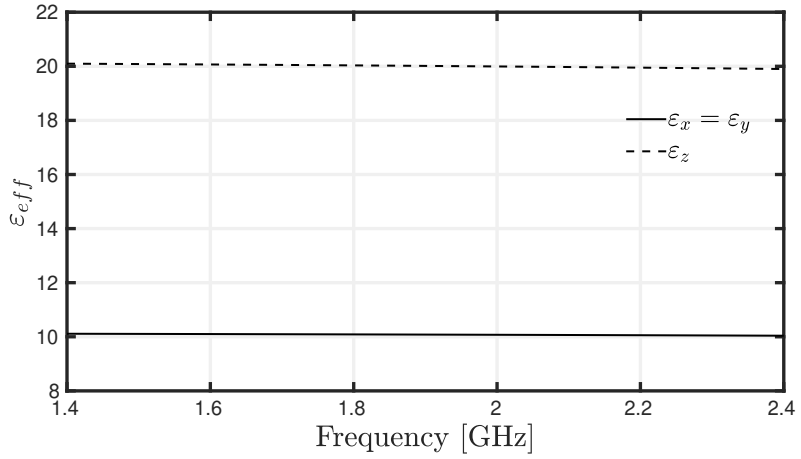

(b) Anisotropic unit cell

Figure 5.10: Effective permittivity of the (a) isotropic and (b) anisotropic subwavelength unit cells.

After these modifications and some effort in the manufacturing process, the inhomogeneous and anisotropic DRA has finally been successfully 3D-printed, as can be observed in Fig. 5.11(a). However, it is possible to identify a small default on one of the sides of the dielectric resonator, namely in the isotropic region as shown in Fig. 5.11(b). Besides, the final dimensions of the DR are slightly lower than what was expected with $w = 32.9$ mm and $b = 51.5$ mm, *i.e.* a 2.6% and 1% error, respectively. Even with this default, the antenna has been measured and the results are presented in the following section.

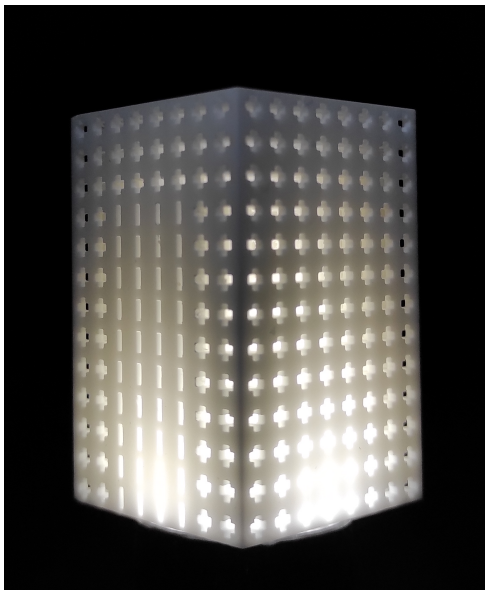

(a)

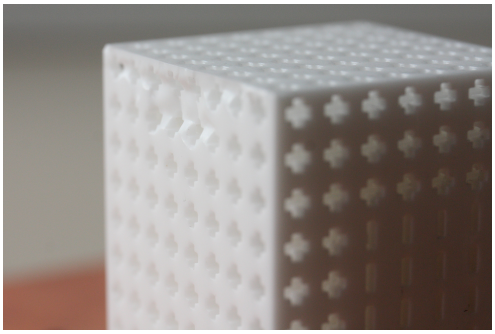

(b)

Figure 5.11: Pictures of the 3D-printed inhomogeneous and anisotropic DRA.

5.3 Measurements and Discussion

The 3D-printed DRA is mounted over a ground plane and an SMA connector is used to connect the antenna to a 50-Ω coaxial cable, as can be observed in Fig. 5.12. At first, the magnitude of the reflection coefficient $|S_{11}|$ in dB has been measured with a Copper Mountain S5065 Vector Network Analyzer (VNA), and the measured and simulated results are presented in Fig. 5.13. For the simulated result, the impedance bandwidth ($|S_{11}| < 10$ dB) are 22.42% (1.37 GHz - 1.72 GHz) and 8.27% (1.97 GHz - 2.14 GHz). For the measured results, the impedance bandwidth is 20.95% (1.41 GHz - 1.74 GHz) and 8.57% (2.01 GHz - 2.19 GHz). One can note an upward frequency shift for the measurements of around 2%, which may certainly be due to the manufacturing tolerances since some defaults are noted and the width and height of the 3D-printed antenna are 2.6% and 1% smaller than the expected, respectivelly.

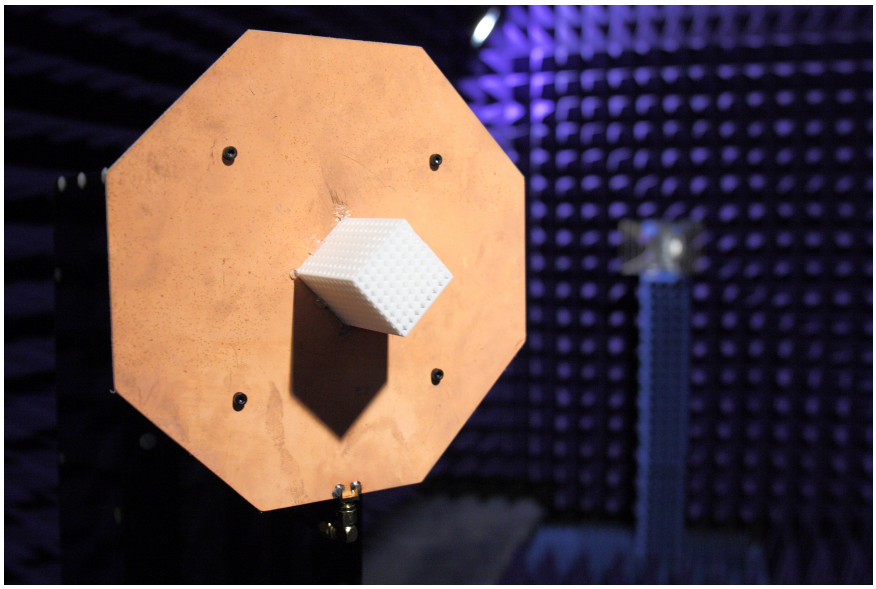

Figure 5.12: Perspective view of the 3D-printed antenna mounted over a ground plane.

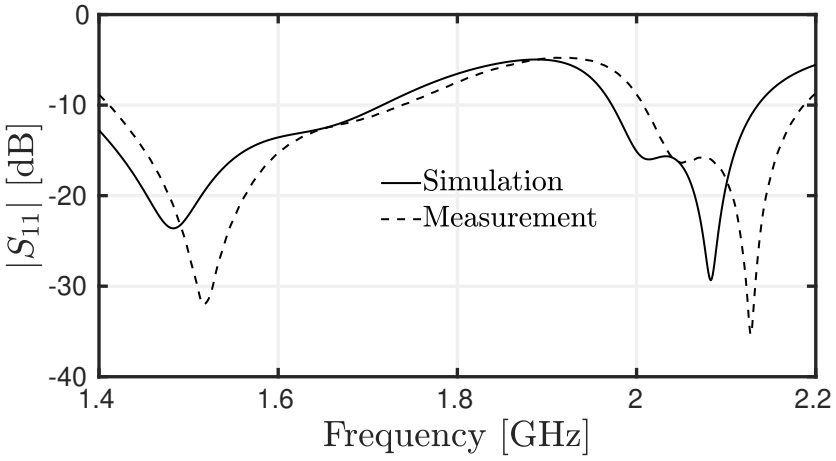

Figure 5.13: Measured and simulated reflection coefficient of the proposed inhomogenenous and anisotropic DRA.

In this work, the axial ratio and radiation patterns are measured in a SIEPEL anechoic chamber with a Rohde & Schwarz ZVL13 VNA at ISAE-SUPAERO. Considering this setup, Fig. 5.14 shows simulated and measured axial ratio as a function of the frequency at the boresight direction, *i.e.* for $\phi = 0°$ and $\theta = 0°$. The simulated 3-dB axial ratio (AR) bandwidths are 5.06% (1.54 GHz - 1.62 GHz) and 1.45% (2.05 GHz - 2.08 GHz). For the measured results, the 3-dB axial ratio (AR) bandwidths are 4.31% (1.59 GHz - 1.66 GHz) and 2.38% (2.08 GHz - 2.13 GHz). An upward frequency shift of around 2% of the measured results is observed once again, as expected. Therefore, one can note that even with this slight frequency shift, the antenna presents dual band and circular polarization, which is the goal of the proposed design.

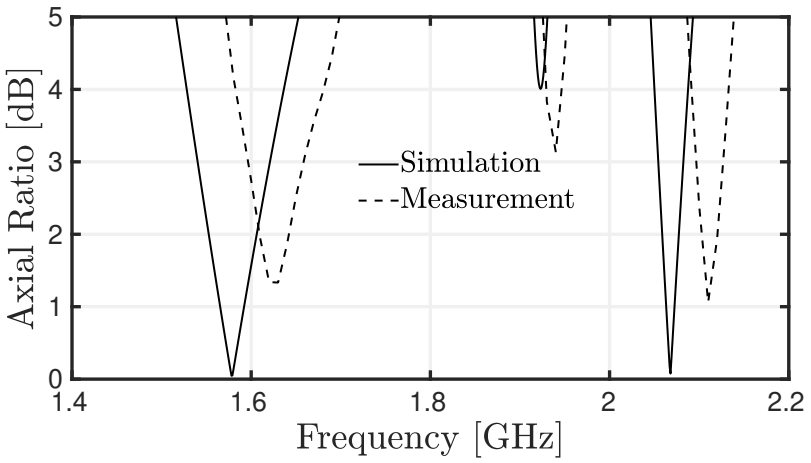

Figure 5.14: Measured and simulated axial of the proposed inhomogenenous and anisotropic DRA at the boresight direction ($\phi = 0°$ and $\theta = 0°$).

The simulated and measured left- and right-handed components of the gain pattern in dBi and calculated at the frequency of minimum axial ratio are shown in Fig. 5.15. At both bands and for both simulation and measurements, it is possible to observe that the proposed antenna presents broadside radiation patterns, as expected for the $\mathrm{TE}^{x}_{\delta 11}$, $\mathrm{TE}^{y}_{1\delta 1}$, $\mathrm{TE}^{x}_{\delta 13}$, and $\mathrm{TE}^{y}_{1\delta 3}$ modes. Also, one can note that the antenna presents right-handed circular polarization and both models present similar radiation patterns.

Figure 5.16 presents the simulated and measured axial ratio as a function of θ at $\phi = 0°$ and $\phi = 90°$ at the lower and upper bands. At the lower band, the simulated axial ratio is below 3 dB for $-49.5° \leq \theta \leq 47.3°$ and $-39.9° \leq \theta \leq 39.8°$ at $\phi = 0°$ and $\phi = 90°$, respectively. By contrast, at the upper band, the simulated axial ratio is below 3 dB for $-21.5° \leq \theta \leq 21.7°$ and $-35.9° \leq \theta \leq 29.4°$ at $\phi = 0°$ and $\phi = 90°$, respectively. For the measurements, the circular polarization happens at the lower band for $-56.6° \leq \theta \leq 48.4°$ at $\phi = 0°$ and for $-30.6° \leq \theta \leq 34.6°$ at $\phi = 90°$. At the upper band, the measured 3-dB axial ratio covers $-26.0° \leq \theta \leq 31.5°$ and $-35.6° \leq \theta \leq 28.4°$ at $\phi = 0°$ and $\phi = 90°$, respectively.

Figure 5.17 shows the measured and simulated realized gain in dBi at boresight direction, *i.e.* $\phi = 0°$ and $\theta = 0°$. At the L1 band, the maximum realized gains are 7.02 dBi and 6.45 dBi for the simulation and measurement, respectively. At the up-link TT&C band, the maximum realized gain in simulation is 8.27 dBi and, for the measurement, is 7.30 dBi. Therefore, one can note that the measured realized gains are slightly lower than simulated ones.

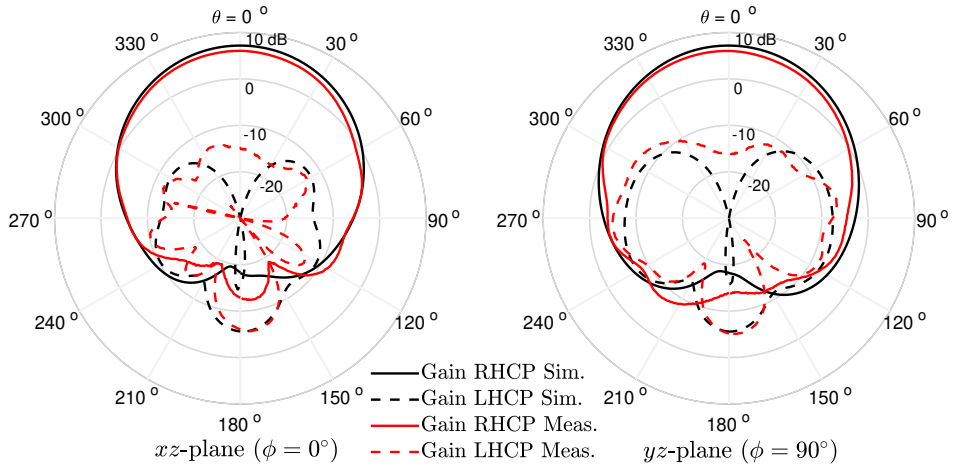

(a) L1 band

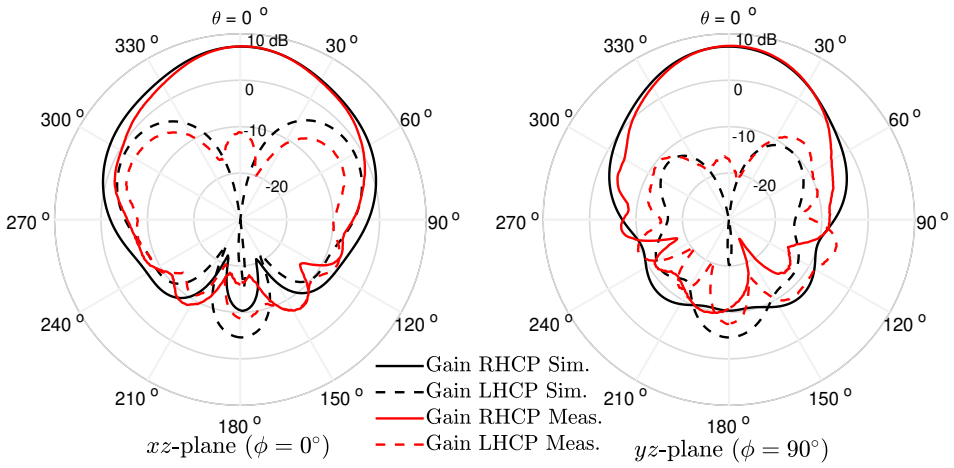

(b) TT&C band

Figure 5.15: Simulated and measured radiation patterns at (a) L1 and (b) TT&C bands of the proposed dual-band circularly-polarized DRA.

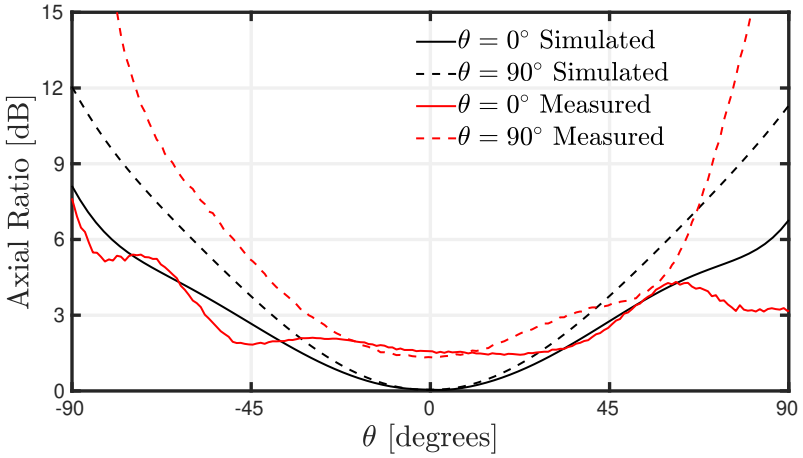

(a) Lower band

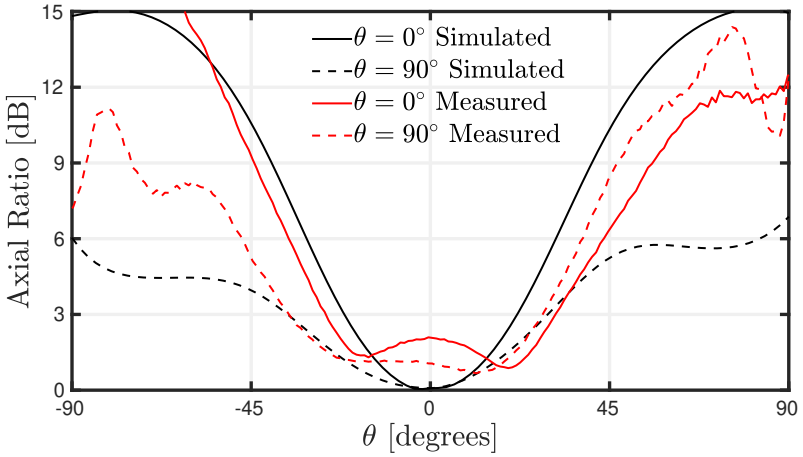

(b) Upper band

Figure 5.16: Simulated and measured axial ratio as function of θ at the (a) L1 and (b) TT&C bands for the proposed dual-band circularly-polarized DRA.

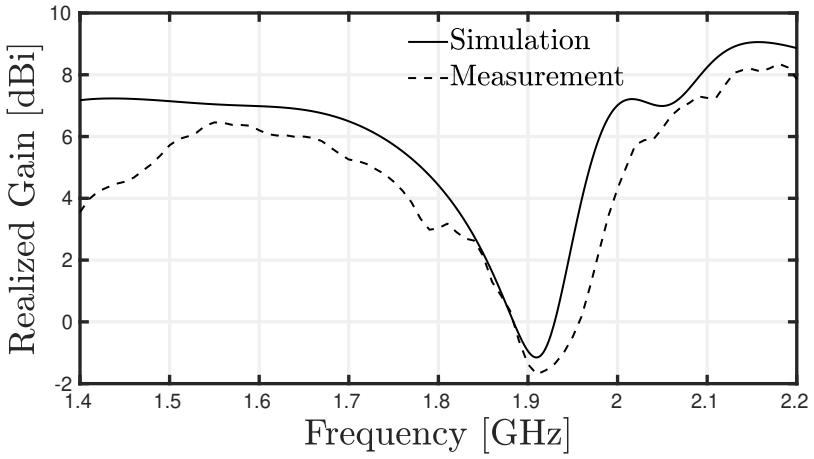

Figure 5.17: Simulated and measured realized gain of the proposed dual-band circularly-polarized DRA at the boresight direction ($\phi = 0°$ and $\theta = 0°$).

Finally, with the measurements, it is observed that the 3D-printed inhomogeneous and anisotropic DRA presents circular polarization with a dual-band operation, as expected. Table 5.2 summarizes the main results obtained from the measurements and simulations. The measured results present a frequency shift of around 2% in the $|S_{11}|$ and axial ratio compared to the simulated ones. However, we consider this difference acceptable since the antenna presents a visible default and size difference due to the manufacturing process.

	Simulation		**Measurement**	
	Lower band	**Upper band**	**Lower band**	**Upper band**
Impedance bandwidth	22.42%	8.27%	20.95%	8.57%
3-dB AR bandwidth	5.06%	1.45%	4.31%	2.38%
3-dB AR beamwidth for $\phi = 0°$	96.8°	43.2°	105°	57.5°
3-dB AR beamwidth for $\phi = 90°$	79.7°	65.3°	65.2°	64°
Maximum realized gain	7.02 dBi	8.27 dBi	6.45 dBi	7.30 dBi

Table 5.2: Simulated and measured results of the proposed dual-band circularly polarized DRA.

5.4 Conclusion

In this chapter, isotropic and anisotropic unit cells are used to realize the proposed dual-band CP dielectric resonator antenna proposed in Chapter 3. Previously, the dielectric properties of this antenna were directly assigned on Ansys HFSS for simulations. Here, the needed dielectric properties are achieved due to the use of 3D-printable subwavelength unit cells and the main results are presented and discussed.

Initially, the dual-band CP DRA has been designed to operate at the L5 (1166.22 MHz - 1186.68 MHz) and L1 (1565.19 MHz - 1585.65 MHz) bands of the GNSS. Nevertheless, pro-

totypes of this antenna broke during the 3D printing. After some trials, 3DCeram concluded that the antenna was too big and fragile. To overcome this problem, they suggest reducing the size of the antenna and changing some dimensions of the isotropic unit cell.

The demanded modifications of the isotropic unit cell are easily done due to the development in Section 4.3. To reduce the volume, the operating frequency of the prototype has been increased to operate at the L1 (1565.19 MHz - 1585.65 MHz) and up-link of the TT&C (2025 MHz - 2110 MHz) bands with a volume reduction of 56.21%. Finally, the dual-band CP DRA has been successfully 3D-printed.

Measurements have been performed and the results are compared with the simulated ones. A good agreement between the results is observed. Nevertheless, in the measured $|S_{11}|$ and axial ratio, an upward frequency shift of around 2% is observed. This shift is attributed to some visible defaults and size difference in the prototype due to the manufacturing tolerances. These problems during the manufacturing seem to be related to the fact that the proposed antenna is inhomogeneous, which leads to different coefficients of thermal expansion in this object during the sintering process. However, these types of issues are normal since the process of 3D-printing ceramics is not completely established yet.

One of the main goals of this thesis is to demonstrate the possibility of controlling the dielectric properties in an electrically-small resonator. With the measured results, we demonstrated that it is possible to do so. This is done by 3D-printing an inhomogeneous and anisotropic DRA with dual-band and circular polarization. In the next chapter, we propose an extension of this design to a third band.

Chapter 6

Inhomogeneous and Anisotropic Triple-Band DRA

Contents

In the previous chapters, a dual-band circularly-polarized dielectric resonator antenna is presented, which has broadside radiation patterns at both bands. In this chapter, the introduction of a third band with an omnidirectional radiation pattern to the previously proposed DRA is presented. In Section 6.1, the principle of operation of this antenna is described. The presence of the quasi-TM_{001} mode is discussed and how its resonance frequency can be controlled without affecting the modes employed at the GNSS band. In Section 6.2, the full antenna with its feeding system and a finite ground plane is considered, and results such as reflection coefficient, axial ratio, and radiation patterns are presented and discussed. In Section 6.3, the feeding method used to excite the $TE^{x}_{\delta 11}$, $TE^{y}_{1\delta 1}$, $TE^{x}_{\delta 13}$, $TE^{y}_{1\delta 3}$, and quasi-TM_{001} modes is studied in more detail.

6.1 Principle of Operation

A great number of communication systems use the ISM band (2.4 GHz - 2.5 GHz) for short-range links. Thus, in addition to a dual-band and circular polarization operation at the GNSS, it would be interesting to add to the antenna proposed in Chapter 3 a third band with an omnidirectional radiation pattern.

From [87], it is known that the quasi-TM_{001} mode can be excited in isotropic and homogenous rectangular DRAs with a square base. This mode results from the combination of the $TE^{x}_{\delta 21}$ and $TE^{y}_{2\delta 1}$ modes when they are excited at the same frequency. The quasi-TM_{001} mode radiates as a vertical electric dipole and it could be excited by a probe placed at the center of the DRA. However, due to the lack of symmetry of the inhomogeneous dielectric

used for the dual-band DRA proposed in Chapter 3, it is necessary to verify whether this mode exists in this structure.

As a starting point, the dual-band DRA proposed in Chapter 3 is considered to investigate the existence of the quasi-TM_{001} mode. The DR is placed over an infinite ground plane without any sources, as can be seen in Fig. 6.1. An Eigenmode analysis is then performed using Ansys HFSS. The parameters optimized in Section 3.1 are considered for the Eigenmode analysis, where $\varepsilon_{ri} = \varepsilon_x = \varepsilon_y = 10$, $b = 75.0$ mm, $w = 41.5$ mm, $b_a = 42.0$ mm, $l_a = 29.0$ mm, and $w_a = 10.5$ mm. Nevertheless, instead of using at first the optimized value of $\varepsilon_z = 25.1$, its initial value is defined as 10, *i.e.* the isotropic and homogeneous case, where the presence of the quasi-TM_{001} is already proven [87]. Considering these parameters, the quasi-TM_{001} mode is found at 2.52 GHz as identified in Fig. 6.2 by its dipole-like field distribution.

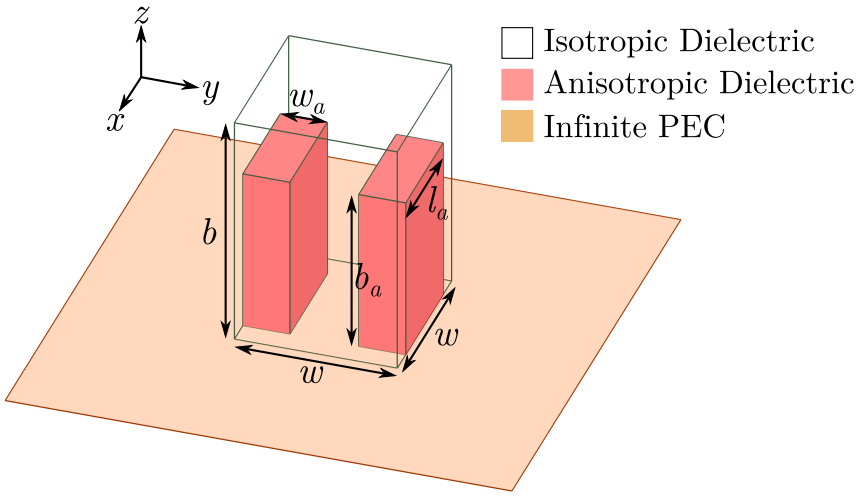

Figure 6.1: Perspective view of the proposed dual-band DRA over an infinite ground plane.

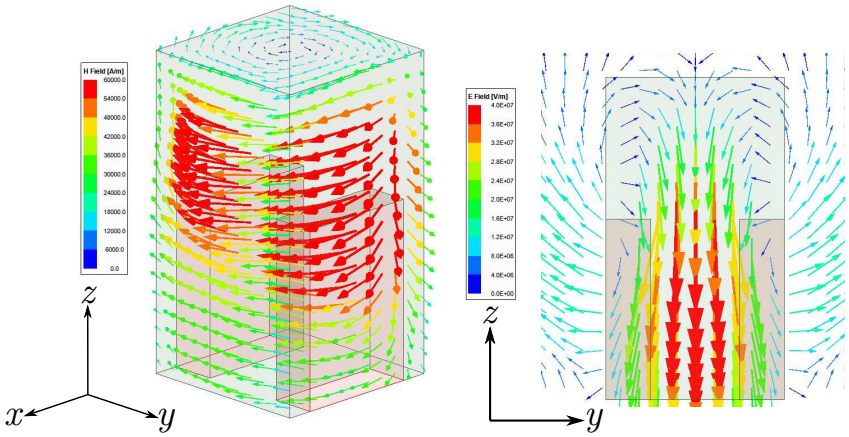

(a) Magnetic field (b) Electric field

Figure 6.2: (a) Magnetic and (b) electric field distributions of the quasi-TM_{001} mode assuming a homogeneous and isotropic square-base rectangular dielectric resonator.

Now that the resonance frequency of the quasi-TM_{001} mode for the isotropic and homogeneous scenario has been identified, one can track this mode when varying ε_z to verify its existence. Figure 6.3 shows the resonance frequency and Q-factor of the quasi-TM_{001} mode as a function of ε_z. This mode is observed for all values ε_z considered in this analysis, *i.e.* from 6 to 28. It means that, even with the lack of symmetry of the dielectric properties of the DR, this mode can be excited. Also, for the initial value of $\varepsilon_z = 25.1$, the quasi-TM_{001} mode now resonates at 2.32 GHz with a Q-factor of 7.42.

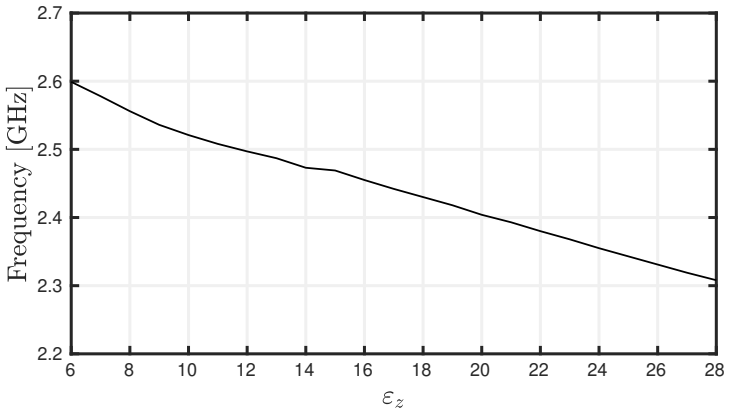

(a)

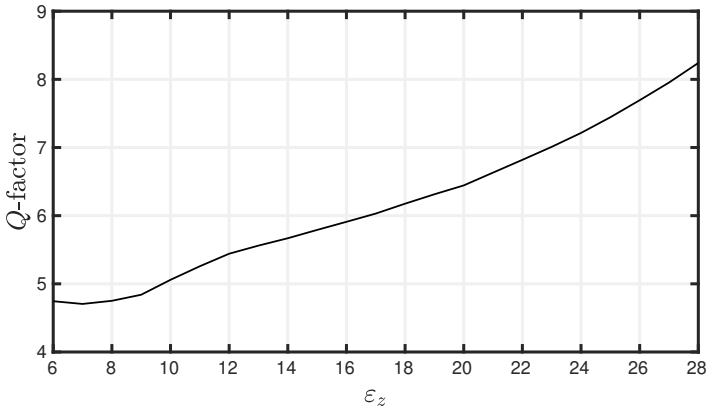

(b)

Figure 6.3: (a) Resonance frequency and (b) Q-factor of the TM_{001} mode of the proposed inhomogeneous and anisotropic DR as a function of ε_z.

Here, the goal is to have quasi-TM_{001} mode working at the ISM band. It is thus necessary to shift it from 2.32 GHz to around 2.45 GHz. The same strategy used in Chapter 2 can be employed here. It consists of using an air cavity at the center of the DRA, where the electric field of the $TE^x_{\delta 11}$, $TE^y_{1\delta 1}$, $TE^x_{\delta 13}$, and $TE^y_{1\delta 3}$ modes are weak while it is strong for the quasi-TM_{001} mode. It would therefore be possible to increase the resonance frequency of this mode without affecting too much the modes used for the GNSS bands. As a result, the structure shown in Fig. 6.4 is considered, which is very similar to the dual-band DRA except

for the presence of a square-based air cavity at its center with height h_{ag} and width w_{ag}.

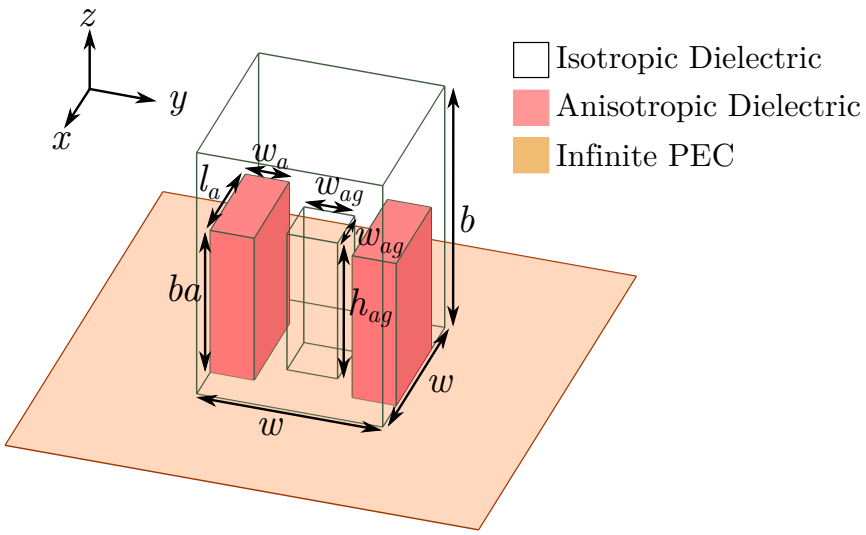

Figure 6.4: Perspective view of the proposed triple-band DR with an air cavity over an infinite ground plane.

To analyze the behavior of the different modes with the presence of the air cavity, their resonance frequencies are calculated as a function of the height h_{ag} using the Eigenmode solution of Ansys HFSS as observed in Fig. 6.5. One can note that the quasi-TM_{001} mode is more sensitive to variation of h_{ag} than the modes used for the GNSS bands. Also, the resonance frequencies of the $\text{TE}^x_{\delta 11}$ and $\text{TE}^y_{1\delta 1}$ modes remain almost the same for the different values of h_{ag}, while the $\text{TE}^x_{\delta 13}$ and $\text{TE}^y_{1\delta 3}$ modes are just a little bit more sensitive, especially for values of h_{ag} bigger than 20 mm. Therefore, depending on the height of the air cavity, it would be needed to slightly readjust the dimensions of the DRA so that the circular polarization is achieved at the L5 and L1 bands using the same reasoning presented in Chapter 3.

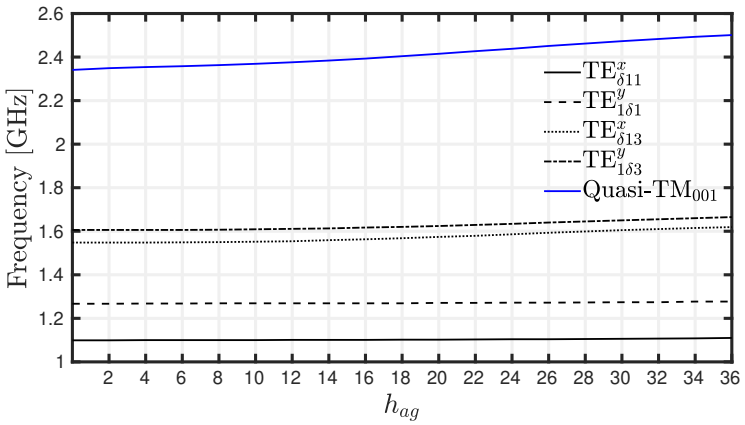

Figure 6.5: Resonance frequency of the $\text{TE}^x_{\delta 11}$, $\text{TE}^y_{1\delta 1}$, $\text{TE}^x_{\delta 13}$, $\text{TE}^y_{1\delta 3}$, and quasi-TM_{001} modes as a funcion of h_{ag}.

6.2 Antenna Design and Results

In the previous section, the natural resonances of the DR have been investigated using an infinite ground plane without any sources. Here, we describe the final DRA design, where two ports are implemented. One for the GNSS system and the other for the ISM band. To excite the quasi-TM_{001} mode, a coaxial probe is placed at the center of the DR and connected to an SMA connector, as presented in Fig. 6.6. Thereafter, it is referred to as port 2. Also, this connector is grounded using metallic vias. A conducting line is used to assure that these vias are not below the DRA, which could make difficult the manufacturing of the antenna. Besides, the presence of these vias close to the slot can affect the performance of the antenna at the GNSS bands as discussed in the next Section. Finally, as the probe and SMA connector are at the center of the substrate, the slot is coupled now to a microstrip line with a T-junction, which is here considered as port 1.

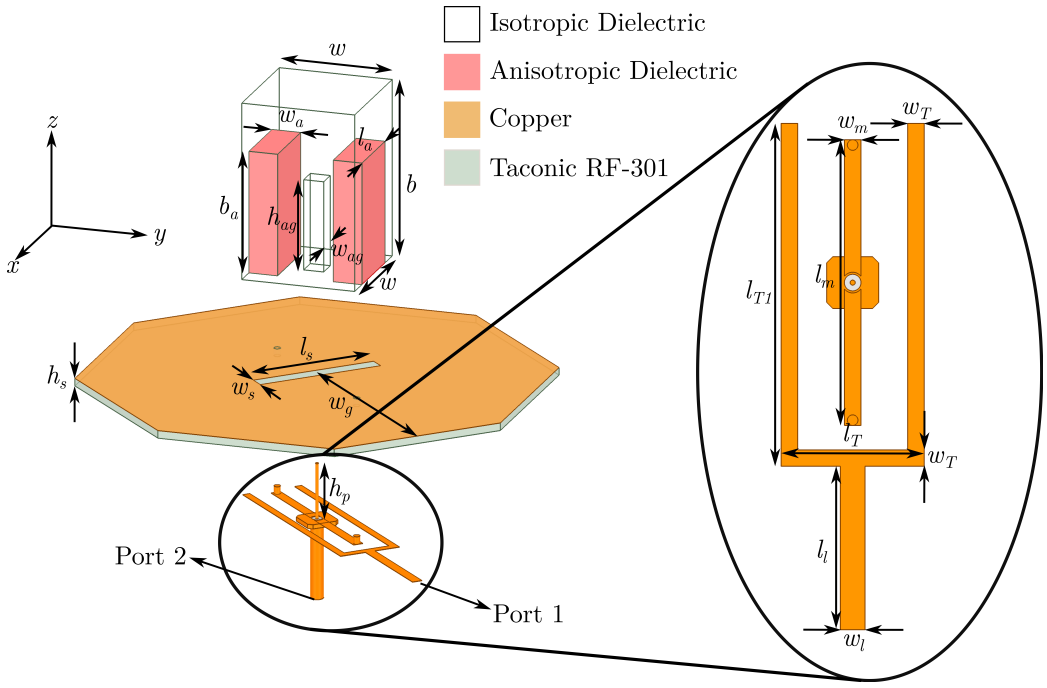

Figure 6.6: Perspective split view of the proposed inhomogeneous and anisotropic triple-band DRA.

Considering the feeding network and a finite ground plane, the triple-band DRA is optimized using Ansys HFSS. Its dimensions are $w = 45.1$ mm, $b = 70.4$ mm, $w_a = 11.4$ mm, $b_a = 48.5$ mm, $l_a = 27.6$ mm, $w_{air} = 8$ mm, $b_{air} = 36$ mm, and $w_g = 100$ mm. The permittivity of the isotropic region ε_{ri} is equal to 10 and the permittivity of the anisotropic region is represented by the following tensor in the cartesian coordinate system

$$\varepsilon_{ra} = \begin{pmatrix} 10 & 0 & 0 \\ 0 & 10 & 0 \\ 0 & 0 & 22.9 \end{pmatrix}. \tag{6.1}$$

Also, the height h_{pin} of the probe is equal to 36.5 mm and the length l_s and width w_s of the slot are 51.0 mm and 3.22 mm, respectively. Regarding the microstrip line, its dimensions are $w_l = 3.86$ mm, $l_l = 40$ mm, $l_T = 25$ mm, $w_T = 1$ mm, $l_{T1} = 92$ mm, $l_m = 35$ mm, $w_m = 4$ mm, and the stub length is 30 mm. Finally, a Taconic RF-301 substrate with tickness of 1.524 mm and dielectric constant of 2.97 is employed.

Considering the aforementioned properties, the S-parameters of the proposed dual-part triple-band DRA are computed with Ansys HFSS, as can be seen in Fig. 6.7. At the GNSS band, the simulated impedance bandwidths ($|S_{11}| < 10$ dB) are 29.6% (0.98 GHz - 1.32 GHz) and 8.7% (1.53 GHz - 1.67 GHz) for the port 1, which is related to the microstrip line that is coupled to the slot. In addition, one can note that the two feeding ports are well-isolated since the $|S_{21}|$ is below -30 dB from 0.9 GHz to 1.7 GHz. At the ISM band, namely Fig. 6.7(b), the simulated impedance bandwidth ($|S_{22}| < 10$ dB) is 8.9% from 2.35 GHz to 2.57 GHz for port 2, which is the port that excites the quasi-TM_{001} mode. Moreover, at this frequency band, the mutual coupling is still below -40 dB, which means that the two ports are not coupled.

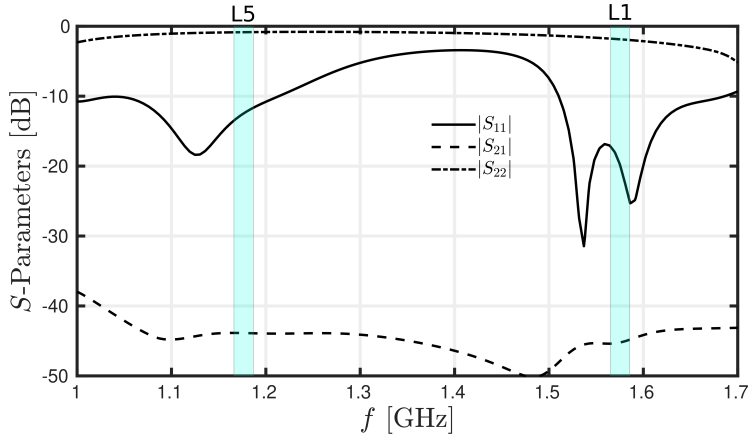

(a)

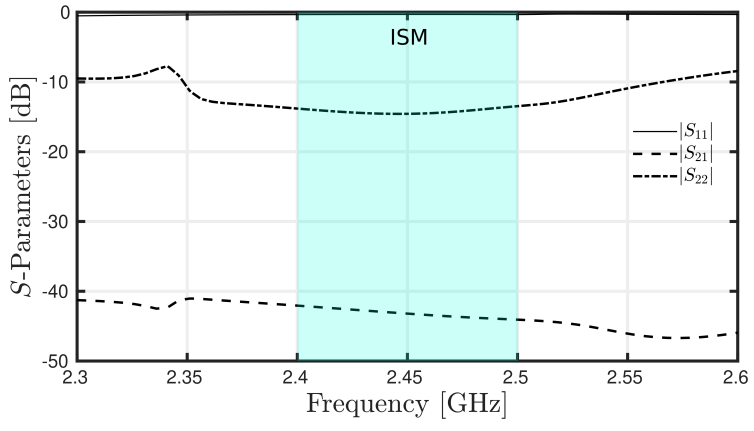

(b)

Figure 6.7: Simulated S-parameters of the inhomogeneous and anisotropic triple-band DRA at the (a) GNSS and (b) ISM bands.

Figure 6.8 shows the simulated axial ratio (AR) at the boresight direction, *i.e.* at $\theta = 0°$ and $\phi = 0°$, of the proposed triple-band DRA for port 1 while port 2 is matched to 50-Ω load. The 3-dB axial ratio bandwidths are 5.9% (1.143 GHz - 1.212 GHz) and 1.2% (1.564 GHz - 1.584 GHz), covering the L5 and L1 bands. Additionaly, this result is similar to the dual-band DRA proposed in Chapter 3, as expected.

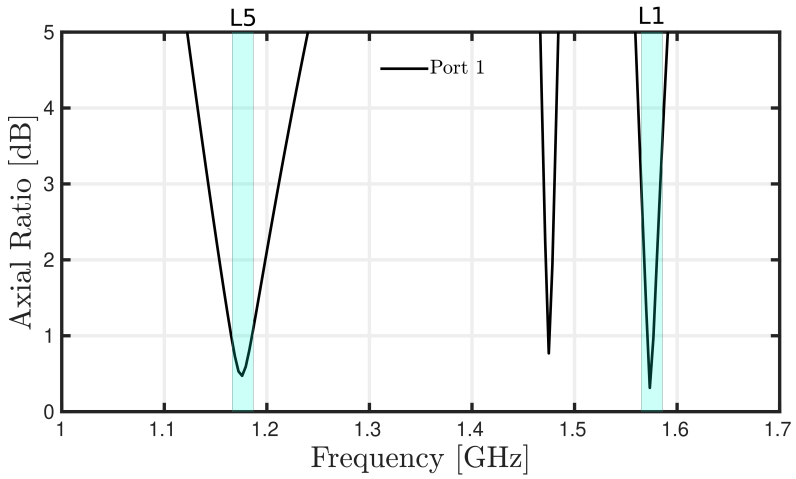

Figure 6.8: Simulated axial ratio of the inhomogeneous and anisotropic triple-band DRA at the GNSS band.

Figure 6.9 shows the left- and right-handed components of the gain, in dBi, at the L5 and L1 bands, which are calculated while port 1 is excited and port 2 is matched to a 50-Ω load. One can note that the antenna presents broadside radiation patterns, which is expected for the $\mathrm{TE}^{x}_{\delta 11}$, $\mathrm{TE}^{y}_{1\delta 1}$, $\mathrm{TE}^{x}_{\delta 13}$ and $\mathrm{TE}^{y}_{1\delta 3}$ modes. In addition, it is possible to realize that, at the L5 and L1 bands, the DRA is still right-handly circular polarized. For the ISM band, the ϕ- and θ-components are presented in Fig. 6.10. They are calculated while port 2 is excited and port 1 is matched to a 50-Ω load. A monopole-like radiation pattern with linear polarization is observed at the different planes as expected for the quasi-TM_{001} mode.

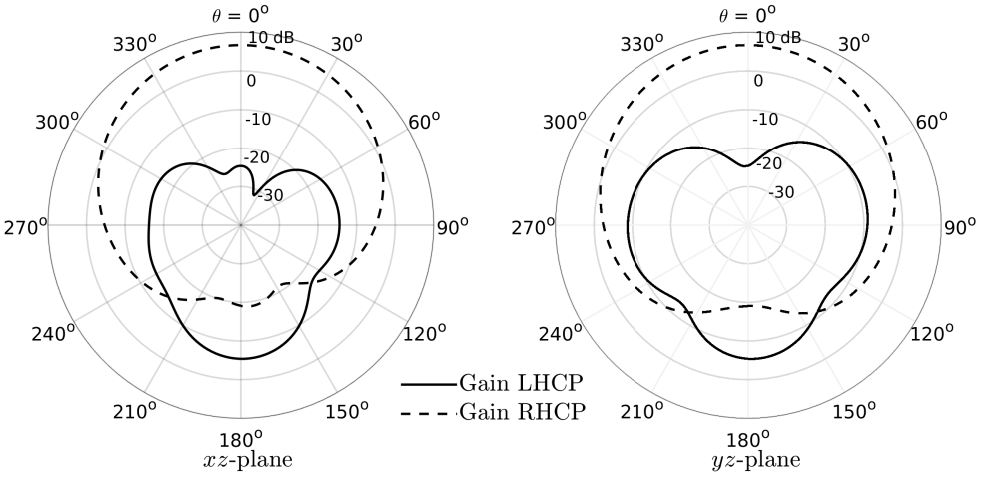

(a) $f = 1.17$ GHz

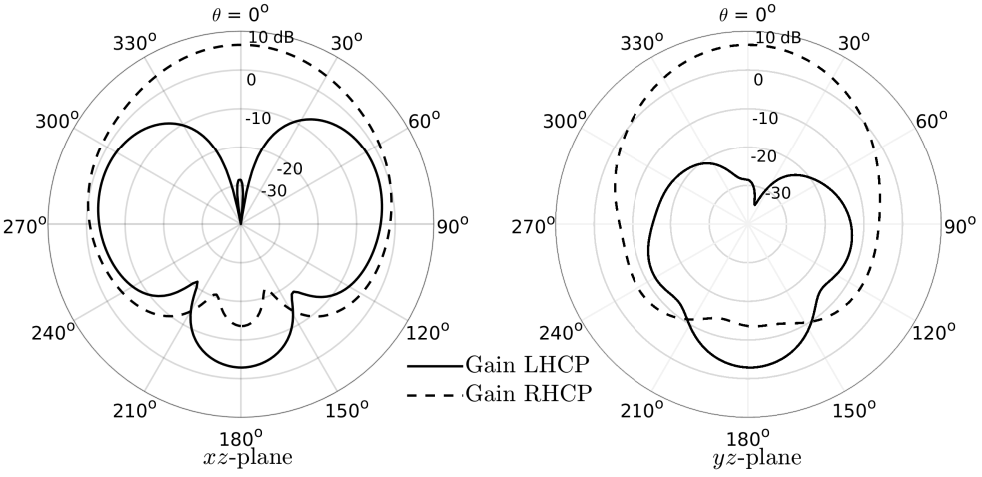

(b) $f = 1.57$ GHz

Figure 6.9: Simulated radiation patterns at (a) L5 and (b) L1 bands of the triple-band DRA.

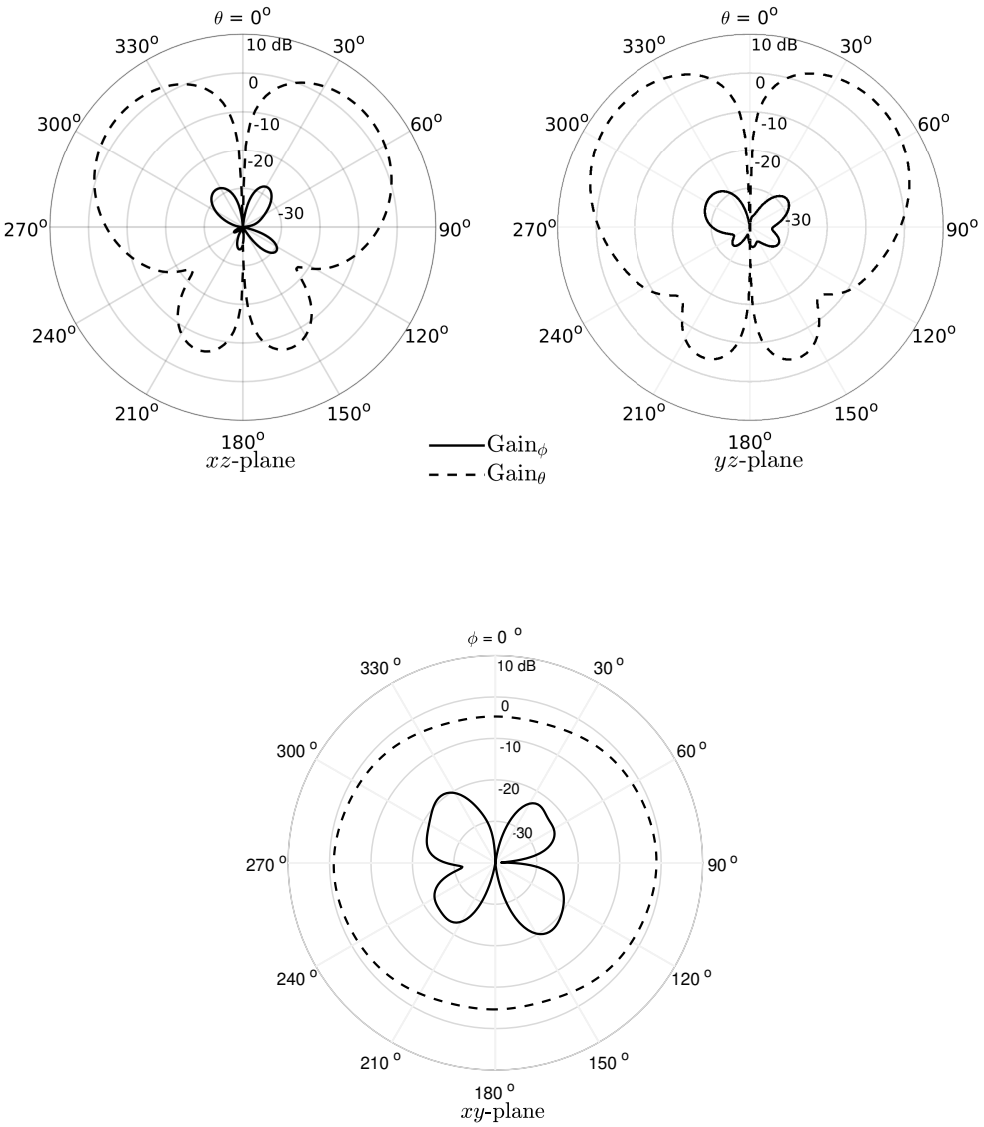

Figure 6.10: Simulated radiation patterns at ISM band (f = 2.45 GHz) of the triple-band DRA.

Figure 6.11 simulated realized gain in dBi for the proposed triple-band DRA. In Fig. 6.11(a), the realized gain at the boresight direction, *i.e.* $\theta = 0°$ and $\phi = 0°$, is presented for port 1 while port 2 is matched to a 50-Ω load. One can note that the gain at the 6.5 dBi and 6.3 dBi at the center of the L5 and L1 bands, respectively. At ISM band, the realized gain is calculated for $\theta = 60°$ and $\phi = 0°$ for port 2 while port 1 is matched to a 50-Ω load. From Fig. 6.11(b), it is possible to observe that the realized gain is 2.5 dBi at 2.45 GHz.

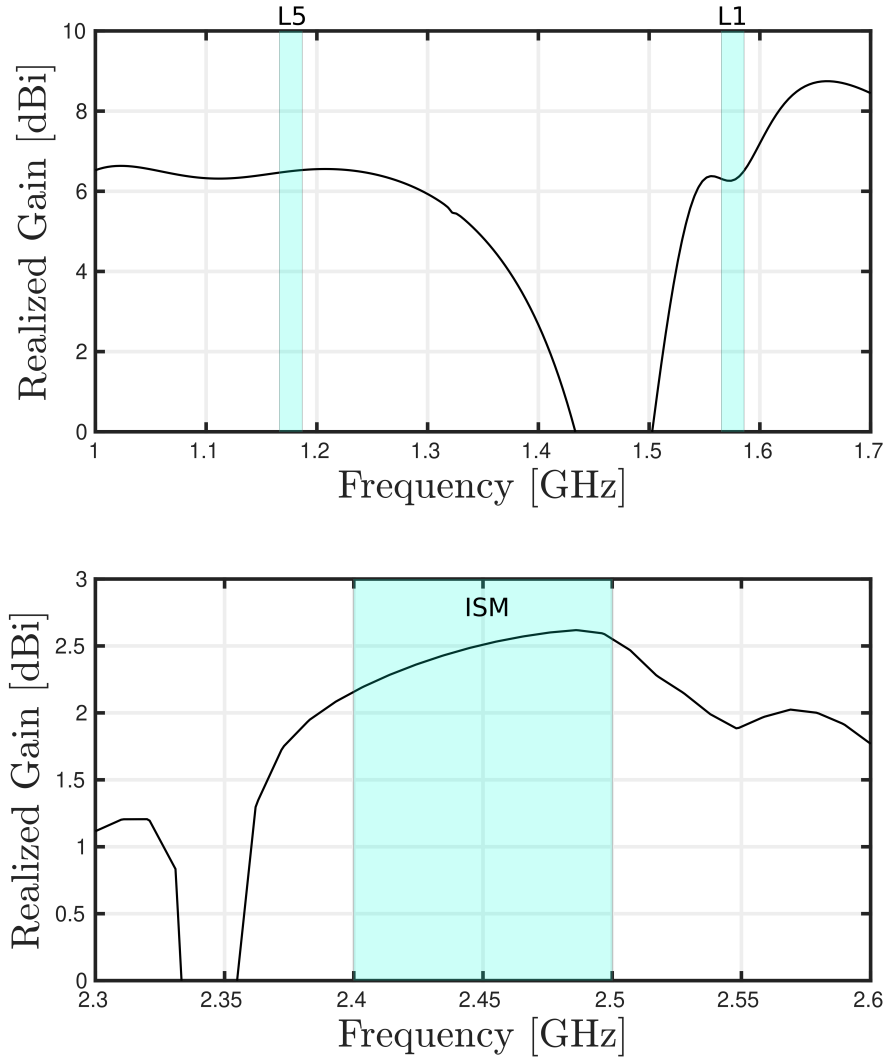

Figure 6.11: Simulated realized gain of the triple-band DRA at the (a) GNSS, for $\theta = 0°$ and $\phi = 0°$, and (b) ISM, for $\theta = 60°$ and $\phi = 0°$, bands.

The simulated axial ratio as a function of θ at $\phi = 0°$ and $\phi = 90°$ for port 1 is shown in Fig. 6.12 at the frequencies of minimum axial ratio at the L5 and L1 bands. At the lower band, at $\phi = 0°$ and $\phi = 90°$, the axial ratio is below 3 dB for $-68.05° \leq \theta \leq 66.07°$ and $-47.93° \leq \theta \leq 44.12°$, respectively. At the upper, the circular polarization happens for $-27.83° \leq \theta \leq 26.45°$ and $-61.63° \leq \theta \leq 62.15°$ at the $\phi = 0°$ and $\phi = 90°$, respectively.

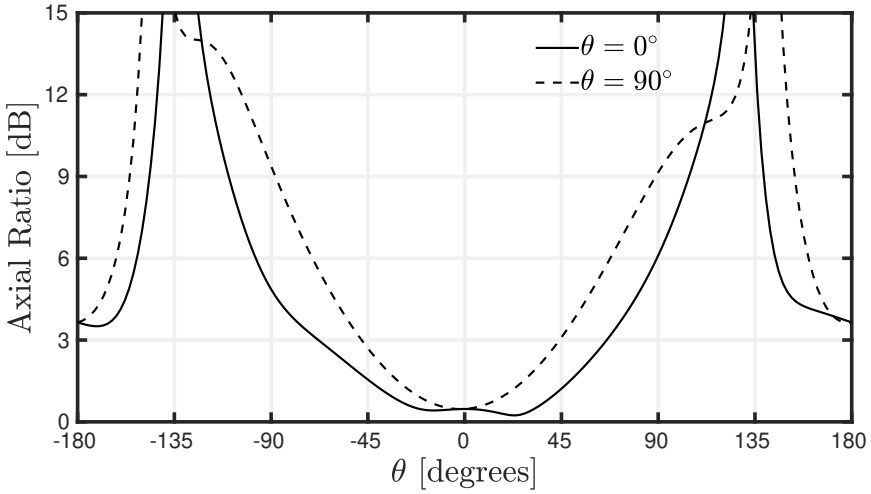

(a) $f = 1.17$ GHz

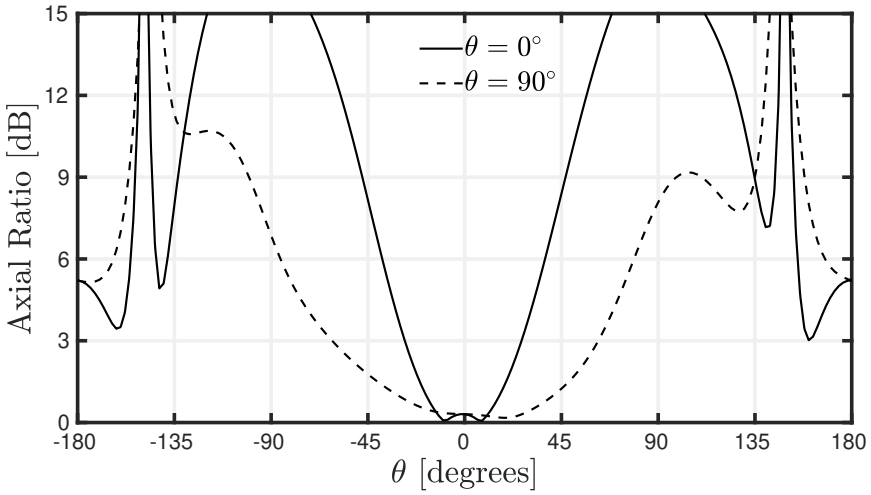

(b) $f = 1.57$ GHz

Figure 6.12: Simulated axial ratio as a function of θ at the (a) L5 and (b) L1 bands of the proposed triple-band DRA.

Finally, the results presented show that it is possible to add a third band without disturbing the performance of the DRA at the GNSS bands. This is because the air gap and probe are introduced in a region where the electric field distributions of the modes used at the L5 and L1 bands are weak.

6.3 Feeding Method

One important difference between the proposed dual- and triple-band DRAs is the feeding network. For the dual-band circularly-polarized DRA, a simple slot is coupled to a 50-Ω microstrip line to excite the fundamental $TE^{x}_{\delta 11}$ and $TE^{y}_{1\delta 1}$, and higher $TE^{x}_{\delta 13}$ and $TE^{y}_{1\delta 3}$ modes. On the other hand, for the triple-band antenna, a second port is connected to a coaxial probe placed at the center of the DRA to excite the quasi-TM_{001} mode. It is thus necessary to find a feeding scheme to keep the same performance at the GNSS band.

Regarding port 1, which excites the modes for the GNSS bands and can be seen in Fig. 6.6, a simple modification is made when compared to the dual-band DRA. Instead of using a simple and straight 50-Ω microstrip transmission line, a T-junction is used to open up some space at the center of the antenna for the probe. More precisely, port 1 is connected to a 50-Ω microstrip line that is split into two 100-Ω lines, which are coupled to the slot.

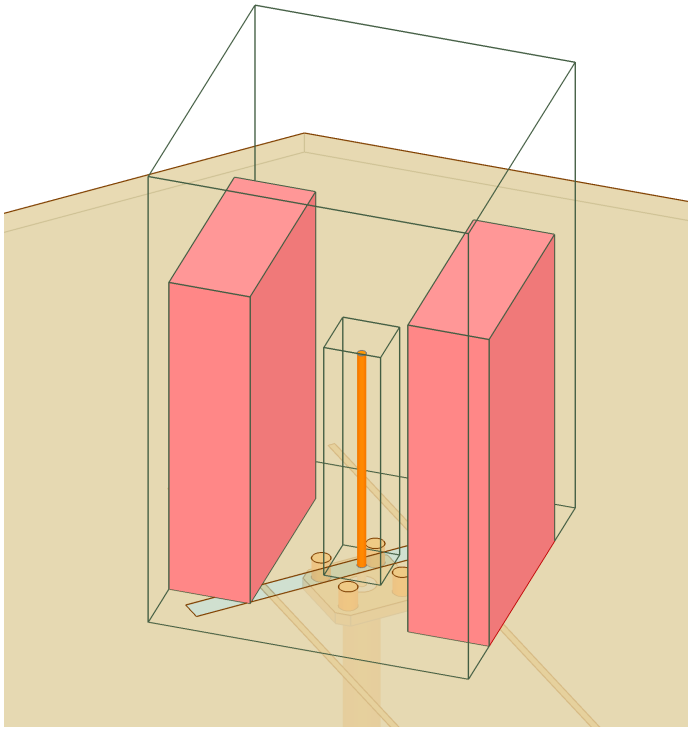

Figure 6.13: Perspective view of the proposed triple-band DRA with the initial feeding scheme.

The quasi-TM_{001} mode can now be fed by a 50-Ω coaxial probe that is connected to an SMA connector that needs to be grounded. A straightforward way to do so is using metallic vias connecting the SMA straight to the ground plane, as can be observed in Fig. 6.13. However, it was noted that these vias were disturbing the performance of the antenna at the GNSS bands since they are close to the slot. More precisely, the reflection coefficient of port 1 is highly affected by the vias around the slot and, even with optimizations of the microstrip lines and slot, better results than the one shown in Fig. 6.14 have not been observed.

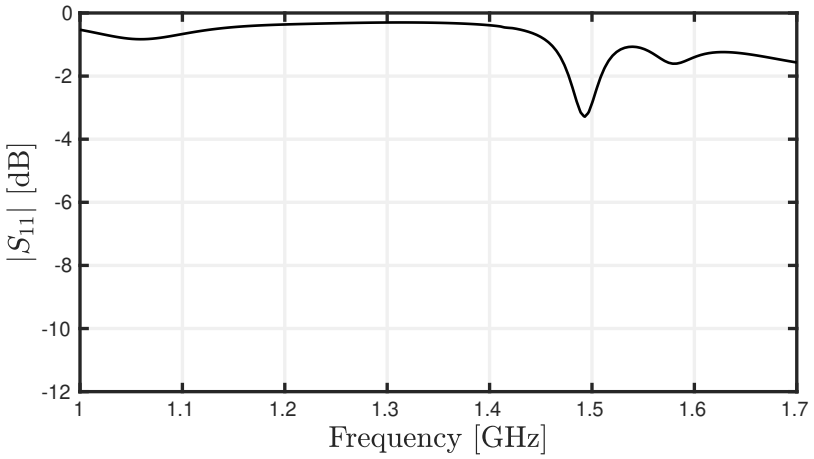

Figure 6.14: Reflection coefficient of the port 1 considering the initial feeding scheme of Fig. 6.13.

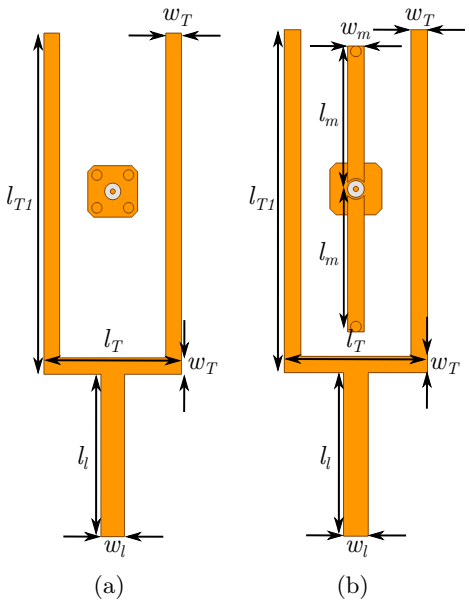

Figure 6.15: (a) Initial and (b) final feeding schemes for the triple-band DRA.

To keep the same performance at the GNSS bands, the vias are moved away from the slot and the feeding scheme shown in Fig. 6.15(b) is proposed, where microstrip transmission lines are used. To understand the influence of these lines, a parametric analysis of the reflection coefficient at the port 1 is performed as a function of their length l_m as can be observed in Fig. 6.16 ($w = 45.1$ mm, $b = 70.4$ mm, $w_a = 11.4$ mm, $b_a = 48.5$ mm, $l_a = 27.6$ mm, $w_{air} = 8$ mm, $b_{air} = 36$ mm, $w_g = 100$ mm, $h_{pin} = 36.5$ mm, $l_s = 51$ mm, $w_s = 3.22$ mm, $w_l = 3.86$ mm, $l_l = 40$ mm, $w_T = 1$ mm, $l_{T1} = 92$ mm, $w_m = 4$ mm, $\varepsilon_{ri} = \varepsilon_x = \varepsilon_y = 10$, and $\varepsilon_z = 22.9$). It is possible to note that the reflection coefficient tends to improve at both bands as the

value of l_m increases, *i.e.* as the vias are moving away from the slot. Also, it is important to point out that the optimized value of the l_m found in the previous Section is 35 mm.

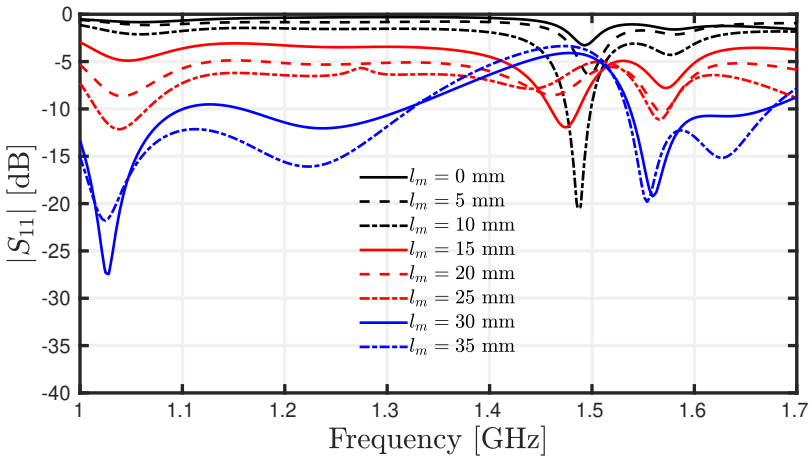

Figure 6.16: Reflection coefficient of port 1 at the GNSS bands for different values of l_m.

It is necessary to verify as well the behavior of the antenna at the ISM band as the vias are getting far away from the slot, *i.e.* as the length l_m of the lines connected to the vias increases. The $|S_{22}|$ is shown as a function of l_m at the ISM band in Fig. 6.17. It is noted that each of the metallic arms acts as stubs connected to the coaxial cable, then, it is necessary to pay attention to the value of l_m in terms of λ_g, which is the guided wavelength at 2.45 GHz. For $l_m = 0$ mm, as expected, the reflection coefficient of port 2 presents a good result at the ISM band. However, for $l_m = 17$ mm, the antenna is not well-matched anymore. This value of l_m is approximately $\frac{\lambda_g}{4}$ and, then, the short-circuited microstrip transmission lines act as an open circuit at their input. On the other hand, for $l_m = 35$ mm, the antenna is well-matched again since l_m is approximately $\frac{\lambda_g}{2}$ and, thus, the lines act as a short circuit from the point of view of the SMA connector.

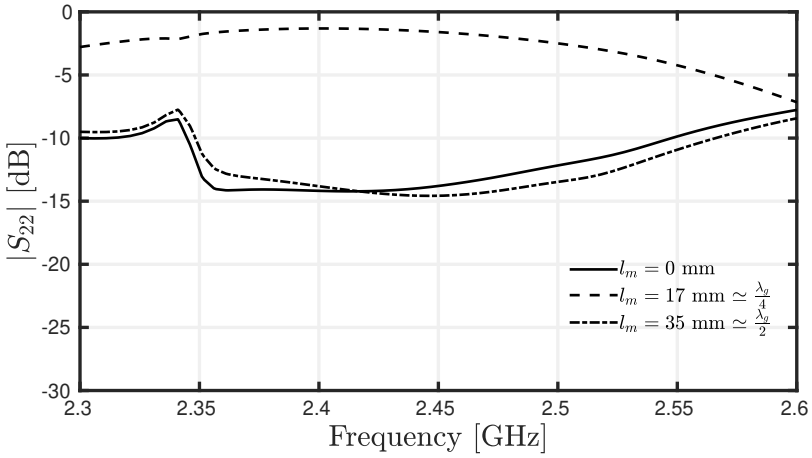

Figure 6.17: Reflection coefficient of port 2 at the ISM band for different values of l_m.

6.4 Conclusion

An inhomogeneous and anisotropic dual-part triple-band rectangular DRA is presented in this Chapter to operate at the L5 and L1 bands of the GNSS and the 2.45-GHz ISM band. At the GNSS bands, the antenna is excited by a simple slot and presents circular polarization and broadside radiation patterns as for the antenna detailed in Chapter 3. On the other hand, at the ISM band, the antenna is fed by a probe and presents an omnidirectional pattern with linear polarization.

At the GNSS band, the operation principle is the same developed in Chapter 3, where a square-based dielectric is used and two anisotropic regions are introduced to manipulate the $TE^{x}_{\delta 11}$, $TE^{y}_{1\delta 1}$, $TE^{x}_{\delta 13}$, and $TE^{y}_{1\delta 3}$ modes to have circular polarization at two bands. However, instead of using a straight microstrip line to couple to the slot, a T-junction is used to open up some space at the center of the DRA so that it can be explored to excite the third band.

In the literature, the presence of quasi-TM_{011} mode, which radiates as a vertical electric dipole, was observed in isotropic rectangular DRAs with a square base. The possibility of exciting this mode in an anisotropic and inhomogeneous DRA with a square base was investigated in this Chapter and, it was verified that this mode still exists under these conditions. The quasi-TM_{011} mode is excited at 2.45 GHz by a probe and its resonance frequency can be controlled by adding and adjusting the dimensions of an air cavity at the center of the DRA, which is similar to the method used in Chapter 2.

The modes used at the GNSS and ISM bands can coexist at the same DRA without disturbing each other since the quasi-TM_{011} mode is orthogonal to the other ones. Also, due to the analysis of the electric field distribution of each one of these modes, the electric properties of the DRA can be locally controlled to achieve the expected results. An orthogonal feeding system is proposed to properly excite the modes at the GNSS and ISM bands without disturbing the performance of each other.

Conclusion and Perspectives

The main objective of this Ph.D. thesis was to investigate and design multiband dielectric resonator antennas with special radiation and polarization properties. More precisely, in this work, the use of 3D-printing technology, which has the potential to unlock the full potential of DRAs, has been explored to design these DRAs. The conclusion of each chapter is presented as follows:

Chapter 1 has been dedicated to the necessary background for the comprehension of this work as well as the state-of-the-art about multiband dielectric resonator antennas, which is essential to establish the research axes of this thesis. Some challenges have been identified in designing multiband DRAs with given radiation properties where most of these properties were achieved by using complex feeding networks and/or physical modifications in the shape of the DRA. None of them explored the dielectric properties of the DRA to do so, which could be realized by using additive manufacturing. Therefore, this chapter has paved the way for all further development found in this work.

Chapter 2 has studied the design of a dual-band rectangular DRA for the L5 and L1 bands of the GNSS. For this application, it is interesting to have broadside radiation patterns and, then, the fundamental $\mathrm{TE}^{x}_{\delta 11}$ and $\mathrm{TE}^{y}_{1\delta 1}$ modes are used at the L5 and L1 bands, respectively. However, at the L1 band, it has been observed that the radiation pattern is not as expected. To find out the reasons behind it, an investigation using the Eigenmode solution of HFSS detected the presence of the $\mathrm{TE}^{x}_{\delta 21}$ mode at the L1 band and, due to its electric field distribution, this mode could be excited as well. To overcome this issue, the permittivity of the dielectric has locally been controlled to increase the resonance frequency of this undesirable mode by adding an air cavity at the center of the antenna. This is because the electric fields of the fundamental modes are weak in this region while they are strong for the $\mathrm{TE}^{x}_{\delta 21}$ mode. The radiation pattern results have demonstrated that this method is useful to manipulate the resonance frequency of a given radiating mode.

Chapter 3 has been dedicated to the design of a dual-band dielectric resonator antenna with circular polarization at the L5 and L1 bands of the GNSS. The fundamental $\mathrm{TE}^{x}_{\delta 11}$ and $\mathrm{TE}^{y}_{1\delta 1}$ modes are excited at the lower band as well as the higher-order $\mathrm{TE}^{x}_{\delta 13}$ and $\mathrm{TE}^{y}_{1\delta 3}$ modes at the upper band. To fulfill the circular polarization conditions, the electric field distributions of these modes were carefully analyzed and, then, the electric properties of the DRA were locally controlled by the introduction of two anisotropic regions. As all of these modes are fed by a single slot and a square-based DRA is considered, the achievement of circular polarization at two bands relies exclusively on its dielectric properties, which is a novelty itself since similar results found in the literature are achieved by controlling the shape of the DRA and/or using multiple ports or complex feeding networks.

Chapter 4 has introduced the concept of artificial materials made up of periodic structures and 3D printing. Indeed, the electric properties of the antenna proposed in Chapter 3 were directly assigned on Ansys HFSS for the full-wave simulations and it required a practical

implementation. Periodic structures made up of subwavelength unit cells to emulate artificial anisotropic and isotropic media have thus been proposed and studied to investigate their design and their limitations regarding 3D printing. To retrieve the effective permittivity of these cells, the S-parameters retrieval method and dispersion diagram have been used at first. However, the curves of extracted permittivity presented different behaviors as the frequency increased for these methods. Then, the effective permittivity considering a dielectric resonator has been computed using the Eigenmode solution of Ansys HFSS. This analysis has demonstrated that the dispersion diagram is more accurate to compute the effective permittivity of periodic structures to design DRA, especially for electrically-large unit cells.

Chapter 5 has been devoted to combine the antenna proposed in Chapter 3 and the unit cells presented in Chapter 4. The simulated results have demonstrated the efficiency of periodic structures to design an anisotropic and inhomogeneous DRA. Also, the first attempt to 3D-print the DRA for the L5 and L1 bands fails, and, then, following the feedback of the technicians to reduce the size of the antenna, the DRA was re-designed to operate at the L1 and up-link of the TT&C bands. The antenna has finally been 3D-printed and the measured results are in good agreement with the simulated ones.

Chapter 6 has presented a triple-band dielectric resonator antenna operating at the L5, L1, and 2.45-GHz ISM bands. The idea was to keep the same performance at the GNSS bands, as seen in Chapter 3, and add a third band with the excitation of the quasi-TM_{001} mode. However, by that time, this mode has been only observed in isotropic and homogeneous DRAs with a square base. An investigation has thus been developed to verify the existence of this mode in an inhomogeneous and anisotropic DRA, which is proved due to the identifications of its electric field distribution. Moreover, as the quasi-TM_{001} mode behaves as a vertical electric dipole, an air cavity placed at the center of the DRA has been used to control its resonance frequency. Compared to the model proposed in Chapter 3, some modifications have been made in the feeding network to leave some space at the center of the DRA for the presence of the probe. The results of S-parameters, radiation pattern, and axial ratio have demonstrated that the antenna operates almost independently at the GNSS and ISM bands.

To summarize, the developments from this Ph.D. thesis provide several contributions to the current literature:

I) The local control of the effective permittivity in electrically-small and resonant structures by using 3D-printed subwavelength isotropic and anisotropic unit cells. In this work, three different methods to calculate the effective permittivity of these cells have been presented, showing the pros and cons of them to design dielectric resonators.

II) A dual-band circularly-polarized dielectric resonator antenna has been proposed by using an inhomogeneous and anisotropic dielectric. The circular polarization in both bands happens due to the local control of the electric permittivity of the antenna, which is completely new in the literature since this type of performance is most of the time achieved by modifying the shape of the DR and/or using complex feeding networks. The same concept has been used as well to design a triple-band antenna.

III) A prototype of the dual-band circularly-polarized DRA has been 3D-printed in ceramic and experimental measurements have been carried out to validate the simulated results.

Perspective for Future Works

The future investigations from the developments provided in this Ph.D. thesis can be listed as follows:

Antenna performance: To show the potential of the local control of dielectric properties of a resonator by using the 3D-printing, we used a single slot to excite the antenna. However, the employment of a single feeding source limits the 3-dB axial bandwidth as seen in Section 3.4. Therefore, complex feeding networks could be combined with the local control of the dielectric permittivity of the dielectric to improve the performance of the antenna in terms of axial ratio.

Antenna size reduction: Depending on the application, the antennas developed in this thesis can be too bulky. Thus, some techniques could be investigated to overcome this issue. The use of metallic parasitic elements sounds promising as well as the use of nonconventional dielectric resonator shapes.

Antenna manufacturing: At the end of this Ph.D. thesis, a prototype of a dual-band circularly-polarized DRA is 3D-printed in ceramics and the experimental results agreed with the simulated ones. However, before successfully 3D-printing the DRA, several prototypes have been broken during the manufacturing process. It sounds thus that the 3D-printing process presents some mechanical weaknesses when it comes to inhomogeneous DRAs. In this context, the study on the properties of the unit cells considering different topologies can be envisaged to find the compromise between mechanical and electrical properties.

Artificial materials applied to DRAs: So far, the periodic subwavelength unit cells have been used to create anisotropic or isotropic and homogeneous or inhomogeneous for DRA applications. However, it is possible to go further by exploring some other features of periodic structures. In this context, dielectrics with engineered dispersion could be investigated to design multi or wideband DRAs.

Antenna integration: In this work, the measurement of the dual-band CP DRA is performed in an anechoic chamber, *i.e.* in a controlled environment. Nevertheless, it would be interesting to do the integration of this antenna into a platform for a practical application such as a UAV or nanosatellite. This integration would allow the investigation of the performance of the antenna in a noncontrolled environment. In case of compatibility issues, some solutions may be proposed to improve the performance of the antenna under these conditions.

Publications

Communications in international conferences with technical programme committee

- J. B. de Araújo, C. Morales, C. Morlaas, A. Chabory, R. Pascaud, M. Grzeskowiak, and G. Mazingue, "A dual-band hollow dielectric resonator antenna for GPS applications," in *2021 IEEE International Symposium on Antennas and Propagation and USNC-URSI Radio Science Meeting (APS/URSI)*, pp. 1177–1178, IEEE, 2021

Communications in national (French) conferences

- J. B. de Araújo, C. Morlaas, A. Chabory, R. Pascaud, M. Grzeskowiak, and G. Mazingue, "Inhomogeneous and anisotropric 3D-printed dielectric resonator antenna with dual-band and circular polarization," in *22ème édition des Journées Nationales Microondes (JNM)*, 2022

International journals

- J. B. de Araújo, C. Morlaas, A. Chabory, R. Pascaud, M. Grzeskowiak, and G. Mazingue, "3D-printed dual-band circularly-polarized dielectric resonator antenna," *IEEE Transactions on Antennas and Propagation*, 2022 (in Preparation)

Appendix A

Parameter Retrieval of Periodic Structures on HFSS

Mathematical Formulation

Periodic structures used to be analyzed in terms of their effective constitutive parameters, which can be extracted using scattering-parameters (S-parameters) retrieval methods [88][89]. These methods are easily employed in electromagnetic simulation software such as Ansys HFSS and CST, for instance.

In this work, the retrieval method proposed in [90] is considered, where the reflection S_{11} and transmission S_{21} coefficient are used to calculated the effective permittivity ε_{eff} and permeability μ_{eff}. In this case, the periodic structure is assumed to be an effective homogeneous slab. Considering a normally-incident plane wave on a homogeneous slab, S_{11} and S_{21} can be written as

$$S_{11} = \frac{R\left(1 - e^{j2nk_0d}\right)}{1 - R^2 \cdot e^{j2nk_0d}}, \tag{A.1}$$

$$S_{21} = \frac{\left(1 - R^2\right) \cdot e^{j2nk_0d}}{1 - R^2 \cdot e^{j2nk_0d}}, \tag{A.2}$$

where $R = (z-1)/(z+1)$, d is the thickness of the slab, k_0 is the free-space wavenumber, z is the impedance, and n is the refractive index.

The impedance z and refractive index n can be calculated using the following equations:

$$z = \pm\sqrt{\frac{(1+S_{11})^2 - S_{21}^2}{(1-S_{11})^2 - S_{21}^2}}, \tag{A.3}$$

$$e^{jnk_0d} = \frac{S_{21}}{1 - S_{11}R}, \tag{A.4}$$

$$n = \frac{1}{k_0 d}\left[\left\{\left[\ln\left(e^{jnk_0d}\right)\right]'' + 2m\pi\right\} - j\left[\ln\left(e^{jnk_0d}\right)\right]'\right], \tag{A.5}$$

where $(\bullet)'$ and $(\bullet)''$ represents the real and complex components of the operators, respectively. In addition, the index m indicates the presence of multiple solutions for n. However, if the material at issue has passive nature, m can be assumed to be zero and, then, only one solution is found. Also, the sign of z must be chosen so that $z \geq 0$, if the periodic structure at issue were passive [88, 89, 91].

Thus, the effective permittivity ε_{eff} and permeability μ_{eff} are expressed as

$$\varepsilon_{\text{eff}} = \frac{n}{z} \tag{A.6}$$

$$\mu_{\text{eff}} = nz \tag{A.7}$$

Extraction of S-Parameters on Ansys HFSS

Previously in this appendix, all the mathematical formulation is presented considering a plane wave with normal incidence on an infinitely large periodic structure, which is achieved by the infinite and periodic repetition of its unit cell. Also, most commercial electromagnetic simulation software present periodic boundary conditions, which become the simulation of this kind of structure easier and faster.

In this work, Ansys HFSS is used to design the unit cells and extract their effective parameters. The employed boundary conditions and excitation ports are thus explained in this appendix. Moreover, an incident electromagnetic wave propagating in $\pm z$-axis is considered, and 2-D periodic boundary conditions along the xy-plane are assigned, which are realized by using the configuration shown in Fig. A.1. In addition, one can note that the unit cell is surrounded by an airbox, where the boundary conditions and excitation port will be set. The shape and dimension of the airbox along the xy-plane must be the same as the unit cell and its height h will be discussed further.

The periodic boundary conditions can be assigned on Ansys HFSS by using perfect electric/magnetic or master/slave conditions. These conditions are supposed to present the same result for cubic-shaped unit cells, however, when it comes to complex shapes, only the master/slave condition can be used effectively. In this work, the master/slave boundary condition is employed along the sidewalls of the unit cell, so that 2D periodic structures can be realized from a single unit cell.

Besides the boundary conditions, it is necessary to choose the proper excitation port and, to do this on Ansys HFSS, Floquet ports are assigned on the top and bottom faces of the air box. Floquet ports are used exclusively with planar-periodic structures and they can be used

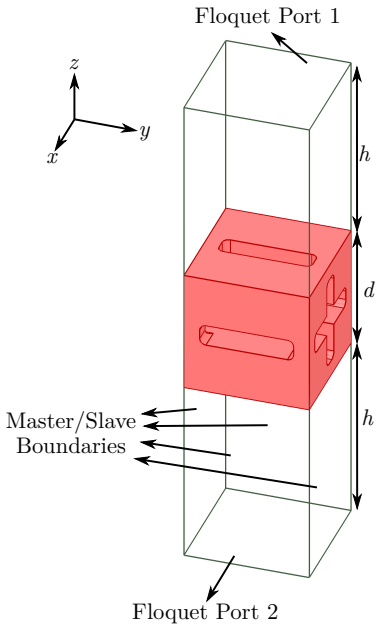

Figure A.1: Unit cell, boundary conditions and excitation ports on Ansys HFSS.

with master/slave boundary conditions [92]. Moreover, Floquet modes are used to represent the fields on the port boundary, which are plane waves with propagation directions defined by the frequency and shape of the periodic structure. The distance h between the port and the surface of the unit cell must be great enough to allow the evanescent modes to decay and a rule of thumb used for this variable is a quarter of the wavelength at the lowest frequency of the band at issue.

When it comes to the parameter retrieval of anisotropic materials, it is important to know the polarization of the incident electromagnetic wave. Considering the following tensor of permittivity

$$\varepsilon_r = \begin{pmatrix} \varepsilon_x & 0 & 0 \\ 0 & \varepsilon_y & 0 \\ 0 & 0 & \varepsilon_z \end{pmatrix}, \tag{A.8}$$

and to calculate ε_x, the electric field must be x-directed and the same reasoning must be used to calculate ε_y and ε_z. However, with the configuration presented in Fig. A.1, where the incoming plane wave propagates in the $\pm z$-direction, it is possible to calculate only ε_x and ε_y. To calculate ε_z, it is necessary to rotate the air box so that the propagation direction is along the x- or y-axes. Also, to know which component of the permittivity tensor is being calculated, the proper Floquet modes must be chosen in the Floquet Port Setup on HFSS, and the electric field polarization can be seen in Floquet Port Display.

Bibliography

[1] Ben Redwood, Filemon Schöffer, and Brian Garret. *The 3D printing handbook: technologies, design and applications*. 3D Hubs, 2017 (cit. on pp. 1, 63, 65, 66).

[2] Annamaria Gisario et al. "Metal additive manufacturing in the commercial aviation industry: A review." In: *Journal of Manufacturing Systems* 53 (2019), pp. 124–149 (cit. on p. 1).

[3] Mallikarjuna N Nadagouda, Vandita Rastogi, and Megan Ginn. "A review on 3D printing techniques for medical applications." In: *Current Opinion in Chemical Engineering* 28 (2020), pp. 152–157 (cit. on pp. 1, 65).

[4] Tom Lecklider. "3D printing drives automotive innovation." In: *EE-Evaluation Engineering* 56.1 (2017), pp. 16–20 (cit. on p. 1).

[5] Benoit Furet, Philippe Poullain, and Sebastien Garnier. "3D printing for construction based on a complex wall of polymer-foam and concrete." In: *Additive Manufacturing* 28 (2019), pp. 58–64 (cit. on pp. 1, 65).

[6] Jeffrey I Lipton et al. "Additive manufacturing for the food industry." In: *Trends in food science & technology* 43.1 (2015), pp. 114–123 (cit. on pp. 1, 65).

[7] Francesco Paolo Chietera, Riccardo Colella, and Luca Catarinucci. "Dielectric Resonators Antennas Potential Unleashed by 3D Printing Technology: A Practical Application in the IoT Framework." In: *Electronics* 11.1 (2022), p. 64 (cit. on p. 1).

[8] Diogo Helena et al. "Antenna design using modern additive manufacturing technology: A review." In: *IEEE Access* (2020) (cit. on pp. 1, 2, 64).

[9] Ryan A Bahr et al. "Novel uniquely 3D printed intricate Voronoi and fractal 3D antennas." In: *2017 IEEE MTT-S International Microwave Symposium (IMS)*. IEEE. 2017, pp. 1583–1586 (cit. on p. 2).

[10] Ila Agnihotri and Satish K Sharma. "Design of a 3D metal printed axial corrugated horn antenna covering full Ka-band." In: *IEEE Antennas and Wireless Propagation Letters* 19.4 (2020), pp. 522–526 (cit. on p. 2).

[11] Anastasios Papathanasopoulos et al. "3-D-Printed Shaped and Material-Optimized Lenses for Next-Generation Spaceborne Wind Scatterometer Weather Radars." In: *IEEE Transactions on Antennas and Propagation* 70.5 (2021), pp. 3163–3172 (cit. on pp. 2, 3).

[12] Chen Ding and Kwai-Man Luk. "Wideband Omnidirectional Circularly Polarized Antenna for Millimeter-Wave Applications Using Conformal Artificial Anisotropic Polarizer." In: *IEEE Transactions on Antennas and Propagation* 70.4 (2021), pp. 2450–2458 (cit. on pp. 2, 3).

[13] Muhammad S Anwar, Hasan Abufanas, and Axel Bangert. "3D printed dielectric lens for the gain enhancement of a broadband antenna." In: *International Journal of RF and Microwave Computer-Aided Engineering* 30.4 (2020), e22115 (cit. on p. 3).

[14] Gautier Mazingue et al. “3D Printed Ceramic Antennas for Space Applications.” In: *2020 14th European Conference on Antennas and Propagation (EuCAP)*. IEEE. 2020, pp. 1–5 (cit. on pp. 3, 67, 68, 71, 83).

[15] Quentin Lamotte et al. “Multi-permittivity 3D-printed Ceramic Dual-Band Circularly Polarized Dielectric Resonator Antenna for Space Applications.” In: *2021 15th European Conference on Antennas and Propagation (EuCAP)*. IEEE. 2021, pp. 1–5 (cit. on pp. 3, 4, 68, 69, 71, 83).

[16] Carlos David Morales Peña et al. “3D-printed ceramics with engineered anisotropy for dielectric resonator antenna applications.” In: *IET Electronics Letters* (2021) (cit. on pp. 3, 4, 36, 37, 68, 69, 71, 83).

[17] Constantine A Balanis. *Advanced engineering electromagnetics*. John Wiley & Sons, 2012 (cit. on pp. 8–10, 16).

[18] Jin Au Kong. *Electromagnetic wave theory*. Wiley-Interscience, 1990 (cit. on p. 8).

[19] RD Richtmyer. “Dielectric resonators.” In: *Journal of Applied Physics* 10.6 (1939), pp. 391–398 (cit. on p. 9).

[20] A Okaya and LF Barash. “The dielectric microwave resonator.” In: *Proceedings of the IRE* 50.10 (1962), pp. 2081–2092 (cit. on pp. 9, 12).

[21] Jean Van Bladel. “On the resonances of a dielectric resonator of very high permittivity.” In: *IEEE Transactions on Microwave Theory and Techniques* 23.2 (1975), pp. 199–208 (cit. on pp. 10, 16).

[22] M Verplanken and J Van Bladel. “The Electric-Dipole Resonances of Ring Resonators of Very High Permittivity (Short Papers).” In: *IEEE Transactions on Microwave Theory and Techniques* 24.2 (1976), pp. 108–112 (cit. on p. 10).

[23] M Verplanken and J Van Bladel. “The magnetic-dipole resonances of ring resonators of very high permittivity.” In: *IEEE Transactions on Microwave Theory and Techniques* 27.4 (1979), pp. 328–333 (cit. on p. 10).

[24] S Long, Mark McAllister, and Liang Shen. “The resonant cylindrical dielectric cavity antenna.” In: *IEEE Transactions on Antennas and Propagation* 31.3 (1983), pp. 406–412 (cit. on p. 10).

[25] MW McAllister, S Andrew Long, and GL Conway. “Rectangular dielectric resonator antenna.” In: *Electronics letters* 19.6 (1983), pp. 218–219 (cit. on p. 10).

[26] MW McAllister and S Andrew Long. “Resonant hemispherical dielectric antenna.” In: *Electronics Letters* 20.16 (1984), pp. 657–659 (cit. on p. 10).

[27] MT Birand and RV Gelsthorpe. “Experimental millimetric array using dielectric radiators fed by means of dielectric waveguide.” In: *Electronics Letters* 17.18 (1981), pp. 633–635 (cit. on p. 10).

[28] M Haneishi and H Takazawa. “Broadband circularly polarised planar array composed of a pair of dielectric resonator antennas.” In: *Electronics Letters* 21.10 (1985), pp. 437–438 (cit. on p. 10).

[29] AA Kishk, HA Auda, and BC Ahn. "Accurate prediction of radiation patterns of dielectric resonator antennas." In: *Electronics Letters* 23.25 (1987), pp. 1374–1375 (cit. on p. 10).

[30] AA Kishk et al. "Broadband stacked dielectric resonator antennas." In: *Electronics Letters* 25.18 (1989), pp. 1232–1233 (cit. on p. 10).

[31] Ahmed A Kishk and Atef Z Elsherbeni. "Radiation characteristics of dielectric resonator antennas loaded with a beam-forming ring." In: *Archiv Elektronik und Uebertragungstechnik* 43 (1989), pp. 158–165 (cit. on p. 10).

[32] KW Leung, KM Luk, and KYA Lai. "Input impedance of hemispherical dielectric resonator antenna." In: *Electronics Letters* 27.24 (1991), pp. 2259–2260 (cit. on p. 10).

[33] KW Leung et al. "Theory and experiment of a coaxial probe fed hemispherical dielectric resonator antenna." In: *IEEE Transactions on Antennas and Propagation* 41.10 (1993), pp. 1390–1398 (cit. on p. 10).

[34] RK Mongia. "Half-split dielectric resonator placed on metallic plane for antenna applications." In: *Electronics Letters* 25.7 (1989), pp. 462–464 (cit. on p. 10).

[35] A Ittipiboon et al. "Aperture fed rectangular and triangular dielectric resonators for use as magnetic dipole antennas." In: *Electronics Letters* 29.23 (1993), pp. 2001–2002 (cit. on p. 10).

[36] Aldo Petosa. *Dielectric resonator antenna handbook*. Artech, 2007 (cit. on pp. 10, 11, 13, 15, 16, 58).

[37] Shady Keyrouz and Diego Caratelli. "Dielectric resonator antennas: basic concepts, design guidelines, and recent developments at millimeter-wave frequencies." In: *International Journal of Antennas and Propagation* 2016 (2016) (cit. on pp. 11, 12).

[38] Enrique AJ Marcatili. "Dielectric rectangular waveguide and directional coupler for integrated optics." In: *Bell System Technical Journal* 48.7 (1969), pp. 2071–2102 (cit. on pp. 13, 14).

[39] Bruce Henry et al. *Mutual Coupling Between Rectangular Dielectric Resonator Antenna Elements*. Tech. rep. DEFENCE RESEARCH ESTABLISHMENT OTTAWA (ONTARIO), 1998 (cit. on p. 13).

[40] Roger F Harrington. *Time-harmonic electromagnetic fields*. McGraw-Hill, 1961 (cit. on p. 13).

[41] Constantine A Balanis. *Antenna theory: analysis and design*. John wiley & sons, 2015 (cit. on p. 15).

[42] RK Mongia. "Theoretical and experimental resonant frequencies of rectangular dielectric resonators." In: *IEE proceedings H (microwaves, antennas and propagation)*. Vol. 139. 1. IET. 1992, pp. 98–104 (cit. on p. 16).

[43] Yi-Fang Lin, Hua-Ming Chen, and Chia-Ho Lin. "Compact dual-band hybrid dielectric resonator antenna with radiating slot." In: *IEEE Antennas and Wireless Propagation Letters* 8 (2008), pp. 6–9 (cit. on p. 17).

[44] Yong Mei Pan, Shao Yong Zheng, and Bin Jie Hu. "Design of dual-band omnidirectional cylindrical dielectric resonator antenna." In: *IEEE antennas and wireless propagation letters* 13 (2014), pp. 710–713 (cit. on pp. 17, 18).

[45] Yongmei Pan and Kwok Wa Leung. "Wideband circularly polarized trapezoidal dielectric resonator antenna." In: *IEEE Antennas and Wireless Propagation Letters* 9 (2010), pp. 588–591 (cit. on p. 18).

[46] Ricky Chair et al. "Aperture fed wideband circularly polarized rectangular stair shaped dielectric resonator antenna." In: *IEEE transactions on antennas and propagation* 54.4 (2006), pp. 1350–1352 (cit. on p. 18).

[47] Ahmed A Kishk. "An elliptic dielectric resonator antenna designed for circular polarization with single feed." In: *Microwave and Optical Technology Letters* 37.6 (2003), pp. 454–456 (cit. on p. 18).

[48] Longfang Zou and Christophe Fumeaux. "A cross-shaped dielectric resonator antenna for multifunction and polarization diversity applications." In: *IEEE Antennas and Wireless Propagation Letters* 10 (2011), pp. 742–745 (cit. on p. 18).

[49] Xiao Sheng Fang and Kwok Wa Leung. "Linear-/circular-polarization designs of dual-/wide-band cylindrical dielectric resonator antennas." In: *IEEE Transactions on Antennas and Propagation* 60.6 (2012), pp. 2662–2671 (cit. on p. 18).

[50] Meng Zhang, Bin Li, and Xin Lv. "Cross-slot-coupled wide dual-band circularly polarized rectangular dielectric resonator antenna." In: *IEEE antennas and wireless propagation letters* 13 (2014), pp. 532–535 (cit. on pp. 18, 19).

[51] Xiao Sheng Fang, Kwok Wa Leung, and Eng Hock Lim. "Singly-fed dual-band circularly polarized dielectric resonator antenna." In: *IEEE antennas and wireless propagation letters* 13 (2014), pp. 995–998 (cit. on p. 19).

[52] Bin Li, Cheng-Xiang Hao, and Xin-Qing Sheng. "A dual-mode quadrature-fed wideband circularly polarized dielectric resonator antenna." In: *IEEE Antennas and wireless propagation letters* 8 (2009), pp. 1036–1038 (cit. on pp. 19, 20).

[53] Xiao-Chuan Wang et al. "Single-feed dual-band circularly polarized dielectric resonator antenna for CNSS applications." In: *IEEE Transactions on Antennas and Propagation* 65.8 (2017), pp. 4283–4287 (cit. on p. 20).

[54] Meng Zou and Jin Pan. "Wide dual-band circularly polarized stacked rectangular dielectric resonator antenna." In: *IEEE Antennas and Wireless Propagation Letters* 15 (2015), pp. 1140–1143 (cit. on pp. 20, 21).

[55] Joshua M Kovitz and Yahya Rahmat-Samii. "Using thick substrates and capacitive probe compensation to enhance the bandwidth of traditional CP patch antennas." In: *IEEE Transactions on Antennas and Propagation* 62.10 (2014), pp. 4970–4979 (cit. on p. 36).

[56] William L Langston and David R Jackson. "Impedance, axial-ratio, and receive-power bandwidths of microstrip antennas." In: *IEEE transactions on antennas and propagation* 52.10 (2004), pp. 2769–2774 (cit. on pp. 36, 59).

[57] Xin Wang et al. “3D printing of polymer matrix composites: A review and prospective.” In: *Composites Part B: Engineering* 110 (2017), pp. 442–458 (cit. on p. 64).

[58] Vincenzo Tagliaferri et al. “Environmental and economic analysis of FDM, SLS and MJF additive manufacturing technologies.” In: *Materials* 12.24 (2019), p. 4161 (cit. on p. 64).

[59] Flaviana Calignano et al. “Overview on additive manufacturing technologies.” In: *Proceedings of the IEEE* 105.4 (2017), pp. 593–612 (cit. on pp. 65, 66).

[60] Mojtaba Izadi et al. “A review of laser engineered net shaping (LENS) build and process parameters of metallic parts.” In: *Rapid Prototyping Journal* (2020) (cit. on p. 65).

[61] Yun Lu Tee et al. “PolyJet 3D printing of composite materials: experimental and modelling approach.” In: *Jom* 72.3 (2020), pp. 1105–1117 (cit. on p. 65).

[62] A Simchi, F Petzoldt, and H Pohl. “On the development of direct metal laser sintering for rapid tooling.” In: *Journal of materials processing technology* 141.3 (2003), pp. 319–328 (cit. on p. 65).

[63] Morgan Larsson, Ulf Lindhe, and OLA Harrysson. “Rapid manufacturing with Electron Beam Melting (EBM)-A manufacturing revolution?” In: *2003 International Solid Freeform Fabrication Symposium*. 2003 (cit. on p. 65).

[64] Stephan M Wagner and Robert O Walton. “Additive manufacturing’s impact and future in the aviation industry.” In: *Production Planning & Control* 27.13 (2016), pp. 1124–1130 (cit. on p. 65).

[65] AK Matta et al. “Metal Prototyping the future of Automobile Industry: A review.” In: *Materials Today: Proceedings* 5.9 (2018), pp. 17597–17601 (cit. on p. 65).

[66] Murathan Kalender et al. “Additive manufacturing and 3D printer technology in aerospace industry.” In: *2019 9th International Conference on Recent Advances in Space Technologies (RAST)*. IEEE. 2019, pp. 689–694 (cit. on p. 65).

[67] Roger Naslain. “Design, preparation and properties of non-oxide CMCs for application in engines and nuclear reactors: an overview.” In: *Composites Science and Technology* 64.2 (2004), pp. 155–170 (cit. on p. 65).

[68] Isabelle Denry and J Robert Kelly. “State of the art of zirconia for dental applications.” In: *Dental materials* 24.3 (2008), pp. 299–307 (cit. on p. 65).

[69] Yongduk Oh et al. “Microwave dielectric properties of zirconia fabricated using NanoParticle Jetting$^{\text{TM}}$.” In: *Additive Manufacturing* 27 (2019), pp. 586–594 (cit. on p. 65).

[70] 3DCeram. *Additive Manufacturing for industrial applications*. Tech. rep. 3DCeram, 2021 (cit. on p. 65).

[71] RHJ Hannink, MJ Murray, and HG Scott. “Friction and wear of partially stabilized zirconia: basic science and practical applications.” In: *Wear* 100.1-3 (1984), pp. 355–366 (cit. on p. 66).

[72] Giuseppe Addamo et al. “3-D printing of high-performance feed horns from Ku-to V-bands.” In: *IEEE Antennas and Wireless Propagation Letters* 17.11 (2018), pp. 2036–2040 (cit. on p. 66).

[73] Payam Nayeri et al. “3D printed dielectric reflectarrays: Low-cost high-gain antennas at sub-millimeter waves.” In: *IEEE Transactions on Antennas and Propagation* 62.4 (2014), pp. 2000–2008 (cit. on p. 66).

[74] Ngoc Tinh Nguyen et al. “Design and characterization of 60-GHz integrated lens antennas fabricated through ceramic stereolithography.” In: *IEEE Transactions on Antennas and Propagation* 58.8 (2010), pp. 2757–2762 (cit. on p. 66).

[75] Min Liang et al. “A 3-D Luneburg lens antenna fabricated by polymer jetting rapid prototyping.” In: *IEEE Transactions on Antennas and Propagation* 62.4 (2014), pp. 1799–1807 (cit. on pp. 66, 68).

[76] Majid Ahmadloo and Pedram Mousavi. “Application of novel integrated dielectric and conductive ink 3D printing technique for fabrication of conical spiral antennas.” In: *2013 IEEE Antennas and Propagation Society International Symposium (APSURSI)*. IEEE. 2013, pp. 780–781 (cit. on p. 66).

[77] JJ Adams et al. “3D-printed spherical dipole antenna integrated on small RF node.” In: *Electronics Letters* 51.9 (2015), pp. 661–662 (cit. on p. 66).

[78] David R Jackson and Stuart A Long. “History of microstrip and dielectric resonator antennas.” In: *2020 14th European Conference on Antennas and Propagation (EuCAP)*. IEEE. 2020, pp. 1–5 (cit. on p. 66).

[79] Vito Basile et al. “Design and manufacturing of super-shaped dielectric resonator antennas for 5G applications using stereolithography.” In: *IEEE Access* 8 (2020), pp. 82929–82937 (cit. on p. 66).

[80] Matias Cuevas et al. “Parametric Study of a Fully 3D-Printed Dielectric Resonator Antenna Loaded With a Metallic Cap.” In: *IEEE Access* 9 (2021), pp. 73771–73779 (cit. on p. 67).

[81] Zhen-Xing Xia, Kwok Wa Leung, and Kai Lu. “3-D-printed wideband multi-ring dielectric resonator antenna.” In: *IEEE Antennas and Wireless Propagation Letters* 18.10 (2019), pp. 2110–2114 (cit. on p. 68).

[82] Quentin Lamotte et al. In: (cit. on p. 69).

[83] Tannu Gupta, Mohammad Jaleel Akhtar, and Animesh Biswas. “A unit cell approach to model and characterize the metal powders and metal-dielectric composites at microwave frequencies.” In: *Progress In Electromagnetics Research B* 49 (2013), pp. 363–387 (cit. on p. 70).

[84] Leon Brillouin. *Wave propagation in periodic structures: electric filters and crystal lattices*. Vol. 2. Dover publications, 1953 (cit. on p. 70).

[85] William D Callister and David G Rethwisch. *Fundamentals of materials science and engineering*. Vol. 471660817. Wiley London, 2000 (cit. on p. 70).

[86] Raymond C Rumpf. “Engineering the dispersion and anisotropy of periodic electromagnetic structures.” In: *Solid State Physics* 66 (2015), pp. 213–300 (cit. on pp. 71, 73, 74).

[87] Yong Mei Pan, Kwok Wa Leung, and Kai Lu. “Study of resonant modes in rectangular dielectric resonator antenna based on radar cross section.” In: *IEEE Transactions on Antennas and Propagation* 67.6 (2019), pp. 4200–4205 (cit. on pp. 107, 108).

[88] DR Smith et al. “Electromagnetic parameter retrieval from inhomogeneous metamaterials.” In: *Physical review E* 71.3 (2005), p. 036617 (cit. on pp. 129, 130).

[89] S Arslanagić et al. “A review of the scattering-parameter extraction method with clarification of ambiguity issues in relation to metamaterial homogenization.” In: *IEEE Antennas and Propagation Magazine* 55.2 (2013), pp. 91–106 (cit. on pp. 129, 130).

[90] Xudong Chen et al. “Robust method to retrieve the constitutive effective parameters of metamaterials.” In: *Physical review E* 70.1 (2004), p. 016608 (cit. on p. 129).

[91] Ahmad B Numan and Mohammad S Sharawi. “Extraction of material parameters for metamaterials using a full-wave simulator [education column].” In: *IEEE Antennas and Propagation Magazine* 55.5 (2013), pp. 202–211 (cit. on p. 130).

[92] Ansys. *HFSS online help 17.2*. 2016 (cit. on p. 131).

Abstract — Additive manufacturing, or simply three-dimensional (3D)-printing, has been playing an important role in different fields due to its rapid manufacturing, energy savings, customization, and material waste reduction, to name a few. When it comes to antenna applications, it turns out that most of the dielectric-based 3D-printed solutions proposed in the literature deal with non-resonant and large structures in comparison to the wavelength. More recently, the possibility of using ceramics as printing material opened new possibilities for the design of small and resonant structures due to the higher dielectric constant. In this context, the main goal of this work is to show the possibility of locally controlling the inhomogeneity and anisotropy of a dielectric. To demonstrate it, multi-band dielectric resonator antennas (DRAs) are proposed to achieve circular polarization and/or specific radiation patterns by manipulating the electric permittivity of the dielectric. At first, an original approach to design a dual-band and circularly polarized DRA is presented. The circular polarization is achieved only due to the manipulation of the permittivity of the dielectric instead of using complex feeding techniques and/or using complex dielectric shapes as most of the works found in the literature. The results demonstrate the efficiency of the proposed model and a design guideline for this type of antenna is presented. Besides, an extension to a triple-band antenna is proposed with the two lower bands presenting circular polarization and broadside radiation pattern, while the upper band has linear polarization and omnidirectional pattern. Both antennas require an assembly of anisotropic and isotropic dielectrics with specific values of permittivity to achieve the desired results. However, not necessarily, these materials with these characteristics would be available. To overcome this issue, periodically arranged sub-wavelength cells allow to create artificial and heterogeneous media by controlling their effective permittivity. For this purpose, only zirconia is used as printing material in a single manufacturing process using 3D printing technology.

Keywords: 3D-printing, anisotropy, circular polarization, dielectric resonator antennas, inhomogeneity, multi-band, periodic structures.

Résumé — La fabrication additive, ou simplement l'impression tridimensionnelle (3D), joue un rôle important dans différents domaines en raison de sa rapidité de fabrication, des économies d'énergie, de la personnalisation et de la réduction des déchets de matériaux, par exemple. En ce qui concerne les applications d'antennes, il s'avère que la plupart des solutions imprimées en 3D à base de diélectrique proposées dans la littérature portent sur des structures non résonantes et de grande taille par rapport à la longueur d'onde. Plus récemment, la possibilité d'utiliser la céramique comme matériau d'impression a ouvert de nouvelles possibilités pour la conception de structures petites et résonantes en raison de la constante diélectrique plus élevée. Dans ce contexte, l'objectif principal de ce travail est de montrer la possibilité de contrôler localement l'inhomogénéité et l'anisotropie d'un diélectrique. Pour le démontrer, des antennes à résonateur diélectrique (DRAs) multibandes sont proposées pour

obtenir polarisation circulaire et/ou des diagrammes de rayonnement spécifiques en manipulant la permittivité électrique du diélectrique. Dans un premier temps, une approche originale pour concevoir un DRA bi-bande à polarisation circulaire est présentée. La polarisation circulaire est obtenue uniquement grâce à la manipulation de la permittivité du diélectrique au lieu d'utiliser des techniques d'alimentation complexes et/ou d'utiliser des formes diélectriques complexes comme la plupart des travaux trouvés dans la littérature. Les résultats démontrent l'efficacité du modèle proposé et un guide de conception pour ce type d'antenne est présenté. En outre, une extension à une antenne à trois bandes est proposée, les deux bandes inférieures présentant polarisation circulaire et un diagramme de rayonnement large, tandis que la bande supérieure a une polarisation linéaire et un diagramme omnidirectionnel. Les deux antennes nécessitent un assemblage de diélectriques anisotropes et isotropes avec des valeurs spécifiques de permittivité pour obtenir les résultats souhaités. Cependant, ces matériaux présentant ces caractéristiques ne sont pas nécessairement disponibles. Pour surmonter ce problème, des motifs sub-longueur d'onde agencés périodiquement permettent de créer des milieux artificiels et hétérogènes en contrôlant leur permittivité effective. Pour cela uniquement la zircone est utilisée comme matériau d'impression en un seul procédé de fabrication en utilisant la technologie d'impression 3D.

Mots clés : Impression 3D, anisotrope, polarisation circulaire, antennes à résonateur diélectrique, inhomogène, multibande, structures périodiques.
